Dissertation

submitted to the

Combined Faculty of Natural Sciences and Mathematics

of Heidelberg University, Germany

for the degree of

Doctor of Natural Sciences

Put forward by

Helena Almazán Molina

born in Almería

Oral examination on February 05$^{\text{th}}$, 2020

Evaluation of the Neutron Detection Efficiency

in the STEREO Reactor Neutrino Experiment

Referees:

PROF. DR. DR. H.C. MANFRED LINDNER

PROF. DR. HANS-CHRISTIAN SCHULTZ-COULON

Abstract

Der Stereo Detektor misst Elektron-Antineutrinos aus dem Forschungsreaktor am Institut Laue-Langevin (Grenoble, Frankreich). In einer Entfernung von $\sim 10\,\mathrm{m}$ vom Reaktorkern sucht Stereo mit einem segmentierten Targetvolumen nach Neutrino-Oszillationen aufgrund eines leichten sterilen Neutrinos zur Erklärung der 2011 beobachteten Reaktor-Antineutrino-Anomalie. Um dieses Ziel zu erreichen ist eine genaue Bestimmung der Nachweiseffizienz des durch den inversen Betazerfall (IBZ), $\bar{\nu}_e + p \rightarrow e^+ + n$, erzeugten korrelierten Signals notwendig. Speziell bedarf es einem guten Verständnis der Nachweiseffizienz für die IBZ Neutronen, sowohl in den experimentellen Daten als auch in den Simulationen, da es sich hier um eine der dominanten systematischen Unsicherheiten der Stereo Analyse handelt. Es wurde eine AmBe Quelle in verschiedene Subvolumina des Detektors eingesetzt, um mit hoher Genauigkeit die Eigenschaften des Neutronennachweises zu untersuchen. Unter anderem wurden innerhalb dieser Arbeit speziell die Selektionskriterien, Ortsabhängigkeiten und Modelle zum Neutroneneinfang geprüft. Die AmBe Quelle wurde auch benutzt, um die Modellierung der ausgestrahlten Gamma-Kaskade nach einem Neutroneneinfang von Gadolinium (im Flüssigszintillator vorhandene Atomkerne) zu testen. Der Fokus dieser Arbeit ist auf die Untersuchung der relevantesten Eigenschaften im Hinblick auf Korrekturfaktoren zwischen Daten und Simulation gerichtet und liefert, die einen entscheidenden Beitrag zur Analyse im Stereo Experiment liefert.

∽❋∼

The Stereo detector is measuring electron antineutrinos from the research reactor at the Institut Laue-Langevin (Grenoble, France). Located at $\sim 10\,\mathrm{m}$ from its core and with a segmented neutrino target, Stereo is searching for light sterile neutrino oscillations as a possible explanation for the Reactor Antineutrino Anomaly observed in 2011. An accurate determination of the detection efficiency of the correlated signal created by the electron antineutrino interaction, $\bar{\nu}_e + p \rightarrow e^+ + n$, called inverse beta decay (IBD) is needed to reach that goal. More concretely, a good understanding of the detection efficiency for the IBD neutrons is required, in both data and simulation, since it is one of the dominant systematic uncertainties of the Stereo analysis. An AmBe neutron source has been deployed throughout the different sub-volumes of the detector, and has been used to study the properties of the neutron detection with high accuracy. Among others, the selection cuts, neutron vertex dependencies and neutron capture models have been specially investigated along this thesis. The AmBe source has been used to test the modelisation of the gamma cascade emitted after a neutron capture on gadolinium (nuclei present in the liquid scintillator). This thesis is focused on studying the most relevant properties in terms of data-to-simulation correction coefficients, providing thus a crucial input in the oscillation analysis of the Stereo experiment.

"I wish it need not have happened in my time" – said Frodo.
"So do I" – said Gandalf – "and so do all who live to see such times.
But that is not for them to decide.
All we have to decide is what to do with the time that is given us."
— TOLKIEN, *The Fellowship of the Ring.*

Por el Tito Pepe, por enseñarnos a que hay que vivir la vida,
y por Mario, porque él siempre quiso una tesis llena de $\sum$.

Contents

3

Introduction

During the last decades, the neutrino oscillation phenomenon has been a puzzling enigma for the physics community. However, in the most recent years neutrinos coming from different sources have provided complementary information to build a clearer neutrino oscillation picture. Among them, nuclear reactors have played an important role in the evaluation of the oscillation angle θ_{13}. Experiments like Double Chooz, Daya Bay or RENO have presented an accurate evaluation of this oscillation angle, that is necessary for the current efforts searching for CP violation in the leptonic sector or for the determination of the neutrino mass ordering.

A missing piece in the global picture of the reactor neutrino physics has been brought up in the last decade. In 2011, the predicted flux of $\overline{\nu}_e$ from nuclear reactors was recalculated after the improvement of the decay yields for all the fission products and the neutron lifetime, causing a considerable deficit on the observed-to-expected ratio. This reactor antineutrino anomaly (RAA) is still under investigation, and several theories have been developed to explain it. Some experiments have reported that the evaluation of the ν-spectrum from a specific fuel isotope ^{235}U may be the primary cause of the RAA. Others pointed out a possible underestimation of the error bars of the points conforming the RAA, suggesting thus that the anomaly is a statistical artifact. However, the existence of light sterile neutrinos taking part in the flavor oscillation phenomenon has also been proposed as the reason of the deficit of $\overline{\nu}_e$. This last hypothesis can be studied with the evaluation of the neutrino flux at very short baselines. Consequently, a set of reactor experiments placed at distances $\lesssim 10\,\text{m}$ from a reactor core have appeared in the last years. The STEREO detector is one of the flagships among them.

The STEREO experiment operates since 2016 near the highly-enriched uranium reactor at the Institut Laue-Langevin (ILL – Grenoble, France). This detector measures the neutrino flux at different baselines by means of a segmented neutrino target, being an oscillation study in this way performed independently of an emitted flux prediction. The $\overline{\nu}_e$ detection principle is by inverse beta decay (IBD, $\overline{\nu}_e + p \rightarrow e^+ + n$) in the gadolinium loaded liquid scintillator. The two particles emitted in this process are detected via a correlated signal. The positron annihilation gives a prompt signal that carries information about the neutrino energy, while the delayed neutron signal is used to tag the process a few µs later and to optimize the $\overline{\nu}_e$ selection by removing background contributions. An oscillation towards a sterile neutrino state would be indirectly observed as the disappearance of neutrino emitted initially, leading to a deficit of observed IBD events. The STEREO detector is testing the sterile neutrino hypothesis, while it is providing an evaluation of the electron antineutrino rate coming from a pure ^{235}U fuel fuel.

These two analyses need a tight control of the detection systematic uncertainties, especially when a data-to-simulation is performed. The simulation of IBD processes in the liquid scintillator is very sensitive to inaccuracies on the implementation of the neutron physics, being therefore set of correction coefficients necessary to perform a proper comparison with data. This thesis is focused on the study of such correction coefficients for the neutron selection efficiency. Neutron interactions have been evaluated with calibration data from an AmBe neutron source, deployed throughout the detector volume on a monthly basis. A summary of the relevant neutron physics is described in Chapter 3, together with the corresponding signal left in the STEREO detector.

Two different correction coefficients are defined in Chapter 4 for the STEREO analysis: one that evaluates the relative abundance of neutron captures, and another one that quantifies the effect of the neutron selection criteria. The robustness of these correction coefficients with respect to the simulation is presented on that chapter. Several properties of the neutron interactions have been upgraded in the simulation framework to reach a good agreement with data. One of them is the use of the FIFRELIN model to describe the gamma cascade emitted during the de-excitation of the gadolinium isotopes. The correction coefficients used in the STEREO analysis with the previous model, based in `GLG4sim`, are described in Chapter 5, while the impact of using the FIFRELIN model is discussed in Chapter 6.

The STEREO analyses has a strong dependence on the detection systematic uncertainties. The values computed along this thesis have been essential for the observation to expectation studies presented in the latest publications of the STEREO collaboration [1, 2, 3, 4], taking this a step forward to disentangle the deficit of $\overline{\nu}_e$ at very short baselines from reactors.

Reactor Neutrinos and the Light Sterile Neutrino Searches

The postulated neutrino in 1930 [8] was firstly detected with a reactor neutrino experiment in 1956 [6, 7]. However, the first evidence of neutrino oscillations was found in 1998 [8]. Since then, this controversial particle of the Standard Model has been thoroughly proved to oscillate with different neutrino sources, being T. Kajita and A. B. McDonald awarded with the 2015 Nobel Prize for physics for their contribution proving this phenomena [10]. This chapter is focused on the study of the neutrino oscillations with reactor experiments, from its mathematical formulation in Section 1.1 to its production and detection in Section 1.2. The two unsolved anomalies that have appeared in the last decade during the study of reactor neutrinos are described in Section 1.3: one related to the absolute neutrino flux, and another to the neutrino spectral shape. The first one, known as the Reactor Antineutrino Anomaly, represents the observed deficit in the neutrino flux compared to the expected one that could point to the existence of a light sterile neutrino on the eV range. The investigation of light sterile neutrinos via the oscillation phenomenon is a hot topic in reactor neutrino physics nowadays, and its motivation together with the current state of the art of the reactor experiments can be found in Section 1.4.

1.1 Neutrino Oscillations

As an introduction of this chapter, a basic definition of the neutrino oscillations is presented. A neutrino state is described in general at the production vertex by the flavour eigenstate $\{|\nu_\alpha\rangle\}$ with $\{\alpha = e, \mu, \tau\}$. These flavour eigenstates are a superposition of the mass eigenstates $\{|\nu_i\rangle\}$ with $\{i = 1, 2, 3\}$ that govern their propagation. In the three flavor paradigm these eigenstates can be connected as,

$$\begin{pmatrix} \nu_e \\ \nu_\mu \\ \nu_\tau \end{pmatrix} = \begin{pmatrix} \mathcal{U}_{e1} & \mathcal{U}_{e2} & \mathcal{U}_{e3} \\ \mathcal{U}_{\mu 1} & \mathcal{U}_{\mu 2} & \mathcal{U}_{\mu 3} \\ \mathcal{U}_{\tau 1} & \mathcal{U}_{\tau 2} & \mathcal{U}_{\tau 3} \end{pmatrix} \begin{pmatrix} \nu_1 \\ \nu_2 \\ \nu_3 \end{pmatrix} , \tag{1.1}$$

where $\mathcal{U}$ is the mixing matrix describing the misalignment between them. This description can also be generally written as

$$|\nu_\alpha\rangle = \sum_{j=1}^{3} \mathcal{U}_{\alpha j} |\nu_j\rangle , \tag{1.2}$$

where the number of light neutrino species [11] is taken into account. The Hamiltonian is not diagonal when represented in the flavor basis $\{|\nu_\alpha\rangle\}$, thus an effective mixing of the flavors is cre-

5

ated providing each mass eigenstate a different propagation phase. Under these circumstances, a neutrino state with a flavor α, after traveling a distance L (or time t for relativistic neutrinos), will evolve as

$$|\nu(L)\rangle = \sum_{\beta=e,\tau,\mu} \left(\sum_i \mathcal{U}_{\alpha i}^* e^{-iE_i L} \mathcal{U}_{\beta i} \right) |\nu_\beta\rangle \, . \tag{1.3}$$

Considering the ultrarelativistic approximation $E_i = \sqrt{p_j^2 + m_j^2} \approx p_j + \frac{m_j^2}{2E}$, the transition probability of a neutrino generated with energy E in a flavor state ν_α into a flavor state ν_β after a distance L is written [11]

$$\begin{aligned} \mathrm{P}_{\nu_\alpha \to \nu_\beta}(L, \, E) = |\langle \nu_\beta | \nu(L) \rangle|^2 = \delta_{\alpha\beta} &- 4 \sum_{i>j} \mathrm{Re} \left[\mathcal{U}_{\alpha i}^* \mathcal{U}_{\beta i} \mathcal{U}_{\alpha j} \mathcal{U}_{\beta j}^* \right] \sin^2 \left(\frac{\Delta m_{ij}^2 L}{4E} \right) \\ &- 2 \sum_{i>j} \mathrm{Im} \left[\mathcal{U}_{\alpha i}^* \mathcal{U}_{\beta i} \mathcal{U}_{\alpha j} \mathcal{U}_{\beta j}^* \right] \sin \left(\frac{\Delta m_{ij}^2 L}{4E} \right) \quad , \end{aligned} \tag{1.4}$$

where the mass splitting Δm_{ij}^2 is defined as

$$\Delta m_{ij}^2 = m_i^2 - m_j^2 \, . \tag{1.5}$$

A mass difference $m_i \neq m_j$ is necessary for the neutrino oscillations, since it implies different exponential phases in Eq. 1.3 and thus different frequencies. Since each mass eigenstate propagates with a different frequency, the oscillation phenomenon is observed in terms of Δm_{ij}^2, L and E. Following the same computation, the survival probability of a flavor state ν_α is then written

$$\mathrm{P}_{\nu_\alpha \to \nu_\alpha}(L, E) = 1 - \sum_{\alpha \neq \beta} \mathrm{P}_{\nu_\alpha \to \nu_\beta}(L, E) \, . \tag{1.6}$$

The mixing matrix $\mathcal{U}$ represents a change of basis in the Hilbert space, and it has to be unitary in order to restrict the number of degrees of freedom. Therefore $\mathcal{U}_{\alpha i}$ can be described in terms of rotations of the orthogonal mass eigenstates ($|\langle \nu_i | \nu_j \rangle| = \delta_{ij}$) into the orthogonal flavor eigensystem ($|\langle \nu_\alpha | \nu_\beta \rangle| = \delta_{\alpha\beta}$) by three Euler angles θ_{12}, θ_{13} and θ_{23} and one complex phase δ. This standard parametrization defines the Pontecorvo-Maki-Nakagawa-Sakata (PMNS) matrix as,

$$\mathcal{U}_{\mathrm{PMNS}} = \begin{pmatrix} 1 & 0 & 0 \\ 0 & c_{23} & s_{23} \\ 0 & -s_{23} & c_{23} \end{pmatrix} \times \begin{pmatrix} c_{13} & 0 & s_{13}e^{-i\delta} \\ 0 & 1 & 0 \\ -s_{13}e^{i\delta} & 0 & c_{13} \end{pmatrix} \times \begin{pmatrix} c_{12} & s_{12} & 0 \\ -s_{12} & c_{12} & 0 \\ 0 & 0 & 1 \end{pmatrix} , \tag{1.7}$$

with $c_{ij} = \cos\theta_{ij}$ and $s_{ij} = \sin\theta_{ij}$. Neutrino oscillations are observed in terms of transition probabilities, and have been observed with high accuracy in experiments [12] using different neutrino sources, including the Sun [13], atmosphere [14], reactors [15], and accelerators [16]. Each of the different type of experiments are characterized by a different neutrino flavor emission, energy and detection distance.

1.2   Reactor Neutrino Physics

The study of neutrinos from nuclear reactors has played a significant part in the understanding the neutrino oscillations, being specially relevant for the measurement of the oscillation angle θ_{13}. The basics about the $\overline{\nu}_e$ production in nuclear reactors, their propagation limits and their detection in experiments are described along this section.

1.2.1   Production and Prediction of Reactor Antineutrinos

The core of a nuclear reactor generates energy through neutron induced nuclear fission. Isotopes of ^{235}U, ^{238}U, ^{239}Pu and ^{241}Pu are targeted with neutrons, producing energy from the fission process and creating fission fragments which undergo with a cascade of β decays. This fission chain is maintained with the neutrons emitted on this process. Research reactors are normally fuelled with highly enriched uranium (HEU) ($> 20\%$ ^{235}U), while commercial power reactors use low enriched uranium (LEU) fuel. Neutrinos are produced from the cascade of β decays of these isotopes products. On average $\sim$6 $\overline{\nu}_e$ are produced per fission [15], and approximately $2 \cdot 10^{20}$ $\overline{\nu}_e$ per second and per GW$_{th}$ of thermal power are emitted. The amount of emitted $\overline{\nu}_e$ varies depending on the initial isotope, as it is portrayed in Fig. 1.2.1.

In reactor neutrino experiments, the understanding of the neutrino flux and energy spectrum is crucial, and thus several models have been created through the years in order to reproduce them. On one side, the flux and spectrum can be predicted from cumulative fission yields with thousands of branching ratios from the available data on the β-decays after fission. This method is colloquially called *ab initio* [17], and provides a $10\% - 20\%$ relative uncertainty on the $\overline{\nu}_e$ spectra due to the inaccuracy of the nuclear databases that feed the method. On the other side, an experimentally based method uses the measured information from β spectra of the different isotopes [18, 19]. This *conversion* method was initially described using the information from the nuclear reactor at Institute Laue-Langevin (ILL) from the ^{235}U, ^{239}Pu and ^{241}Pu isotopes. Later, the addition of the ^{238}U from some measurements in Munich [20] improved the model, being able to better reconstruct the $\overline{\nu}_e$ spectra. With this method, relative uncertainties were improved to a $2\% - 5\%$.
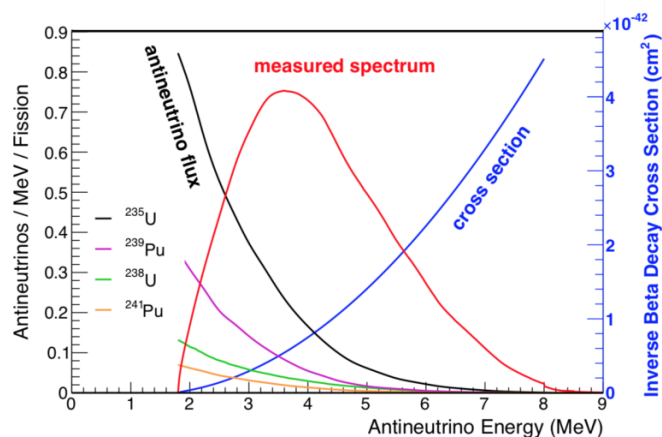
Figure 1.2.1: In the bottom of the figure, the reactor $\overline{\nu}_e$ flux from the indiviual isotopes (black) weighted by their typical contribution to the total flux in a commercial reactor. The IBD reaction cross section (blue) is used to build, together with the reactor flux, the measured $\overline{\nu}_e$ spectrum (red) [15].

1.2.2 Detection of Reactor Antineutrinos

The multiple β decays in the core produce as a result electron antineutrinos. Detectors in reactor experiments are commonly based in proton-rich active volumes, where neutrinos can interact through charge currents (CC). Taking into account that $\bar{\nu}_e$ are produced in the reactor core with an upper limit energy of $10\,\mathrm{MeV}$, these experiments are only sensitive to CC interactions in the electron channel via an inverse beta decay (IBD),

$$\bar{\nu}_e + p \rightarrow e^+ + n \;. \tag{1.8}$$

In the case of organic liquid scintillators (LS), the $\bar{\nu}_e$ interact with the hydrogen nuclei that can be considered as free protons. The threshold energy of this process is [11]

$$E_{\mathsf{IBD}} = \frac{(m_e + M_n)^2 - M_p^2}{2M_p} \;. \tag{1.9}$$

Even if e^+ and the n are emitted at the same time, the IBD is observed in this type of detectors as a time-correlated signal. Neutrons take additional time until they leave a trace in the detector due to their characteristic thermalization and the neutron capture time (see more details in Section 3.1). The IBD correlated signal is separated into a prompt and a delayed events, represented in Fig. 1.2.2:

Prompt event: The e^+ loses its kinetic energy through continuous collisions in the detector within picoseconds, until it annihilates with an e^- in the LS. The visible energy that this process leaves in the detector is

$$E_{vis,e^+} = E_K + 2m_e \cong E_{\bar{\nu}_e} - \Delta + m_e = E_{\bar{\nu}_e} - 0.782\,\mathrm{MeV} \;, \tag{1.10}$$

where $\Delta = M_n - M_p$ is the mass difference between the n and the p. This formulation shows that the visible positron energy is directly linked to the neutrino energy.

Delayed event: The neutron thermalizes by elastic scattering with nuclei of the medium. Some microseconds later it is captured in the LS. In principle, neutron captures happen in the hydrogen nuclei. However, nuclear reactor experiments have doped LS, that improve the neutron capture process and reduce the background contribution. Most of them use gadolinium (Gd) compounds,

Figure 1.2.2: Representation of the IBD interaction and its signal in a scintillator.

enhancing the neutron capture. When a Gd nuclei captures a neutron, the resulting isotope is in an excited state where a gamma cascade is released as

$$
{}_Z^A\text{Gd} + n \rightarrow {}_Z^{A+1}\text{Gd}^* \rightarrow {}_Z^{A+1}\text{Gd} + \sum_i \gamma_i \; , \tag{1.11}
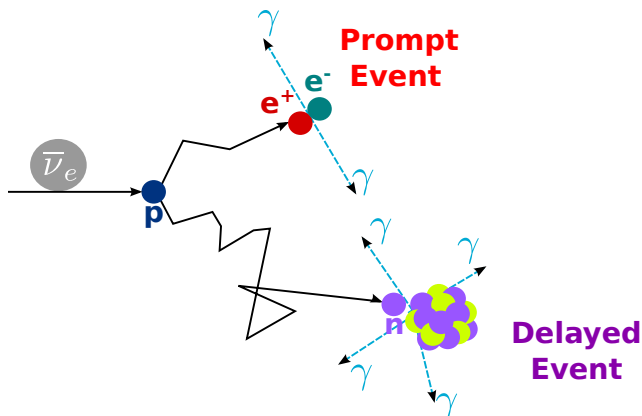$$

the emitted amount of gammas and their energies depend on the Gd isotope, but in all cases it leads to energies approximately $\sum_i E_{\gamma_i} \approx 8\,\text{MeV}$. This high energy emission optimizes the selection of correlated events. More details about the neutron interactions, and more concretely about their captures in LS compounds can be found in Chapter 3.

The prompt-delayed correlated signal provides advantages in the $\bar{\nu}_e$ detection. While the energy of the prompt event translates directly to the initial neutrino, the delayed event mainly tags the coincidence and rejects background events. The IBD cross section is analythically know, and can be evaluated to the zeroth order in terms of the neutron lifetime τ_n [12]

$$
\sigma_{\text{IBD}}^0 = \frac{2\pi}{m_e^5 \tau_n f} K_e p_e \; , \tag{1.12}
$$

where f is a phase space factor, and p_e is the momentum of the positron. Therefore, the combination of the emitted neutrino spectra and the IBD cross section leads to an observed neutrino distribution like the one in Fig. 1.2.1. Considering this distribution, and the relation Eq. 1.10, the visible energy from the positron will appear with the same resolution and shape shifted by $0.782\,\text{MeV}$.

1.2.3 Propagation of Reactor Antineutrinos and θ_{13} Experiments

As explained in Section 1.1, reactors produce $\bar{\nu}_e$ that can change flavor as they propagate. Their detection allows the measurement of their survivability. From Eq. 1.4 and Eq. 1.6, it can be computed

$$
\begin{aligned}
\text{P}_{\bar{\nu}_e \rightarrow \bar{\nu}_e}(L, E) = &\; 1 - 4\cos^2(\theta_{12})\cos^2(\theta_{13})\sin^2(\theta_{12})\sin^2(\theta_{13})\sin^2\left(\frac{\Delta m_{21}^2 L}{4E}\right) \\
&- 4\cos^2(\theta_{12})\cos^2(\theta_{13})\sin^2(\theta_{13})\sin^2\left(\frac{\Delta m_{31}^2 L}{4E}\right) - 4\sin^2(\theta_{12})\cos^2(\theta_{13})\sin^2(\theta_{13})\sin^2\left(\frac{\Delta m_{32}^2 L}{4E}\right) \; .
\end{aligned} \tag{1.13}
$$

This equation represents the evolution of the flavor fraction for an initial $\bar{\nu}_e$ flux, also portrayed in Fig. 1.2.3. This expression can be simplified by two considerations. First of all, in the $1\,\text{km}$ baseline reactor experiments the L/E ratio has a specific value $\sim 5 \cdot 10^2$ km/GeV. Secondly, $|\Delta m_{ij}^2|$ is known, and in this case $|\Delta m_{31}^2| \gg |\Delta m_{21}^2|$. Consequently, the survival probability for an electron antineutrino can be approximated to

$$
\text{P}_{\bar{\nu}_e \rightarrow \bar{\nu}_e}(L, E) \simeq 1 - \sin^2 2\theta_{13} \sin^2\left(\frac{\Delta m_{31}^2 L}{4E_\nu}\right) \; . \tag{1.14}
$$

This relation implies that at baselines of $\sim 1\,\text{km}$, the amplitued of oscillation is governed by θ_{13}, while the frequency is given by Δm_{31}^2. Under these assumptions, θ_{13} can be evaluated from nuclear reactors independent of the CP phase and θ_{23}. Note that matter effects are not relevant for reactor neutrino experiment with short baselines [11].
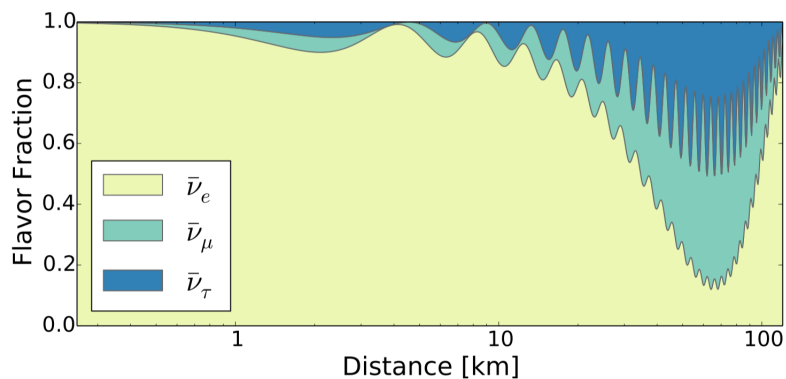
Figure 1.2.3: Expected flavor composition of the reactor $\overline{\nu}_e$ flux for neutrinos of $4\,\text{MeV}$ energy plotted as a function of distance to the reactor cores [15].

In the 1990s $\sim\text{km}$ baseline reactor experiments with senstivity on θ_{13} have started measuring. This first generation of experiments, formed by CHOOZ (France) and PALO VERDE (United States) were not precise enough to measure the $\overline{\nu}_e$ deficit caused by the θ_{13} oscillation angle. Instead, only an upper limit of $\sin^2(2\theta_{13}) < 0.15$ at 90% C.L. was established for $|\Delta m_{13}^2| = 2.4 \cdot 10^{-3} \text{eV}^2$ [15]. The results from these experiments, combined with the measured values of θ_{23} and θ_{12} from atmospheric and solar experiments, motivated many speculations of the neutrino mixing. The importance of knowing the existance of θ_{13} triggered a series of world-wide experiments, generally called as second generation: Double Chooz (France), RENO (Korea) and Daya Bay (China). All of these experiments took data from commercial reactors and were able to measure with high statistics the oscillation effects caused by θ_{13}. In 2011, Double Chooz reported the first hint of $\overline{\nu}_e$ disappearance from a reactor after only a few months of running [23], and in 2012 Daya Bay and RENO confirmed it. The precision of the θ_{13} measurement improved quickly as more data was gathered, leading to the current best combined value of $\sin^2(2\theta_{13}) = 0.085 \pm 0.003$ [12].

1.3 Reactor Anomalies

During the first years of 2010, a series of anomalies concerning reactor neutrinos appeared when a direct comparison of the measured flux rate and shape was performed with respect to the expectation. In the following subsections more details about these two anomalies, and their possible explanations are developed.

1.3.1 The Rate Anomaly

In 2011, the expectation for emitted $\overline{\nu}_e$ from a reactor was re-evaluated considering new calculations of the decay chains of the fissionable nuclides [21, 22]. Together with some non-equilibrium effects and the updated value of the neutron lifetime used for the computation of the IBD cross section (Eq. 1.12), the predicted fluxes were increased by a 6%. This re-evaluation culminated into a rate deficit in the baseline range between $5\,\text{m}$ to $100\,\text{m}$ from the reactor. This deficit known as the *Reactor Antineutrino Anomaly* (RAA) [25] presented a 2.8σ significance. The obtained observed to predicted ratios for different experiments are shown in Fig. 1.3.1.

The RAA triggered a new branch of studies of neutrinos from nuclear reactors. One of the hypothesis relates to the existance of a new type of neutrino that would not interact weakly. An
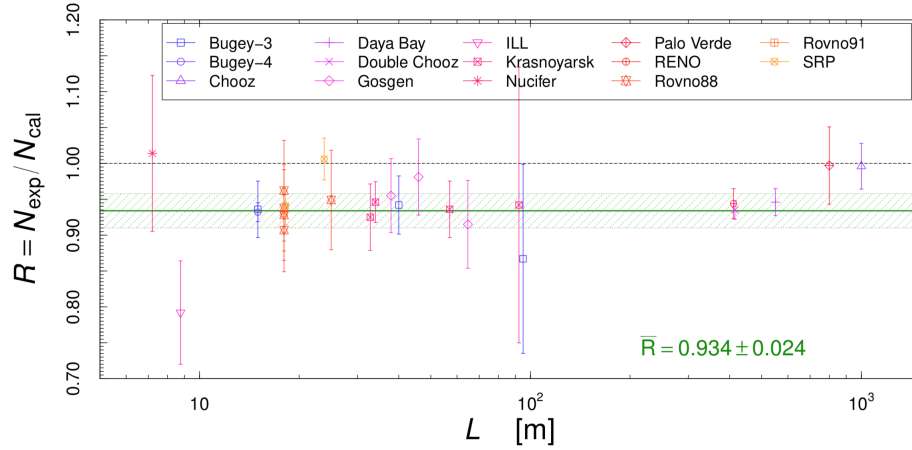
Figure 1.3.1: Ratios R of the reactor experiments as functions of the reactor-detector distance L. The horizontal band shows the average ratio R and its uncertainty. The error bars show the experimental uncertainties [26].

oscillation into a sterile neutrino would transform part of the observable flux into one or more types of non-interacting neutrinos. These invisible transitions would translate into an effective deficit of the experimental IBD rates. More information about the sterile neutrino hypothesis can be found in Section 1.4. In contrast, a second hypothesis that could explain the discrepancies consider the fission isotopes model for the neutrino prediction not accurate.

Daya Bay studied the evolution of the neutrino rate as a function of the fuel usage, for the fission isotopes. A fuel dependent variation of the IBD yield was observed with respect to theoretical predictions [27]. This conclusion disfavors the sterile neutrino hypothesis. Hybrid models with neutrino oscillations and a prediction bias for specific fission isotopes in addition are possible [28, 29].

(a)

(b)
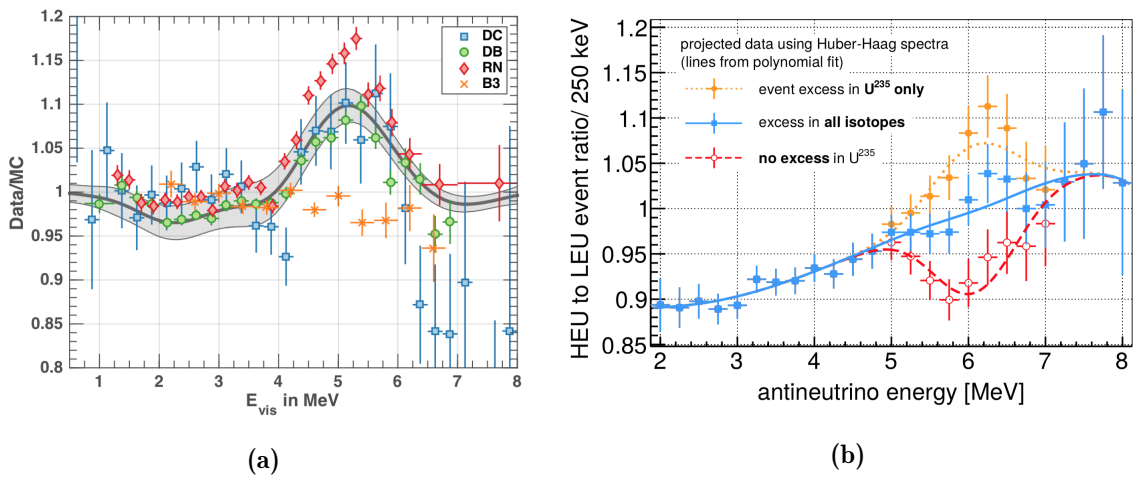
Figure 1.3.2: (a) Ratio of observed reactor antineutrino spectra to current best predictions for Double Chooz (DC), Daya Bay (DB) and RENO (RN) and Bugey 3 (B3)[33]. **(b)** Event ratio of HEU to LEU antineutrino spectra for three hypotheses [34].

11

1.3.2 The Shape Anomaly

Double Chooz [30], Daya Bay [31] and RENO [32] observed in 2014 a distortion of the neutrino spectrum known as the *shape anomaly*. When the measured neutrino spectrum was compared to the predicted one, a distortion was observed in the $5\,\text{MeV}$ region as the one depicted in Fig. 1.3.2a. Since Bugey 3 experiment presented a good agreement between its measured spectrum and the prediction, several hypotheses have appeared in order to explain this distortion. For example, in [33] a residual non-linearity in the energy response has been evaluated to explain this distortion. On the contrary, an incorrect modelisation of the emitted beta spectra from the isotopes could be the one creating an impact in the $\overline{\nu}_e$ shape. If the neutrino spectra of HEU and LEU reactors are compared as in Fig. 1.3.2b, it might show if the $5\,\text{MeV}$ excess is solely due to the ^{2365}U contributions or similar for all isotopes. This modelisation impact is studied in [34]. Currently, this anomaly has not been solved, and the information from short baseline reactor experiments could provide an indication favoring any of these hypotheses.

1.4 The Search of Light Sterile Neutrinos

In addition to the RAA, there have been other neutrino anomalies unrelated to nuclear reactors. One of them, named *Gallium anomaly* [35] was observed in the GALLEX and SAGE radiochemical experiments. These experiments testing the low energy region of solar neutrinos, while during the calibration of the detector response using the ^{51}Cr and ^{37}Ar radioactive sources, presented a deficit of detected ν_e with a ratio of $\overline{R} = 0.84 \pm 0.05$. Another well-known anomaly happened at the LSND accelerator, where an excess of $\overline{\nu}_e$ appearance events over the background with a 3.8σ was observed in agreement with the sterile neutrino hypothesis. The MiniBooNE experiment [37] tried to replicate the LSND results, but inconclusive results have been presented on this regard.

These two anomalies together with the RAA could indicate the existence of a new neutrino. Since only three neutrino flavors are allowed on the weak interactions [12], the new neutrino must be sterile and massive with a new squared-mass difference Δm_s^2. In the next subsection the simplest extension of neutrino oscillations will be described, together with the new reactor experiments studying it.

1.4.1 Neutrino Oscillations in the (3+1) Flavor Scenario

The (3+1) neutrino scenario is defined by including a new flavor eigenstate $|\nu_s\rangle$ and mass eigenstates $|\nu_4\rangle$ on top of the 3ν description of Section 1.1. Considering Eq. 1.1, the homologous mixing matrix is then written [38]

$$\begin{pmatrix} \nu_e \\ \nu_\mu \\ \nu_\tau \\ \nu_s \end{pmatrix} = \begin{pmatrix} \mathcal{U}_{e1} & \mathcal{U}_{e2} & \mathcal{U}_{e3} & \mathcal{U}_{e4} \\ \mathcal{U}_{\mu1} & \mathcal{U}_{\mu2} & \mathcal{U}_{\mu3} & \mathcal{U}_{\mu4} \\ \mathcal{U}_{\tau1} & \mathcal{U}_{\tau2} & \mathcal{U}_{\tau3} & \mathcal{U}_{\tau4} \\ \mathcal{U}_{s1} & \mathcal{U}_{s2} & \mathcal{U}_{s3} & \mathcal{U}_{s4} \end{pmatrix} \begin{pmatrix} \nu_1 \\ \nu_2 \\ \nu_3 \\ \nu_4 \end{pmatrix} \quad , \tag{1.15}$$

where the sterile state ν_s is associated with the matrix elements $\mathcal{U}_{si} \neq 0$. The new ν_s should be sterile to be allowed by the existing experimental neutrino oscillation data, with the parameters

$$|\mathcal{U}_{\alpha4}|^2 \ll 1 \text{ and } \Delta m_{4i}^2 \sim 1\,\text{eV}^2 \ (\alpha \in \{e, \mu, \tau\} \text{ and } \forall i \in \{1, 2, 3\}). \tag{1.16}$$

In this way, only the experimental configurations

$$\frac{\Delta m_{4i}^2 L}{4E} \sim 1 \tag{1.17}$$
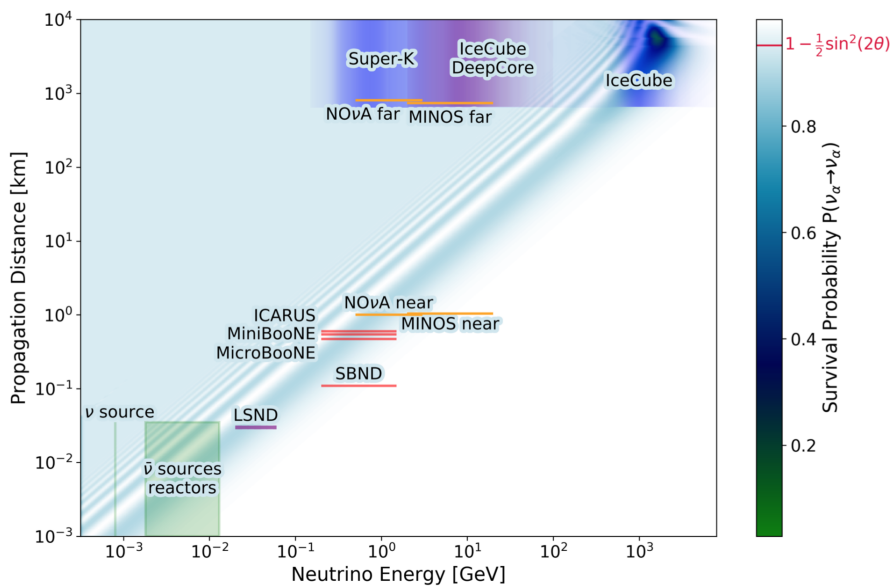
Figure 1.4.1: Neutrino oscillation probability from Eq. 1.18 for $\sin^2(2\theta) = 0.1$ and $\Delta m_s^2 = 1\,\text{eV}^2$, for different neutrino sources and their study distance [38].

would be allowed for $\Delta m_{4i} \sim 1\,\text{MeV}$. Considering this relation and the approximations used to describe Eq. 1.6, the survival probability of an initial state ν_α would then written [38]

$$
\text{P}_{\nu_\alpha \to \nu_\alpha}(L, E) \simeq 1 - \sin^2(2\theta_{\alpha\alpha}) \sin^2 \left(\frac{\Delta m_s^2 L}{4 E_\nu} \right) \, ,
\tag{1.18}
$$

with the oscillation angle

$$
\sin^2(2\theta_{\alpha\alpha}) = 4|\mathcal{U}_{\alpha 4}|^2 \left(1 - |\mathcal{U}_{\alpha 4}|^2 \right) \, .
\tag{1.19}
$$

Since the oscillation behavior depends on the ratio in Eq. 1.17, a variety of experimental configurations and neutrino sources can be used to reproduce the phenomenon. In Fig. 1.4.1 an overview of the experiments sensitive to sterile neutrinos signatures are represented in terms of their energy and distance from the source.

Reactor neutrinos have energies in the $\mathcal{O}(\text{MeV})$, thus light sterile neutrino oscillations would only be observed for distances of $\mathcal{O}(\text{m})$ considering the relation in Eq. 1.17 and $\Delta m_s \sim 1\,\text{MeV}$. Using the approximation from Eq. 1.18, the reactor $\bar{\nu}_e$ survival probability could be re-written as,

$$
\text{P}_{\bar{\nu}_\text{e} \to \bar{\nu}_\text{e}}(L, E) \simeq 1 - \sin^2(2\theta_{ee}) \sin^2 \left(\frac{\Delta m_s^2 L}{4 E_\nu} \right) \, .
\tag{1.20}
$$

with the oscillation angle

$$
\sin^2(2\theta_{ee}) = 4|\mathcal{U}_{e4}|^2 \left(1 - |\mathcal{U}_{e4}|^2 \right) = \sin^2(2\theta_{14}) \, .
\tag{1.21}
$$

13
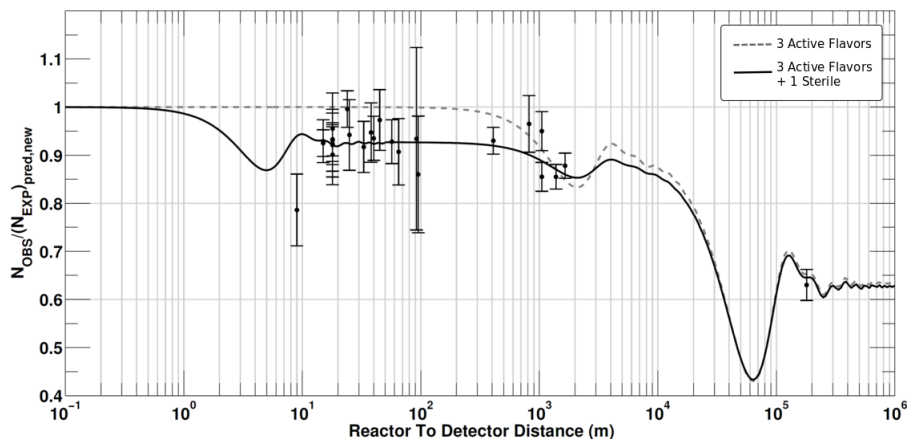
Figure 1.4.2: Observed to predicted ratio of reactor antineutrino experiments. The dashed line corresponds to the classic 3ν picture. The solid line corresponds to a 3 active neutrinos plus one sterile neutrino (3+1) model [25].

The observed to expected ratio under the (3+1) scenario is represented in Fig. 1.4.2 (solid black line), together with the survival probability of Eq. 1.13 and Eq. 1.14 (dashed black line) for the the 3ν scenario. It can be seen that in the region below $1\,\mathrm{m}$ there is no experimental data. Any reactor neutrino observation at this range would then be crucial to prove the sterile neutrino hypothesis. The reactor studies at this configuration are considered to be very short baseline (VSBL) experiments, and the current experiment status is summarized in the next section.

1.4.2 Very Short Baseline Reactor Experiments

Since the discovery of the RAA worldwide experiments appeared in order to provide the information needed to disentangle the mistery of the light sterile neutrinos. A summary of the these experiments, their most important characteristics and configuration is presented in Table 1.4.1. All of these new reactor experiments share their proximity to a reactor core within a $10\,\mathrm{m}$ range to optimize the eV sterile neutrino detection, and their scintillator targets (some of them LS and another plastic stripes – PS). Inaccuracies of the absolute flux prediction pushed these experiments to be independent to it by making relative measurements at different baselines. For example, PROSPECT, STEREO, and Soli∂ detectors are segmented in several identical volumes in a way that a model independent evaluation can be done. Other experiments as DANSS are equipped with movable systems that allows them to be placed at different baselines with respect

Table 1.4.1: Summary of the currently running VSBL experiments and their most important characteristics [1, 39, 40, 41, 42, 43].

Charact.	STEREO	Prospect	NEOS	DANSS	Soli∂	Neutrino-4
Location	France	USA	Korea	Russia	Belgium	Russia
Baseline [m]	9-11	7-9	24	11-13	6-9	6-12
Reactor	HEU	HEU	LEU	LEU	HEU	HEU
Power [MW$_{th}$]	58	85	2800	3100	50-80	100
Target	LS	LS	LS	PS	PS	LS
Dopped with	Gd	Li	Gd	Gd	Li	Gd
IBD Rate [d^{-1}]	400	750	2000	5000	450	200
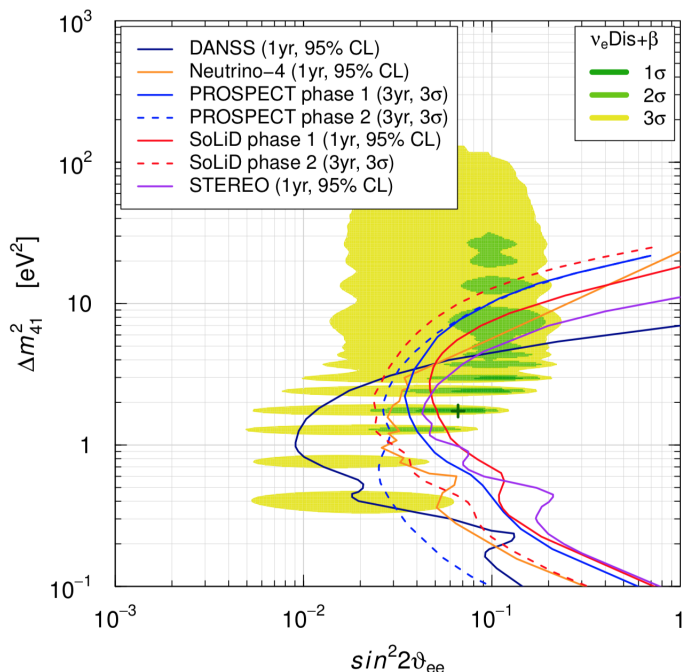
Figure 1.4.3: Sensitivity regions of $\sin^2(2\theta_{ee})$ and Δm_s^2 for the reactor experiments compared with the allowed regions from the combined fit of ν_3 and $\overline{\nu}_e$ disappearance data [26].

to the reactor core. Most of these experiments use the Gd-loading technology for a coincidence selection, already described in Section 1.2.2. However, some of them are specialized in the IBD coincidence with neutron capture in lithium. Another characteristic of these experiments is that they measure the neutrino flux from different type of reactors (HEU or LEU), in this way their information would be crucial not only for the sterile neutrino oscillation studies, but also to shed some light on the reactor shape anomaly mentioned in Section 1.3.2.

The sensitivity contours of $\sin^2(2\theta_{ee})$ and Δm_s^2 for these experiments are represented in Fig. 1.4.3, together with the best fit of the RAA at $\sin^2(2\theta_{ee}) = 0.04$ and $\Delta m_s^2 = 1.3\,\text{MeV}$ [26]. The allowed regions by the RAA in the $\sin^2(2\theta_{ee}) - \Delta m_s^2$ plane are also represented under the green area for the combined fit of ν_e and $\overline{\nu}_e$ disappearance data [26]. The RAA could indicate that the short baseline $\overline{\nu}_e$ disappearance is caused by an active sterile neutrino mixing, and it needs to be confirmed by the ongoing experiments listed in Table 1.4.1. Most of these experiments are currently taking and analyzing their $\overline{\nu}_e$ data, and will provide in the near future a global picture of the neutrino oscillations for different technologies and reactor fuels. More details about the STEREO detector, its detection technology and the most recent oscillation analysis results will be presented in the next Chapter 2.

The STEREO Experiment

The STEREO (STErile neutrino REactor Oscillation) experiment aims to investigate the existence of eV sterile neutrinos at short baselines from nuclear reactors. Its construction was proposed in 2013 [44], and it started taking data in 2016 at the Institut Laue-Langevin (ILL) in Grenoble (France). It measures a pure ^{235}U fission neutrino spectrum at only $10\,\mathrm{m}$ from the compact core of a research reactor. This detector is segmented in six identical cells to measure the energy spectrum at different distances from the reactor. Any oscillation pattern would provide a characteristic signal in the relative comparison of the spectra observed in any of them. A tight control of the background, energy resolution, and systematic uncertainties is crucial for these studies. The main components of the detector and the external backgrounds are described in Section 2.1, preceded by a short description of the ILL reactor site. In the same chapter, the information about the STEREO data taking time line is presented.. A detailed description of the DATA analysis is performed in Section 2.2, with emphasis in the oscillation analysis parameters and the most recent results.

2.1 The STEREO Detector

2.1.1 The ILL Site

The ILL is an international research reactor placed in the European Photon and Neutron (EPN) science campus in Grenoble (France). This reactor is built to provide intense beams neutrons, used for about 40 instruments in different fields of science. It has a compact core of $80\,\mathrm{cm}$ height and $40\,\mathrm{cm}$ diameter that operates with a highly enriched ^{235}U (93%) fuel. Even if the nominal reactor power of $58.3\,\mathrm{MW}_{th}$ is lower than the ones obtained in commercial nuclear power reactors, this type of cores are suitable for very short baseline neutrino oscillation studies.

The STEREO detector is located in the ILL reactor building at *Level C*, as it can be seen in Fig. 2.1.1. Even thought it is placed at ground floor, STEREO takes benefit of being placed right below to the water channel used to renew the spent fuel from the reactor core. This channel is filled with a layer of water $7\,\mathrm{m}$ deep, which leads to an overburden of about 15 m.w.e. The detector is surrounded by two instruments, IN20 and D19. The first one is a thermal three-axis spectrometer, used for inelastic scattering experiments. The second is a thermal neutron diffractionmeter for single-crystal and fiber diffraction. Due to its location in the reactor site, STEREO is affected by several issues like reactor induced γ-rays and neutrons or high magnetic fields from the two close experiments aforementioned.
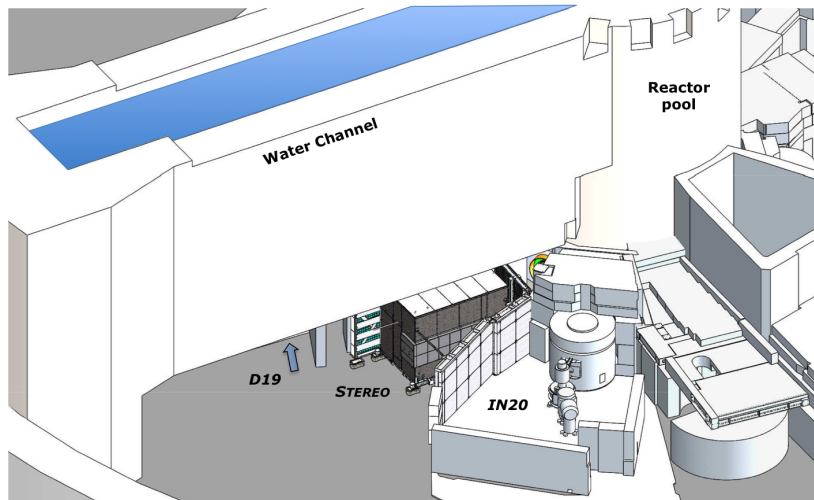
Figure 2.1.1: STEREO location in the ILL reactor site [45].

2.1.2 Detector Design

The STEREO detector can be divided in two main volumes depending on their purpose and position. An inner part, in charge of detecting the neutrino interactions and collecting the detector signal; and an outer geometry that shields and protects the detector from external background. The inner volume is formed by three main parts represented in Fig. 2.1.2a.: the neutrino target, the gamma catcher and the acrylic buffer.

The outer sections have been designed to shield three different types of backgrounds: the cosmic radiation observed as a consequence of having a ground level experiment; the reactor induced backgrounds as the high flux of neutrons from neighbor experiments, and the magnetic fields created by their superconducting coils; and natural radioactivity. The first type of backgrounds can be tagged by the implementation of a Cherenkov muon veto on top of the detector volume. The other two can be minimized by the addition of shielding layers around the detector vessel and on site. In the following sections each one of the parts of the STEREO is detailed, together with an overview of the detector shielding.

Neutrino Target

The center volume of STEREO is the neutrino target (NT), that defines the area where neutrinos interact via IBD. It is surrounded by an acrylic aquarium of $12\,\mathrm{mm}$ thickness, with dimensions of $L \times l \times h = 2.233\,\mathrm{m} \times 0.889\,\mathrm{m} \times 1.230\,\mathrm{m}$ that is divided in six identical cells. These cells are named by their relative distance from the reactor from Cell 1 until Cell 6. They are optically separated from each other by a highly reflective *sandwich* (represented in Fig. 2.1.2b) created with two reflective films (VM2000$^{\mathrm{TM}}$), two acrylic plates and a thin nylon net placed in the air gap between them.

These six cells are filled with an organic LS based on linear alkylbenzene (LAB, $\sim$75 wt.%). This liquid fulfills the optical requirements needed to observe the IBD neutrinos, like light yield and high transparency above $400\,\mathrm{mm}$, compatibility with materials of the detector and high flash point. In lower concentrations, ortho-phenyl-xylyl-ethane (PXE, $\sim$20 wt.%) and di-isopropy-naphtalene (DIN, $\sim$5 wt.%) were added to increase the light yield and the pulse shape discrimination (PSD) capabilities [61]. The LS is loaded with a gadolinium organic complex based on β-diketone. This type of technology where Gd(thd)$_3$ molecules are dissolved in LS was devel-
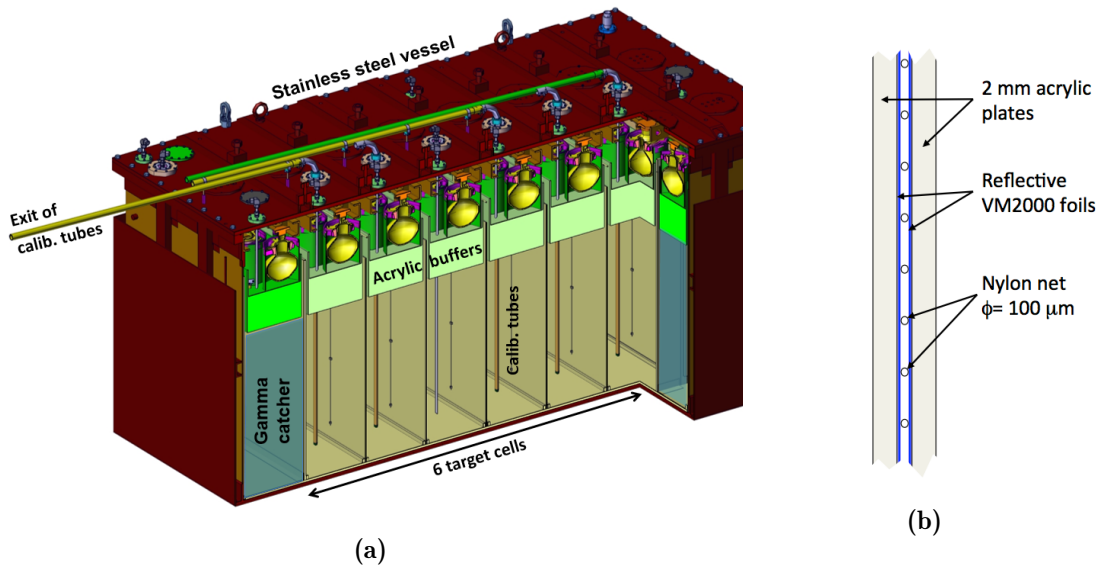
Figure 2.1.2: **(a)** STEREO detector inner volume and **(b)** structure of the reflective walls [45].

oped for Double Chooz and later for the Nucifer experiment [46]. For the STEREO experiment, a concentration of 0.2 wt.% is used to optimize the coincidence time of the neutrino signal. A combination of diphenyloxazole (PPO) and bis-methylstyrylbenzen (bis-MSB) wavelenght shifters is included in the solution.

Gamma Catcher

Surrounding the NT there is another active detector layer called gamma catcher (GC). It helps to collect the escaped gammas from the events in the NT, and to shield it from residual backgrounds. It is enclosed within a larger double walled stainless steel vessel, of dimensions $L \times l \times h = 3.096\,\text{m} \times 1.536\,\text{m} \times 1.505\,\text{m}$. For mechanical reasons, it is divided in four subvolumes optically similarly to the NT. Two short sections, called GCFront and GCRear facing the first and the last cell of the NT; and two long ones covering each of the detector sides called GCIN20 and GCD19 facing each of the correspondent surrounding experiments. The GC volumes are filled with a LS almost identical as the NT, not metal loaded and with less concentration of PPO.

Acrylic Buffer

A set of 48 photomultiplier tubes (PMT) is placed on top of the NT and GC cells, to collect all the scintillation light produced by the LS. The STEREO detector uses 8-inch Hamamatsu R5912-100 PMTs [56], which are characterized by a high sensitivity in the wavelength region of the scintillation light emission with a quantum efficiency of $\sim 35\%$ (bi-alkali photocathode) [65]. Prior to their installation, these PMTs have been tested and characterized to ensure an uniform gain. The PMTs are separated from the LS by a set of $20\,\text{cm}$ thick acrylic blocks, to optimize an homogeneous light collection from the cells. Each of the cells in the NT as well as the GCFront and GCRear are assigned a set of 4 PMTs, installed directly in each cells buffer. The remaining 16 PMTs are divided on top of the GCIN20 and GCD19.
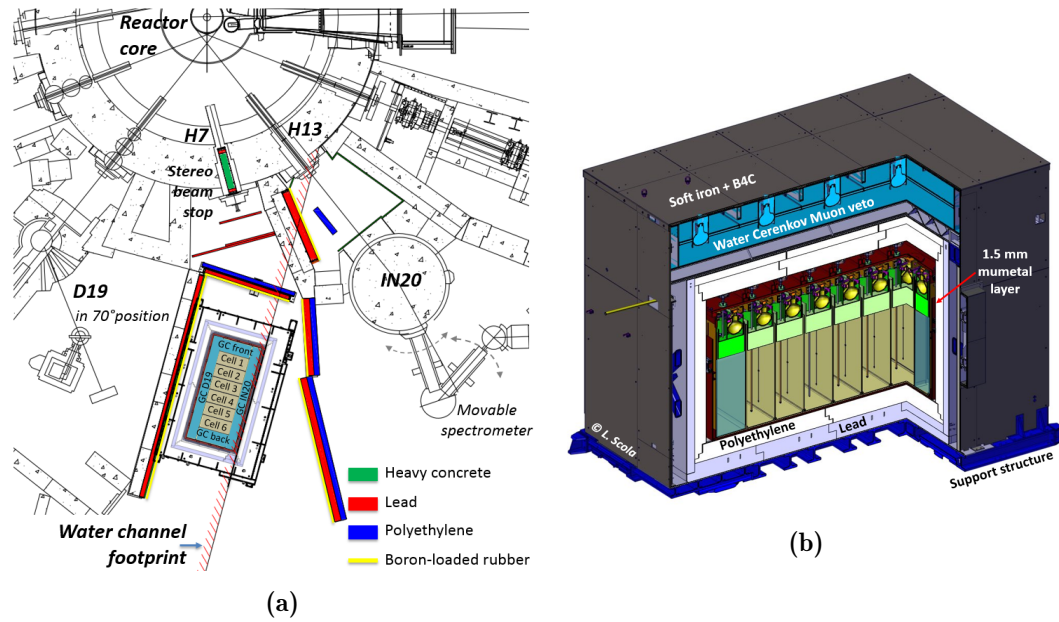
Figure 2.1.3: STEREO detector shielding **(a)** on site and **(b)** around the detector vessel [45].

VETO

Cosmic radiation through muon induced spallation can produce neutrons and γ-rays that mimic the IBD signature in the NT. These types of events are an important source of background in the STEREO detector, due to its position at ground level. The main measure against them is the implementation of a water Cherenkov muon veto (VETO) on top of the STEREO shielding. In Fig. 2.1.3b this volume of $396\,\mathrm{cm} \times 240\,\mathrm{cm}$ covering the detector is represented. The VETO tank is filled with a mixture of demineralized water and a wavelength shifter (4-Methylumbellifrene, 4MU) that optimizes the signal detection. The Cherenkov light is observed by a set of 20 PMTs with the same properties as the ones in the inner volume of the detector. The VETO detector observes a muon rate of $660\,\mathrm{s}^{-1}$ in average at a atmospheric presure of $1020\,\mathrm{hPa}$.

Shielding

The STEREO detector area is covered with different types of shielding. First of all, all of the PMTs in the detector (in the NT, GC, and VETO) are covered with a thin cylinder of mu-metal protecting the photocathode region, essential to minimize the loss of PE. Secondly, a mu-metal layer is safeguarding the detector vessel against magnetic fields. About 65 tons of borated polyethylene and lead are sheltering the inner volumes from external backgrounds and from cosmic muons, as represented in Fig. 2.1.3b. In addition, walls of soft iron are installed surrounding this shielding structure to protect the detector from any external magnetic field. Finally, several delimiting walls are installed around the detector. The region between the reactor core and the two neighbor experiments is covered with walls of borated polyethylene and lead. These materials are represented with blue and red areas in Fig. 2.1.3a, and help to moderate and capture neutrons, and to mitigate the γ-ray background respectively. Besides, the mechanical frames of the walls are covered by boron-loaded rubber to reduce the captures from neutrons in the steel, as it can be seen in the same figure by the yellow areas.

2.1.3 Electronics, DAQ and Monitoring

The STEREO detector has a designed electronic system to trigger and process the read out from the PMTs. Their signal is collected and amplified at first level in 8-channel front-end electronic boards (FE8). The FE8 and the PMT bases have a low level of electronic noise, that allows to detect small PMT signals. A first trigger threshold is applied from this front-end, adjustable to a signal amplitude or charge of individual channels in each of the parts of the detector. If this trigger is accepted, it is processed in a readout board (TRB) that determines the start time of the pulse, its total charge and the tail charge. These last two pieces of information are needed for the energy measurements and the event discrimination from the pulse shape information respectively. At this stage, the TRB can also apply a second level of trigger to reject unwanted events, with too low energy signals in some parts of the detector. Both electronic boards FE8 and TRB are contained in a single crate using the microTCA standard. All of the trigger and processing parameters are adjustable and can be set with the STEREO data acquisition (DAQ) software. This software is developed within the NOMAD [47] framework.

A set of sensors are located inside and outside of the detector volume, monitoring parameters such as temperature, absolute and relative pressures, liquid levels and magnetic fields. Their values can be retrieved from the DAQ system, together with other parameters as the PMT high voltages and currents, microTCA crate values and acquisition rates. Besides, two proportional counters are placed around the STEREO detector volume monitoring the neutron background rate.

2.1.4 Data Taking Timeline

The STEREO detector started data taking in November of 2016. After 2 reactor cycles it had to be retracted due to reactor maintenance in March 2017. Up to 66 days of reactor ON and 22 days of reactor OFF were collected during this period. Since some issues regarding the light collection and detector response were encountered during the first months, the collected data from that period was analyzed independently and defined as Phase I.

Defective acrylic walls were repaired during this period, in addition to some improvements in
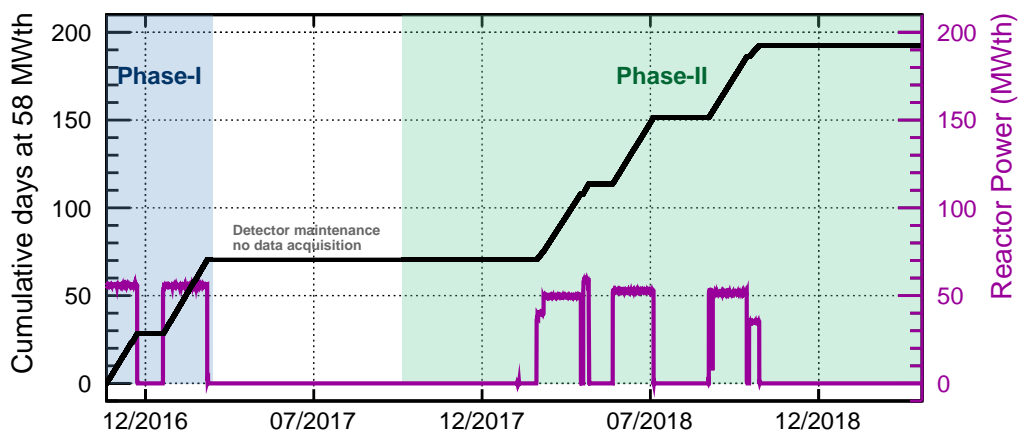

Figure 2.1.4: Data taking time line for Phase I and Phase II of the STEREO detector [4].

the calibration systems. The detector was back to data taking in October 2017 until April 2019 conforming the Phase II. The STEREO detector collected 119 days of reactor ON and 210 of reactor OFF. The time line of these two phases, together with the reactor power and the cumulative days are represented in Fig. 2.1.4.

Nowadays, the STEREO detector is taking data in its Phase III, characterized by the addition of a water wall as part of the detector shielding. It is expected to run at least until Summer 2020, reaching 300 days of reactor ON data. The presented results in this thesis correspond to the time line of Phase I and Phase II.

2.1.5   Calibration Systems

One of the most important features that needs to be monitored in a LS detector is its response. The STEREO detector is characterized by using two different sets of calibration systems: a LED system and a set calibration systems for source deployment calibration. Both methods and their impact in the study of the STEREO response are described in the following subsections.

LED Monitoring System

Two different LED systems are located in the STEREO detector. An array of LED illuminate each of the PMTs with low intensity light pulses on a daily basis, checking for variations of the response of the PMTs or electronic drifts in a short time scale. This method calibrates the PMTs gains, and monitors the light attenuation of the LS. Varying the intensity of the light pulses, the linearity of the PMTs and the electronics are studied over a dynamic range.
Another LED system included in the data acquisition board is placed within five identical boxes outside the shielding and illuminates NT and GC cells at three different heights, and the muon VETO. These LEDs emit UV light to excite and test the wavelength shifters of the LS. To ensure isotropic light emission, the light is carried from the LED boxes to teflon balls by optical fibers within the inner detector.

Source Calibration Systems

The detector response is studied with a set of γ and neutron sources, that can be used in three different calibration systems. The list of calibration sources used in the STEREO analysis are summarized in Table 2.1.1. The set of gamma sources has been selected in such way that it covers a wide range of energies, allowing to understand the energy spectra available for STEREO. The AmBe source is a $\gamma + n$ emitter that can be used for both gamma and neutron studies. More details about this source can be found in Chapter 3, and about its use in neutron capture efficiency studies in Chapter 4, 5 and 6.

Table 2.1.1: Gamma and neutron sources used for calibration of the STEREO detector [45].

Source	^{68}Ge	^{124}Sb	^{137}Cs	^{54}Mn	^{65}Zn	^{42}K	^{60}Co	^{24}Na	AmBe
$\mathbf{E}_\gamma$ [MeV]	0.511, 0.511	0.603, 1.690	0.662	0.835	1.100	1.524	1.170, 1.330	1.137, 2.750	γ - 4.443 n - [0, 11]
Activity [kBq]	90	2.4	37	90	3.3	3.3	50	5.9	$250 \cdot 10^3$ (^{241}Am)
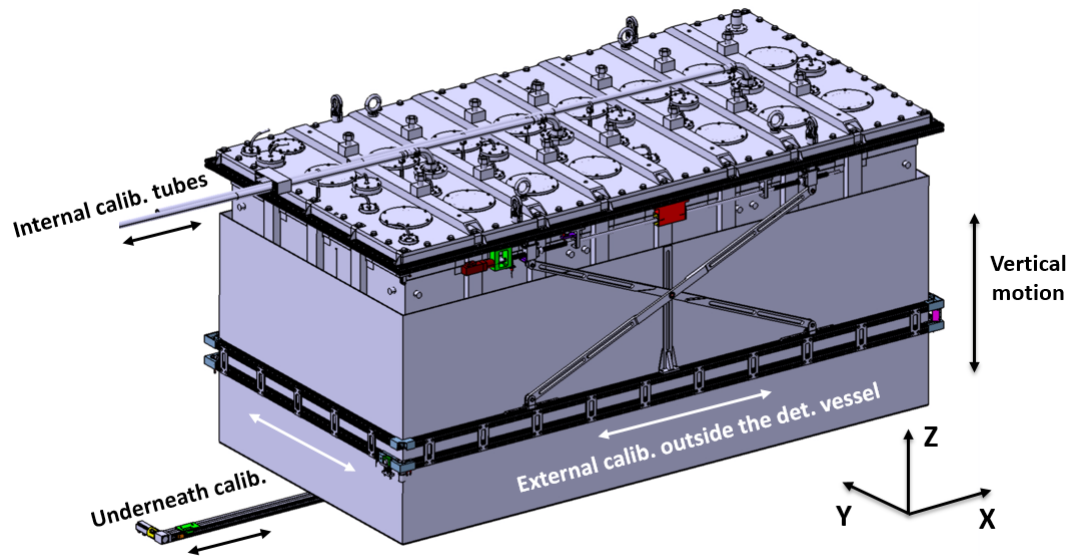
Figure 2.1.5: Sketch of the STEREO detector and its calibration systems [45].

The three different sets of calibration systems are depicted in Fig. 2.1.5, and are characterized by the way the source is deployed and the topology of the generated events. First of all, the *internal* calibration system is designed to deploy the calibration sources inside of the NT cells along 2 cm diameter steel tubes. These calibration tubes cross the cells from their top until 2.5 cm from the bottom of the cell. During Phase I, the internal tubes were located only within Cell 1, Cell 4 and Cell 6. The reactor maintenance after Phase I allowed STEREO to improve the calibration systems and introduce another set of calibration tubes in Cell 2 and Cell 5 for Phase II. More details about the calibration tubes position along the detector volume are described in Section 3.2.2. The internal calibration system is mostly used to study the detector response of the NT with the already mentioned γ sources (see Section 2.2.2), and neutron efficiency studies with the AmBe.

Secondly, an *external* calibration system is placed around the detector vessel. This is a semi-automatized system, and places the source along the perimeter of the detector at different heights between 90 and 15 cm above the NT cell floor. Its motion can be controlled by a dedicated software, allowing to map the desired position around the detector. The external calibration is designed to study spatial homogeneity, and to characterize the response of the GC with high statistics.

Finally, an *underneath* calibration system that crosses the detector longitudinally has been developed. This also semi-automatized system checks the detector response beneath the NT cells permitting to study the spatial inhomogeneities of the detector signal.
Weekly calibrations are performed with the ^{54}Mn source via *internal* deployment for energy reconstruction studies and performance monitoring, while monthly AmBe calibrations are performed for neutron efficiency studies. The rest of the sources are deployed in the detector calibration systems twice a year, in a specific calibration campaign in all of the calibration systems. The calibration runs are performed using NOMAD, with the specific DAQ trigger settings for each calibration system used and source deployed.

2.2 Data Analysis

The rest of this chapter is focused on the STEREO analysis. In the following subsection a detail description about the $\overline{\nu}_e$ spectrum prediction is presented. The way the detector response is treated, from the light collection in the PMTs until the signal is interpreted as reconstructed energy is explained in Section 2.2.2. Details about the Monte Carlo (MC) simulation and the neutrino data (DATA) analysis are presented in Section 2.2.3 and Section 2.2.4 respectively. The description of the absolute neutrino flux in STEREO is described in Section 2.2.5. Lastly, in Section 2.2.6 the fundamentals of the oscillation analysis in STEREO, the necessary parameters and the correspondent systematic uncertainties are summarized.

2.2.1 Neutrino Prediction

The predicted reactor $\overline{\nu}_e$ spectrum is necessary to estimate the number of IBD interactions expected to happen in the detector. The STEREO experiment uses the Huber model [57] of a pure ^{235}U fuel composition, using the FISPACT code [58]. No significant impact from the ^{239}Pu isotope is expected on the predicted emitted $\overline{\nu}_e$ spectrum, due to its low 0.7% mean fission fraction. The pure Huber ^{235}U spectrum needs to account for local effects on the reactor site. These local effects add a mean relative correction factor $\delta(E_\nu)$ on the Huber model of the $\overline{\nu}_e$ energy spectrum in the way:

$$E_\nu(Huber) \rightarrow E_\nu(Huber) \times (1 + \delta(E_\nu)) \ . \tag{2.1}$$

Three main effects are included in the STEREO evaluation of $\delta(E_\nu)$, whose impact is represented in Fig. 2.2.1,

- an *off-equilibrium* correction (red distribution), that accounts for fission products with life-time equal or larger than the time Huber model provides (12 h of irradiation);

- the neutrino contribution from beta decays produced by the spent fuel stored in the water channel above the STEREO detector after the reactor stop (blue distribution);

- the very high density of the fission elements in the core (green distribution), and the large amount of aluminum on them, together with the mechanics surrounding the reactor core (bean tubes and heavy water vessel).
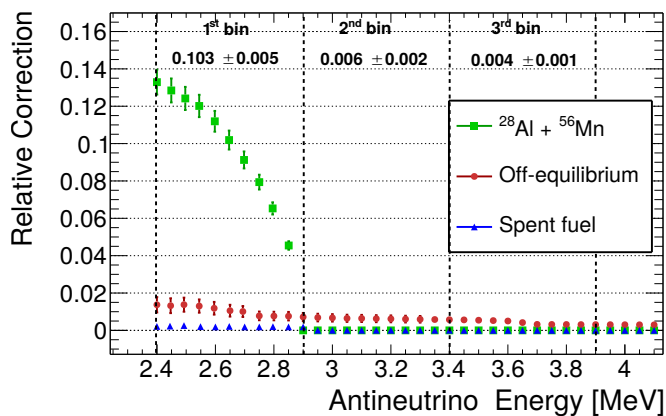

Figure 2.2.1: Relative corrections to the Huber model for the STEREO $\overline{\nu}_e$ spectrum: off-equilibrium (circles), residual $\overline{\nu}_e$ from spent fuel (triangles) and contributions of ^{28}Al (squares) [4].

These $\delta(E_\nu)$ corrections affect mostly the lower energy part of the $\bar{\nu}_e$ spectrum. About 10 millions of IBD events have been created for the STEREO analysis using the Huber $\bar{\nu}_e$ prediction of the spectral shape with these corrections.

2.2.2 Detector Response

A good energy scale is crucial for the STEREO data analysis. An inaccuracy in the reconstructed energy would cause a direct impact in the antineutrino spectrum, used to study the oscillation signal between cells. It is necessary to understand the PMT response, and the correspondent collected charge in the cells, and to monitor the light cross-talk between them. In the next subsection, all of these important pieces for the energy scale are described, together with the algorithm reconstructing the STEREO deposited energy, and the energy non-linearity studies applied on the MC simulation.

Light Collection

A first stage, the linearity of the PMTs and the electronics are studied using the LED calibration runs already described in Section 2.1.5. More information can be find in [45], where for all of the PMTs linearity deviations below 1% are observed.

After treating the specific response of the PMTs, the effect of depositing energy in a specific cell needs to be studied via calibration coefficients. An event is tagged in a certain Cell i by studying the charge barycenter position in the (x,y) plane, obtained using the PMTs location on that plane and the amount of charge collected by them. Knowing the volume with higher deposition, the mean total charge collected in the PMTs on that cell is studied for events with a full energy deposition (FED), represented with Q_i^{FED}. This value is compared to the expected mean deposited energy in the cell i obtained from MC simulations $E_{dep,i}$. This value is few percent smaller than the nominal γ-ray energy due to energy losses by Compton scattering. The calibration coefficient cc_i is then obtained by connecting both parameters as

$$\text{cc}_i = \frac{Q_i^{\text{FED}}}{E_{dep,i}} \ . \tag{2.2}$$

The calibration coefficients cc_i are studied with the weekly ^{54}Mn calibration runs in the internal calibration tubes. The obtained calibration coefficients show an agreement within 4% along the different heights of a cell [45]. In Fig. 2.2.2, the correction coefficients cc_i for the different cells in the NT and GC are represented for both Phase I and Phase II data taking periods.

Even if NT and the GC are cell-wise optically separated, some light cross-talks are expected between them. The study of these cross-talks is important to understand the collected light in a specific volume i. Light cross-talk coefficients $\ell\ell_{ij}$ are defined to represent the collected charge in the volume j when some energy is deposited in a single volume i,

$$\ell\ell_{ij} = \frac{Q_j}{Q_i} \ . \tag{2.3}$$

These parameters are evaluated in the STEREO experiment in two ways: using the FED of ^{54}Mn calibration runs at different heights of the NT cells; and using high energy events induced by cosmic-rays in the entire detector volume recorded during standard runs. Both methods have yielded consistent results. In Fig. 2.2.3, some of the obtained $\ell\ell_{ij}$ between different volumes of the detector are represented for both data taking phases. As explained in Section 2.1.4, during
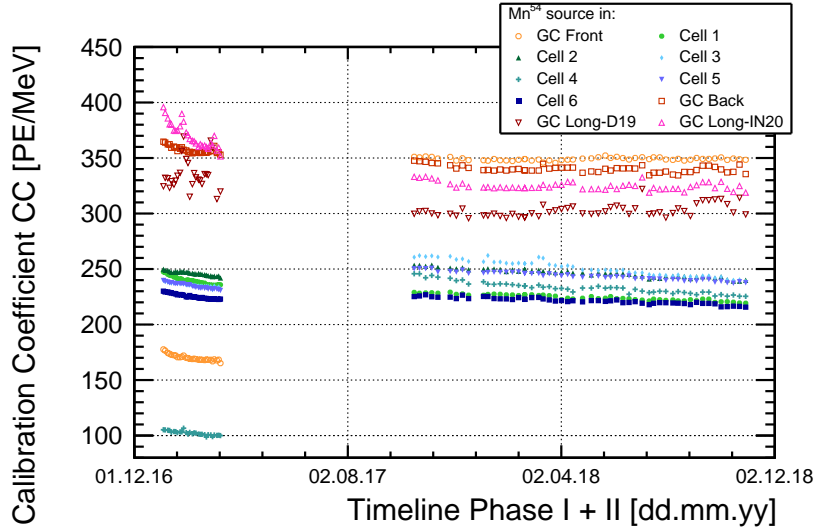
Figure 2.2.2: Time stability of the calibration coefficients cc_i for different cells of the detector volume [65].

Phase I an unexpected leakage of LS into some of the detector acrylic walls occurred, creating consequently an increased amount of light leaks in that cells. The effect was improved during Phase II after the acrylic walls reparation performed during the reactor maintenance period between both phases. It is important to remark that these increased amount of light leaks did not cause significant impact in the detector analysis since it was monitored during the entire process. Nevertheless, the systematic uncertainties of the energy reconstruction of Phase I were inevitably affected. More information about how the calibration coefficients cc_i and the light cross talk coefficients $\ell\ell_{ij}$ have been computed can be found in [65].
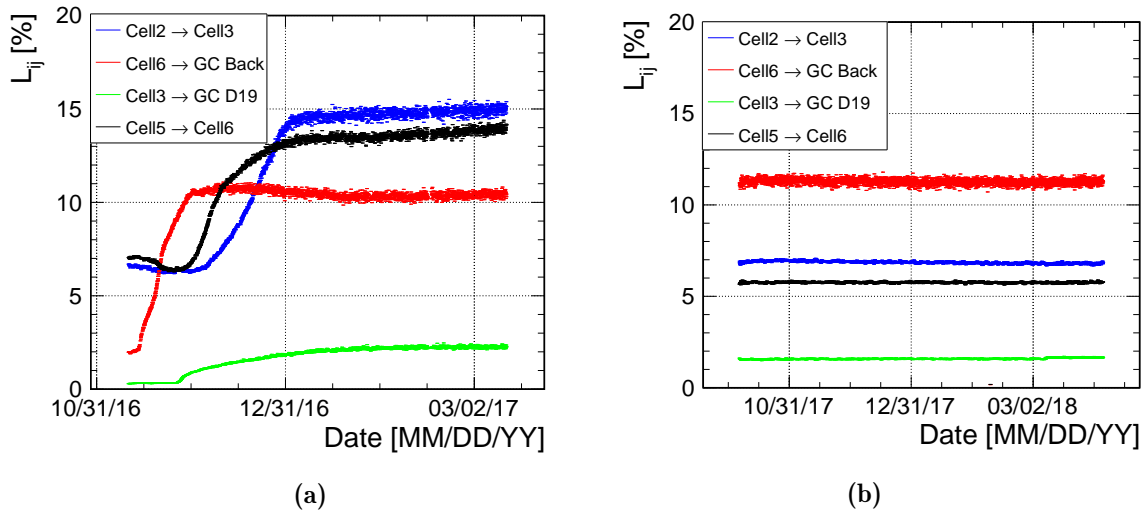
Figure 2.2.3: Examples of light cross-talks evolution during **(a)** Phase I and **(b)** Phase II [45].

Energy Reconstruction

The energy reconstruction algorithm connects the observed charge and the deposited energy in the detector. Considering an energy deposition E_i in a single cell i, the total charge Q_i collected is

$$Q_i = E_i \cdot \mathtt{cc}_i \ . \tag{2.4}$$

Due to the already mentioned light cross-talks, it is expected that a neighbor cell j also sees a total charge of

$$Q_j = E_i \cdot \mathtt{cc}_i \cdot \ell\ell_{ij} \ . \tag{2.5}$$

Therefore a energy deposition could be seen by all the detector cells (10 cells in total: 6 from the `NT` and 4 from the `GC`), and the formula is generalized to

$$Q_i = \sum_{i=0}^{9} E_i \ M_{ij} \ , \tag{2.6}$$

where the matrix notation $M_{ij} = \mathtt{cc}_i \cdot \ell\ell_{ij}$ has been introduced, and $\ell\ell_{ii} = 1$ by definition. Therefore, the deposited energy in the entire detector volume can be reconstructed as

$$\vec{E} = M^{-1} \ \vec{Q} \ . \tag{2.7}$$

The STEREO energy reconstruction algorithm uses this prescription and takes into account the `DATA` and `MC` discrepancies of the $\mathtt{cc}_i$ and $\ell\ell_{ij}$ via an iterative process that corrects them for both samples. The fine tuning of the parameters proceeds in the following way. The true energy distributions of the `FED` events are convoluted with the simulated detector response in reconstructed energy units. A Gaussian fit of the convoluted distributions gives the mean true energy deposited E^{true}. Also with a Gaussian fit, the reconstructed energy E^{rec} is obtained. The discrepancy of these two values is computed as,

$$\delta E_i = \frac{E_i^{reco} - E_i^{true}}{E_i^{true}} \ , \tag{2.8}$$

(a)

(b)
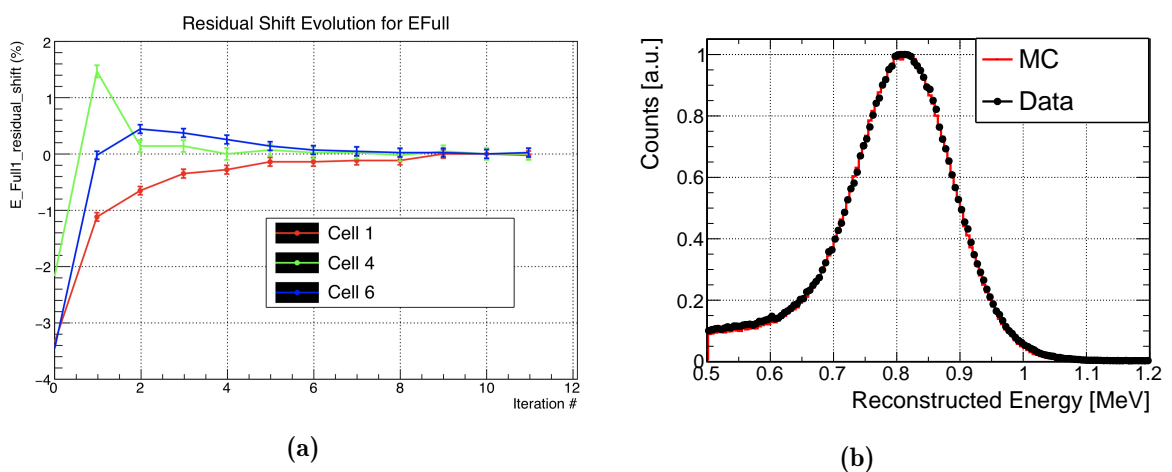
Figure 2.2.4: Energy reconstruction algorithm **(a)** fine tunning evolution shift [72] and **(b)** reconstructed energy γ energy from a deployment of the ^{54}Mn source at the center of `Cell 6` for DATA and MC [45].

representing how much differs the reconstructed energy from MC simulations with respect to the true energy deposition. This discrepancy is translated to the cc_i and $\ell\ell_{ij}$ as,

$$
\begin{aligned}
\delta cc_i &= cc_i \cdot \delta E_i \ , \\
\delta \ell\ell_{ij} &= \ell\ell_{ij} \cdot \delta E^{full} \ ,
\end{aligned}
\tag{2.9}
$$

where δE^{full} is computed in the same way as in Eq. 2.8, but for the entire detector volume (NT+ GC). The new cc_i and $\ell\ell_{ij}$ are obtained as

$$
\begin{aligned}
cc_i + \delta cc_i &\to cc_i' \ , \\
\ell\ell_{ij} + \delta \ell\ell_{ij} &\to \ell\ell_{ij}' \ .
\end{aligned}
\tag{2.10}
$$

The translated cc_i' and $\ell\ell_{ij}'$ are tested again to obtain their discrepancy with Eq. 2.8. This process is repeated a few times until variations of the order of 0.1% are obtained. The fine tuning evolution of these coefficients can be found in Fig. 2.2.4a. With this energy reconstruction method, coherent results between DATA and MC are obtained as it can be seen in Fig. 2.2.4b.

Energy Non-linearities

The calibration coefficients cc_i experience non-linearities caused by quenching effects on the LS response. The quenching of ionizing particles is described by the empirical Birks law [59]:

$$
\frac{dL}{dx} = S \frac{\dfrac{dE}{dx}}{1 + k_B \dfrac{dE}{dx}} \ ,
\tag{2.11}
$$

where $\frac{dL}{dx}$ represents the scintillation light emitted per unit path, S is the scintillation efficiency, and $\frac{dE}{dx}$ is the energy deposited per unit path. The Birks coefficient k_B is the parameter that
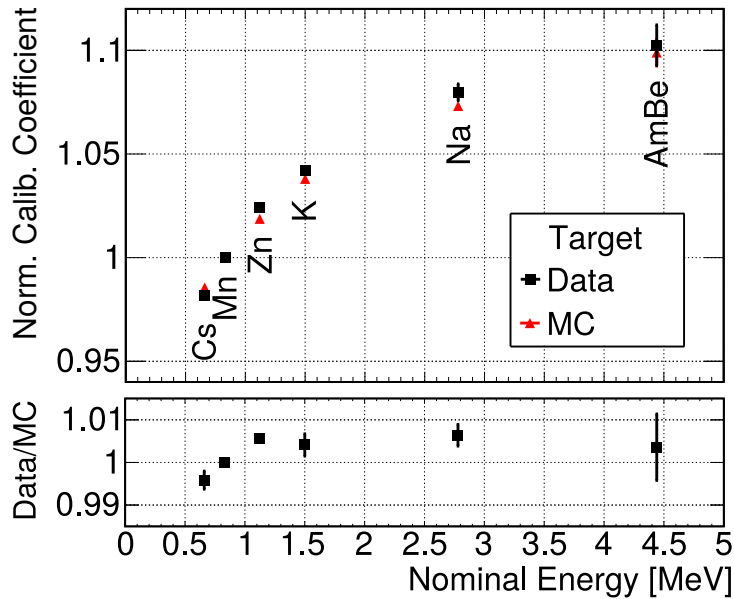
Figure 2.2.5: Quenching effect in the LS using different γ-ray sources. DATA and MC points are normalized to the ^{54}Mn anchor point [65].
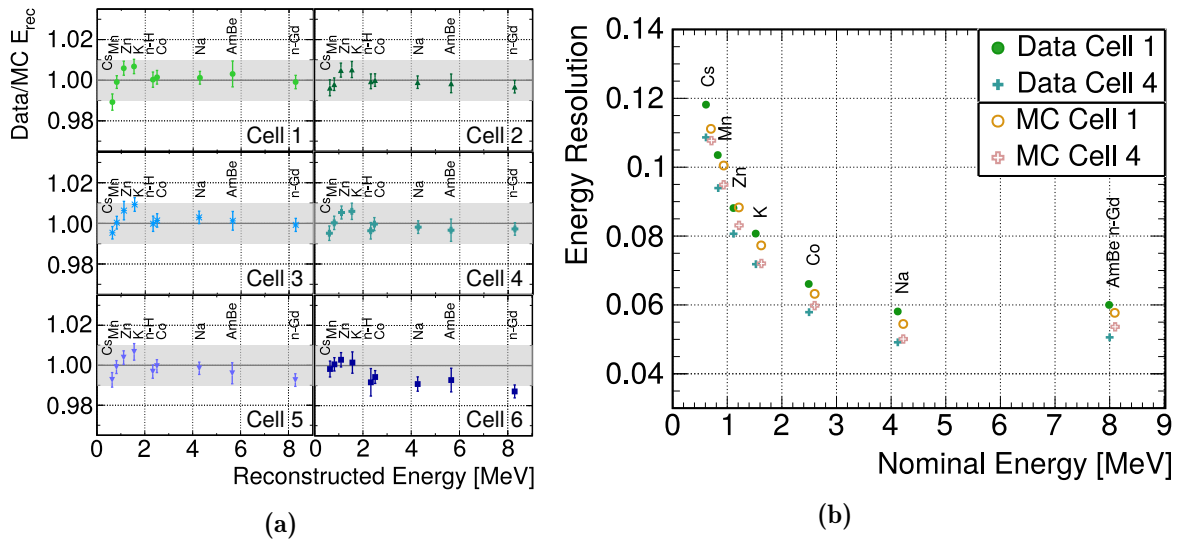
Figure 2.2.6: **(a)** Ratio between reconstructed energy in DATA and MC simulations versus nominal energy, **(b)** energy resolution versus nominal energy. For both distributions, different calibration sources using the averaged value from 5 vertical deployments [4].

represents the fact that the LS becomes less efficient at converting deposited energy into light for large $\frac{dE}{dx}$, which means for low energy ionizing particles. To match DATA and MC simulations, the k_B parameter has been tuned in the MC simulation. The set of γ source mentioned in Table 2.1.1 are used to compare DATA and MC simulations with different k_B values. The minimized DATA to MC discrepancy has been obtained for a value of

$$k_B^{ref} = 0.096 \pm 0.007 \text{ mm MeV}^{-1} \ . \tag{2.12}$$

The collected charge per MeV relative to the ^{54}Mn anchor point for different γ sources is represented in Fig. 2.2.5. As expected, the low energy γ sources have a more quenched signal than the ones at high energies. In the same figure it can be seen that DATA and MC values agree at the 1% level for all the energies with the obtained k_B value.

The k_B estimation forms an important piece in the computation of the detector response, but it is not the only parameter tuned in the simulation to match both DATA and MC. Additional details will be described in the following section regarding these other tuned parameters.

The calibration sources in Table 2.1.1 have also been used to show the reliability of the energy reconstruction for a wide range of energy and positions. For each nominal energy, the reconstructed energy and resolution of a full deposition peak are computed and represented in Fig. 2.2.6a and 2.2.6b. The DATA to MC reconstructed energies show an agreement within 1%. The energy resolution represents the $^1/\sqrt{E}$ law at low energy and saturates around 4% at higher energies, also well reproduced in the MC simulation.

2.2.3   Monte Carlo Simulation

The simulation framework of STEREO uses the `Geant4` toolkit (version 10.2) [60] to build the detector geometry, including the generic libraries of `GLG4sim` to introduce the LS properties (already used in experiments as KamLAND and Double Chooz, showing a good agreement with DATA samples). The simulated geometry includes the main mechanical parts, as the PMTs, the shielding components, the `VETO`, the calibration systems and the reactor building elements. Besides, the simulation includes also the information about the particle interactions from the energy deposition in the LS to the scintillation light collected in the PMTs. All of these implementations make the DATA and MC simulation analogous for both the detector response and analysis code implementation.

Special interest has been put in the implementation of the intrinsic properties of the LS. In addition to the already mentioned Birks k_B coefficient, other properties studied in the MC simulation have been the quantum yield of the fluors, the attenuation length, the light yield of both LS samples, or the `NT` proton number [61]. These parameters have been either measured in the laboratory, or fine tuned with a comparison with the DATA set.

The treatment of the optical reflectivity and transmittance of the acrylic separation plates between cells have been crucial in the STEREO analysis. The increased amount of light cross talks during `Phase I` presented in Section 2.2.2 was caused by leaks of LS into the acrylic *sandwich* wall (Fig. 2.1.2b), degrading its reflective capabilities. As a consequence a versatile description of the light cross talks between the cells have been implemented in the STEREO simulation by introducing individual filling levels for all the acrylic walls, together with an empirical model describing the effect of the liquid on the reflectivity [65].

One of the major improvements in the STEREO simulation has been the updated implementations of the neutron physics, with special emphasis on the neutron mobility and the gamma cascade released after its capture by Gd nuclei. The refinement of the thermal scattering improved the agreement between the simulated and the observed capture times [66], essential for the IBD selection described in the following section. The description of the de-excitation cascades of the relevant Gd isotopes have been significantly overhauled introducing the FIFRELIN model instead of the `GLG4sim` libraries [51]. The strong impact of both models in the energy spectra of the neutron captures and neutron efficiency values is seen along this thesis. Further details about both models are described in Chapter 5 and Chapter 6.

2.2.4   Neutrino Data Analysis

Neutrino Selection

As it was introduced in Section 1.2.2, reactor neutrinos interact in the LS via IBD creating a characteristic correlated signal. The STEREO detector uses a coincidence algorithm (`Stereo_Analysis`) based on time windows to select these correlated events (more details about this algorithm in Section 3.2.3). Table 2.2.1 presents the used IBD selection cuts, together with isolation cuts that contribution to the background rejection. All of them have been chosen to have an optimal signal acceptance and background rejection [74].

The main **selection** cuts are based in energy of the prompt and delayed signals, together with some coincidence time and position constraints. For the prompt event, an energy cut based on the expected spectrum of reactor neutrinos is chosen. Meanwhile, the delayed energy cut selects

Table 2.2.1: Selection cuts for IBD events [45].

	Prompt Cuts	Coincidence Cuts	Delayed Cuts
topology selection	$1.625\,\mathrm{MeV} < E^{\mathtt{DET}} < 7.125\,\mathrm{MeV}$	$2\,\mu s < \Delta T < 70\,\mu s$ $\Delta X < 600\,\mathrm{mm}$	$4.5\,\mathrm{MeV} < E^{\mathtt{DET}} < 10\,\mathrm{MeV}$
	$E^{\mathtt{Cell}} < 1\,\mathrm{MeV}$, neighbor cell $E^{\mathtt{Cell}} < 1\,\mathrm{MeV}$, other cell		$E^{\mathtt{NT}} > 1\,\mathrm{MeV}$
rejection	$\Delta T^{\overline{\mathtt{DET}}}_{before} > 100\,\mu s$, $\forall$ events with $E^{\mathtt{DET}} > 1.5\,\mathrm{MeV}$ $\Delta T^{\mathtt{DET}}_{\mu} > 200\,\mu s$ $\Delta T^{\mathtt{VETO}}_{\mu} > 100\,\mu s$ $Q_{PMTmax}/Q_{\mathtt{Cell}} < 0.5$		$\Delta T^{\mathtt{DET}}_{after} > 200\,\mu s$ $\forall$ events with $E^{\mathtt{DET}} > 1.5\,\mathrm{MeV}$

neutron captures by the gadolinium isotopes in the LS. A coincidence time selection removes a huge number of accidental coincidences. The 70 µs time cut allows to select neutrons after they are thermalized in the LS, while stopping muon events are avoided with the cut below the 2 µs. A set of **topology** cuts are used to optimize the cell tagging, while **rejection** cuts are used to avoid muon induced backgrounds in the detector. Both types of cuts have a strong IBD event acceptance, higher than $\sim 97.8\%$. The combination of all of these cuts makes the ratio of events in the NT ~ 0.99 compared to the other detector volumes.

Backgrounds

After the $\overline{\nu}_e$ selection, background events are still present in the DATA candidate events. To perform a proper DATA to MC comparison these events need to be subtracted. Depending on their source and the way they are eliminated from the $\overline{\nu}_e$ candidates, two types of backgrounds events are defined.

The *accidental background* conform uncorrelated events that randomly pass the selection cuts of the $\overline{\nu}_e$ coincidence selection. This type of events affect both, the prompt and the delayed candidates, and they are mainly caused by low energy gamma events. The accidental backgrounds can be evaluated by an *off-time* method that statistically subtracts them from the coincidence events. This method is thoroughly detailed in Chapter 3.
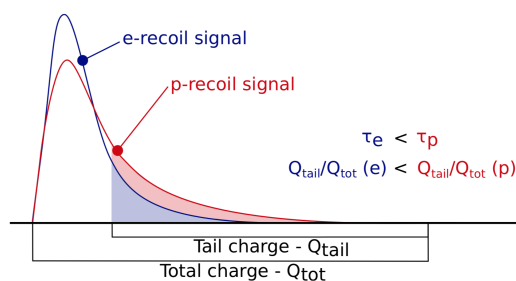
(a)
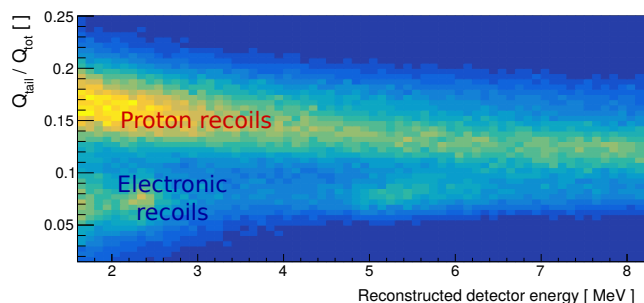
(b)

Figure 2.2.7: (a) Shape of the signal caused by electronic or proton recoil and **(b)** PSD values for each energy of the neutrino distribution [48].

The *correlated background* events are instead created by correlated processes that leave similar signature in the detector as the IBD. These type of events are mainly caused by cosmic rays inducing correlated signals, and can be studied during the reactor OFF periods. They can be classified in two types according to their origin: electronic recoils and proton recoils. to reject them, the PSD capabilities of the LS are used. Depending on the energy and mass of the particle, a different excitation regime of the organic molecules is reached leading to different de-excitation times during the production of scintillation light in the detector. The delay between the start of the integration time window of both, the entire pulse Q_{tot} and the tail of that pulse Q_{tail}, determines the PSD and its shape is presented in Fig. 2.2.7a. More concretely, both parameters create the characteristic PSD ratio Q_{tail}/Q_{tot} that allows to disentangle events in terms of their origin, as can be seen in Fig. 2.2.7b.

As mentioned above, the correlated background events are primarily created by cosmic rays, and thus the amount of events depends on the atmospheric pressure and the filling level of the water pool above the STEREO detector. The PSD shape dependency has been studied for all of the atmospheric and water level conditions proving a good agreement for both PSD contributors. Due to their stable shape, the obtained distributions provide a model of the background that can be used for a $\overline{\nu}_e$ extraction.

Neutrino Signal Extraction

The IBD candidates are directly extracted using the Q_{tail}/Q_{tot} distributions from the reactor ON and OFF periods. The obtained reactor ON and reactor OFF distributions are shown in Fig. 2.2.8, where the scaling parameter a have been introduced to correct the atmospheric pressure and water level differences between the two samples. This active extraction is performed for each cell and energy bin of Fig. 2.2.7b of size $500\,\mathrm{keV}$, using a binned log likelihood. In the end a normal distribution is used to fit the neutrino contribution, where its rate is obtained from its integral. Possible biases between the energy bins and cells are studied from pseudo-experiment simulations, and taken into account during the extraction [4].
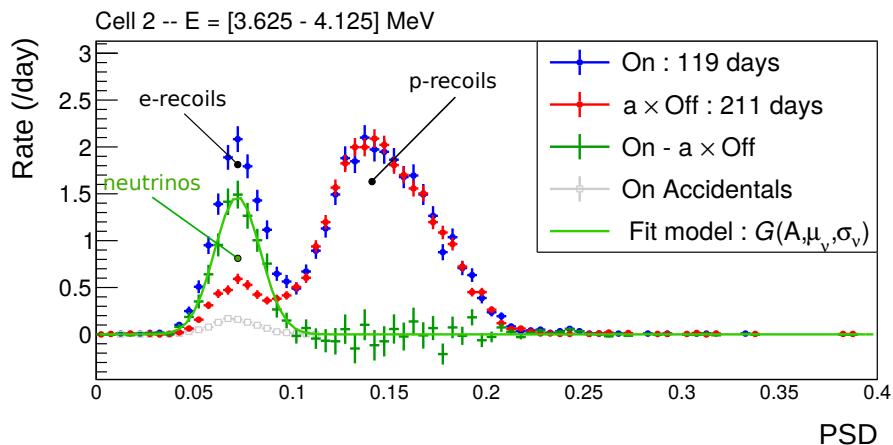
Figure 2.2.8: Example of the neutrino candidate extraction for one energy bin of Cell 2. The reactor OFF spectrum (red) is scaled to the reactor ON (blue) by the parameter a that accounts for the atmospheric pressure and water level discrepancies. Accidental contributions to the reactor ON or OFF events are statistically subtracted (grey). The difference between both samples (green) correspondes to the reactor neutrinos, and is fitted to a normal distribution [3].

2.2.5 Measurement of the Absolute Neutrino Flux

The study of IBD events in the STEREO experiment can provide not only information about the flavor oscillation, but also about the absolute neutrino flux from a highly enriched uranium reactor. For this evaluation, the observed neutrino rate needs to be compared to an expected value.

The number of IBD candidates observed in each cell can be obtained from the neutrino signal extraction in Section 2.2.4. The main effect observed when the different cells are compared is the dependency of the neutrino flux on the distance r from the reactor core. In Fig. 2.2.9, the measured neutrino candidates in each cell l ($N_{\nu,l}$) is represented with respect to the effective baseline r_l of each volume. The rate of observed events have been normalized taking into account the detection efficiency $\epsilon_{det,l}$ for each cell l. Since neutrinos are emitted isotropically from the reactor core, a geometric dilution of the events following the inverse-squared law [49] is observed:

$$\frac{N_\nu}{\epsilon_{det,l}} = \frac{N_o}{r^2} \ .$$

(2.13)

where N_o has been introduced as normalization parameter. The fitted function using this law is represented with a red line.

The observed neutrinos in the detector depend on the emitted spectrum from the reactor, the interaction probability and the detection efficiency. Therefore, for a prediction of the detected neutrinos flux ϕ_ν^{det}, a good modelization of the emitted neutrino spectrum is needed to built the observed to expected ratio. It can be obtained considering,

$$\phi_\nu^{det} = \phi_\nu^{em} \cdot \tau_{int} \cdot \epsilon_{sel} \ ,$$

(2.14)

where ϕ_ν^{em} corresponds to the emitted amount of $\overline{\nu}_e$ from the reactor core, τ_{int} the fraction of emitted neutrinos that interact in the detector, and ϵ_{sel} the detection efficiency on the entire detector. For the computation of the daily emitted neutrino flux, two different terms are considered [50]:
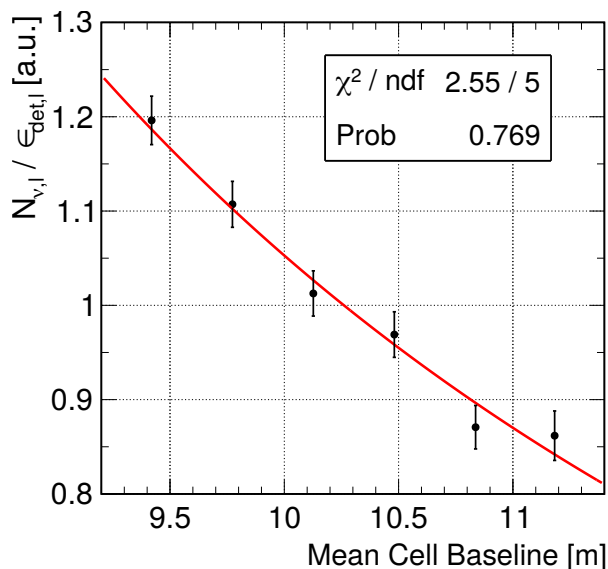

Figure 2.2.9: Measured neutrino candidates in each cell l with respect to its effective baseline. Values are fitted to $1/r^2$ model including a free normalization (red) [4].
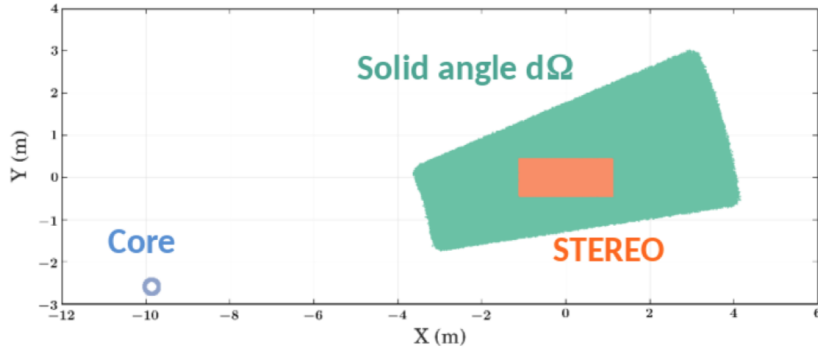
Figure 2.2.10: STEREO detector position with respect to the reactor core [78].

$$\phi_\nu^{em} = N_{\nu/fission} \cdot N_{fission/day} \qquad (2.15)$$

$N_{\nu/fission}$ represents the integral of the total number of neutrinos per fission under the corrected Huber model from Section 2.2.1; and $N_{fission/day}$ takes into account the number of fissions per day for a determined thermal power of the reactor. The fraction of simulated neutrinos τ_{int} is evaluated by considering the position of the STEREO detector with respect to the reactor core (see Fig. 2.2.10) and the IBD cross-section. The last term ϵ_{sel} considers the neutrino detection efficiency correction, which is evaluated as [50]

$$\epsilon_{sel} = \epsilon_{sel}^{\mathsf{MC}} \cdot \langle c_\varepsilon \rangle \cdot N_{proton} \ , \qquad (2.16)$$

where the first term $\epsilon_{sel}^{\mathsf{MC}}$ is defined as the ratio between the selected and the total amount of events, performed via MC simulation; $\langle c_\varepsilon \rangle$ provides the correction coefficients of the neutrino efficiency between DATA and MC; and N_{proton} is the proton number correction from the MC simulation (introduced in Section 2.2.3).

Results concerning the rate analysis of the STEREO $\bar{\nu}_e$ spectra will be published soon, but the evaluation of the neutron efficiency $\langle c_\varepsilon \rangle$ is the main topic of this thesis and it will be presented along Chapter 4, 5 and 6.

2.2.6 Sterile Neutrino Oscillation Analysis

Any sterile neutrino oscillation hypothesis is tested by the comparison of the IBD candidates from the Section 2.2.4 and a simulation sample without any oscillation via a χ^2 formalism

$$\begin{aligned}
\chi^2 = & \sum_{l=1}^{N_{\mathsf{Cells}}} \sum_{i=1}^{N_{\mathsf{E\text{-}Bins}}} \left(\frac{D_{l,i} - \phi_i M_{l,i}}{\sigma_{l,i}} \right) \\
& + \sum_{l=1}^{N_{\mathsf{Cells}}} \left(\frac{\alpha_l^{\mathsf{E\text{-}Scale\ unc.}}}{\sigma_l^{\mathsf{E\text{-}Scale\ unc.}}} \right) + \left(\frac{\alpha^{\mathsf{E\text{-}Scale\ c.}}}{\sigma^{\mathsf{E\text{-}Scale\ c.}}} \right) + \sum_{l=1}^{N_{\mathsf{Cells}}} \left(\frac{\alpha_l^{\mathsf{Norm\ unc.}}}{\sigma_l^{\mathsf{Norm\ unc.}}} \right) \ ,
\end{aligned} \qquad (2.17)$$

where this equation is formed by a comparison term between the number of measured neutrino candidates $D_{l,i}$, and the expected number of events $M_{l,i}$, and a set of pull terms ($\alpha/\sigma ratios$), for each cell l and energy bin i of the spectra. The number of expected neutrinos $M_{l,i}$ is adjusted to match the number of measured neutrinos on average. On one hand, the free parameter

Table 2.2.2: Overview of the uncertainties entering the oscillation analysis in the latest STEREO analysis [4].

Type	Contribution	Relative Uncertainty [%]
Normalization	Cell Volume	0.83
(cell-to-cell uncorrelated)	Neutron efficiency correction	0.84
Energy Scale	Mn anchor point	0.20
(cell-to-cell uncorrelated)	Cell-to-cell deviations	1.00
Energy Scale **(cell-to-cell correlated)**	Time stability	0.30

ϕ_i corrects the absolute rate of predicted events, making the expected amount of neutrinos independent of the spectrum prediction. On the other hand, $M_{l,i}$ are optimized to match the remaining deviations from each $D_{l,i}$ in terms of the oscillation parameters $\sin^2(2\theta_{ee})$, Δm_{41}^2 and the nuisance parameters $\vec{\alpha}$,

$$
\begin{aligned}
M_{l,i} &= M_{l,i}\left(\sin^2\left(2\theta_{ee}\right),\Delta m_{41}^2,\vec{\alpha}\right) \\
&= M_{l,i}\left(\sin^2\left(2\theta_{ee}\right),\Delta m_{41}^2\right)\cdot\left(1+\alpha_l^{\text{Norm unc.}}+S_{l,i}\cdot\left[\alpha_l^{\text{E-Scale unc.}}+\alpha^{\text{E-Scale c.}}\right]\right)\ ,
\end{aligned}
\tag{2.18}
$$

where $S_{l,i}$ are the sensitivity factors used to test the relative fraction of events shifted in the energy bins due to energy scale. The uncertainty $\sigma_{l,i}$ is extracted from the expected neutrinos

$$
\sigma_{l,i}=\sigma_{l,i}\left(\phi_i M_{l,i}\right)\ .
\tag{2.19}
$$

Due to the dependence of $M_{l,i}$ to the mixing angles, the statistical uncertainty $\sigma_{l,i}$ evolves with the rate predicted by the model. The used values for the pull terms of the χ^2 calculation are summarized in Table 2.2.2, and correspond to the uncorrelated and correlated uncertainties of the energy reconstruction ("E-scale unc./c." coefficient) and the normalization effects due to the detector cell volume and the correction factor of the neutron detection efficiency ("Norm unc." coefficient). Cell-to-cell correlated normalization parameters are not listed, since the oscillation analysis is insensitive to common shifts among detector cells. The shape of the prompt spectra obtained from the neutrino candidates for each cell are presented in Fig. 2.2.11 for each cell, together with the no oscillation model and the RAA best fit.

The null-hypothesis is tested with pseudo-experiments. Each one of these pseudo-experiment is fluctuated around the tested parameters $\sin^2\left(2\hat{\theta}_{ee}\right)$, $\Delta \hat{m}_{41}^2$,

$$
\begin{aligned}
\Delta\chi^2\left(\sin^2\left(2\hat{\theta}_{ee}\right),\Delta\hat{m}_{41}^2,\vec{\alpha}\right) &= \\
= \chi^2\left(\sin^2\left(2\hat{\theta}_{ee}\right),\Delta\hat{m}_{41}^2,\vec{\alpha}\right) &- \chi^2\left(\sin^2\left(2\theta_{ee}\right),\Delta m_{41}^2,\vec{\alpha}\right)\ .
\end{aligned}
\tag{2.20}
$$

By comparing the $\Delta\chi^2$ of the DATA with the distribution obtained from the pseudo-experiments the null-oscillation hypothesis can be tested.
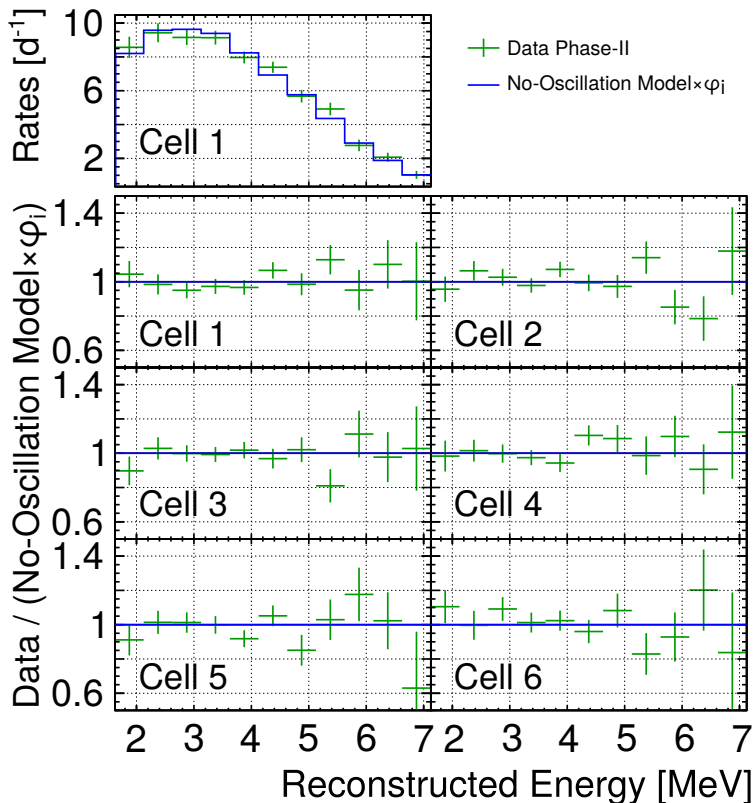
Figure 2.2.11: Absolute (top) and relative (bottom) comparison between the estimated rates of IBD events for Phase II in each cell (green) and the re-normalized no-oscillation model (blue) after a fit to Phase I+Phase II data [4].

2.3 Conclusion

Along this chapter, the status of the Stereo detector and its analysis have been shown. By the time of publication of this thesis (end of 2019), there are no new Stereo results about the rate analysis of the electron anti-neutrino flux from a pure ^{235}U reactor. Concerning the oscillation analysis, in Table 2.3.1 the up-to-date published results for the different data taking configurations are summarized. Concerning the oscillation analysis, the latest result shows a p-value of 0.09 [4], which means that the no-oscillation hypothesis can not be excluded. Rejection contours at 90% C.L. have been draw in Fig. 2.2.12 after a raster scan of the parameter space $(\sin^2(2\theta_{ee}), \Delta m^2_{41})$. The Stereo detector is able to reject the best fit point of the RAA at the 99.99% C.L. for the $\Delta m^2_{41} \sim 1\,\text{eV}^2$ value [4].

Table 2.3.1: Summary of the Stereo experiment published results, separated by data sample (phase) and number of reactor ON/OFF days [1, 2, 3, 4].

	Published	Phase	Reactor ON/OFF days	No-oscillation p-value	RAA best point excluded at
(i)	[1, 2]	I	66/138	0.34	97.56% C.L.
(ii)	[3]	II	119/210	0.40	99.00% C.L.
(iii)	[4]	I+II	179/235	0.09	99.99% C.L.
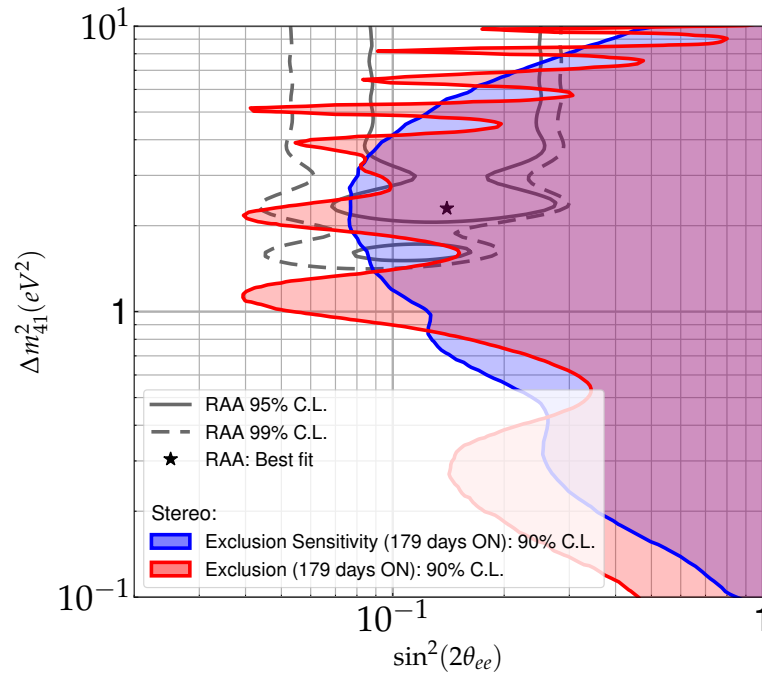
Figure 2.2.12: Rejection contour at 90% C.L. (red) compared to the expected sensitivity curve (blue) of Phase I+Phase II. Overlaid the allowed regions of the RAA (gray lines) and the best fit point (star) [4].

This thesis is focused in the study of the correction factors for the neutron efficiency, for both the absolute neutrino flux and the oscillation analysis. Both parameters haven been studied with the AmBe neutron source, deployed in the internal calibration tubes of the detector. Along the Chapter 3 the analysis of this source, and its signal in the STEREO detector is presented. The way the correction coefficients for the neutron efficiency are estimated will be detailed in Chapter 4. Lastly, in Chapter 5 and 6 the obtained neutron efficiency values are presented by comparing of the DATA samples with a MC simulation, using both the GLG4sim γ-cascade and the FIFRELIN model.

The AmBe as Neutron Source in the STEREO Analysis

Along this chapter a closer look into the neutron physics in an organic LS is presented. The signal of these particles in the detector is a direct consequence of their interaction with the particles of the LS, and its modelisation is deeply explained in Section 3.1. The AmBe source has been used in STEREO not only for its high energy $\sim 4.4\,\text{MeV}$ gamma emission that is useful for quenching studies [65], but also to study the neutrons emitted that can mimic the IBD delayed signal. The physics behind this phenomenon when the source is deployed in the internal calibration tubes along the NT cells are described in Section 3.2. This source can help to monitor the NT response by testing the energy reconstruction and the neutron capture correlation times. All the details of this complementary analysis are described in Section 3.3, being crucial for the test of the LS performance.

3.1 Neutron Physics in the STEREO Experiment

3.1.1 Interaction of Neutrons

Neutrons carry no electric charge, being particles that can travel long distances until they leave some energy in the detector. Their interactions depend strongly on the initial energy of the neutron, and they can be categorized in two different groups [52]:

- **Fast neutrons**, $E_n \gtrsim 1\,\text{eV}$:
  High energy neutrons mostly scatter on the medium, transferring a big fraction of their energy in one collision. The observable signal in this situation come as the recoil of the nuclei which takes a significant amount of energy from the collision. At each scattering, the neutron loses energy, being slowed down or *moderated*. The most efficient moderator is the hydrogen, since proton and neutron masses are on the same range. In this type of interactions, neutrons lose on average half of their energy in a single collision. Also, in this type of energy ranges, inelastic scattering with nuclei can take place.

- **Slow neutrons**, $E_n \lesssim 1\,\text{eV}$:
  The most common interactions in this energy range are elastic scattering with nuclei from the medium, where a little energy can be transferred to the nucleus each time. This type of interactions are responsible to bring the slow neutrons into a *thermal equilibrium* with the medium with an average energy of $\sim 0.025\,\text{eV}$ at room temperature. In many materials, slow neutrons are eventually detected by radiative emissions from the excited nuclei after a *capture* reactions $^A\text{N} + n \rightarrow\, ^A\text{N}^*$, process that plays an important part in the attenuation or shielding for neutrons.

For these reasons, neutron interactions have a combined cross section, a function of the neutron energy that depends on two components: the scattering cross section and the radiative capture cross section, $\sigma_{scatt.}$ and $\sigma_{rad.capt.}$ respectively,

$$\sigma_{tot}(\mathrm{E}_n) = \sigma_{scatt.}(\mathrm{E}_n) + \sigma_{rad.capt.}(\mathrm{E}_n) \ . \tag{3.1}$$

3.1.2 Neutron Interactions in LS

Neutrons from the IBD interaction are in the keV range, and are slowed down in the organic LS mostly by elastic scatterings with hydrogen atoms. A neutron loses on average half of its energy in each neutron-proton collision [52]. As it was highlighted before, this elastic scattering is the dominant interaction for neutron energies in the region between 100 MeV and 10 keV. Below these energies, radiative capture reaction gains importance. In the LS, the neutron capture is a competitive process within its components that depends on their capture cross section and abundance. The nuclei available for neutron capture are: hydrogen, carbon, oxygen or nitrogen. For the Gd-loaded LS volumes, captures can also occur on one of the Gd isotope from the $(\mathrm{Gd(thd)}_3)$ molecule. Among them, ^{157}Gd and ^{155}Gd are the most probable ones, having the highest thermal neutron capture cross section among any stable nuclei in the detector. In Table 3.1.1, a summary of the nuclei present in the LS can be found. By merely inspecting capture cross sections of the different nuclei, one could expect to only observe captures in Gd. However, two features play an important role here. First, the abundance of hydrogen nuclei in the LS is high ($\mathrm{N_H}/\mathrm{N_{Gd}} \sim 10000$). Second, the neutron capture cross section is energy dependent as it can be seen in Figure 3.1.1. For neutrons in the keV range that cross section in H is larger than for Gd. For that reason, neutrons do not need to be slowed down significantly to be captured in H, contrarily to the lower energy requirement for Gd. Considering these properties, a good understanding of Gd neutron capture fraction is crucial on organic LS for the study of IBD selection.
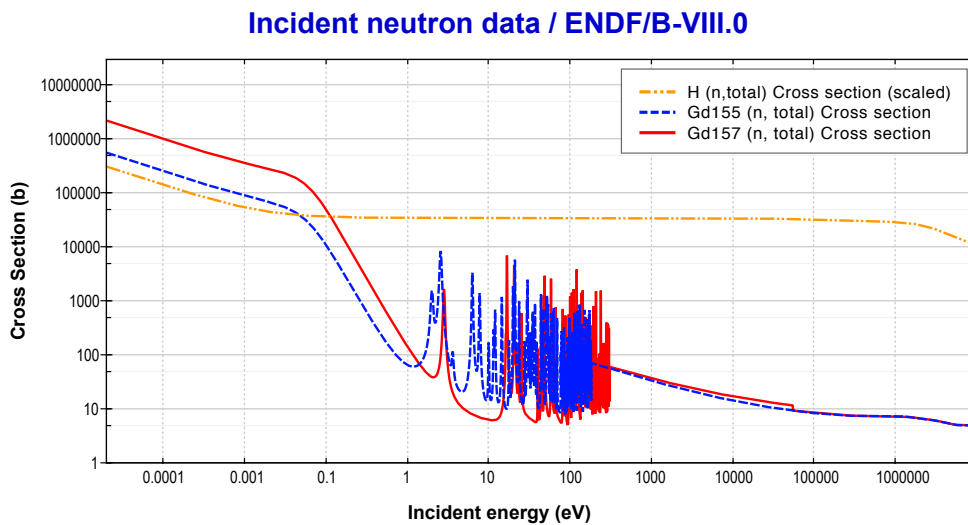

Figure 3.1.1: Evaluated cross sections for elastic scattering and neutron capture processes for ^{155}Gd, ^{157}Gd, and H (scaled to the STEREO concentration) using ENDF/B-VIII nuclear reaction data libraries [53].

3.1.3 Neutron Signals in LS

Neutrons interacting in an organic LS can be characterized by two main features. On one hand, in order to be captured, neutrons need to travel some distance before they reach the thermalization energy. Capture time depends on the physical process affecting the neutron moderation and can be modeled. On the other hand, the energy released upon a neutron capture gives a specific signal, which shape depends on the capturing nucleus and the energy containment of the detector. The main features of these two signals are going to be described along this subsection.

Released Neutron Capture Energy

Neutrons can be captured on the LS after their thermalization, releasing at least one γ from the deexcitation of the capture nuclei. For hydrogen or carbon captures, up to two γs are emitted equivalent to the Q-value of the process (see Table 3.1.1). However, ^{A}Gd captures

$$^{A}\mathrm{Gd} + n \rightarrow {}^{A+1}\mathrm{Gd}^* \ , \tag{3.2}$$

are followed by a cascade of γ emissions from the excited $^{A+1}$Gd* nucleus. The number of released γs is variable, and thus the mean visible energy is sometimes below the Q-value since their containment is more difficult in small detectors. The cause of this is that ^{158}Gd* nucleus is in a s-wave neutron capture resonance state S_n, with spin-parity $J^\pi = 2^-$. This is due to the nuclear selection rules and the ^{157}Gd ground state (GS) spin-parity $J^\pi = 3/2^-$. The transition between the excited state to the GS of ^{158}Gd (with $J^\pi = 0^+$) is via a cascade of an average of 4 γ emissions. The nuclear levels between the excited state and the GS are proportional to the excitation energy, and they split into two different types represented in Fig. 3.1.2a [55]: ***discrete levels***, with known spin and parity states; and a ***quasicontinuum*** where individual states and energy levels cannot be resolved. Intermediate transitions from the capture state to the GS can occur within the *quasicontinuum*, along the discrete levels, and between two levels from each of these connected regions. This fact makes both, the number and the energy values of the emitted γs difficult to predict. The shape of a γs cascade emitted from an enriched ^{157}Gd sample is represented in Fig. 3.1.2b. A good understanding of this γ-emission and its model is crucial to perform a DATA to MC comparison. Along this thesis, the STEREO simulation performance in terms of the neutron capture γ cascade emission is going to be thoroughly studied. As it was already mentioned in Section 2.2.3, two different models for the γ emission have been implemented in the STEREO simulation: the GLG4sim package, and the FIFRELIN model. More

Table 3.1.1: Nuclei in the LS that can induce a neutron capture. Left column, organic components present in the LS. Right column, all the gadolinium isotopes and their natural abundance, cross-sections and Q-values for radiative thermal neutron capture reactions [54].

Isotope	Cross section [b]	Q-value [MeV]	Isotope	Abundance [%]	Cross section [b]	Q-value [MeV]
^{1}H	0.332	2.223	^{152}Gd	0.2	735	6.246
^{12}C	0.004	4.945	^{154}Gd	2.18	85	6.436
^{16}O	$0.190 \cdot 10^{-3}$	4.142	^{155}Gd	14.8	61100	8.446
			^{156}Gd	20.47	1.5	6.359
			^{157}Gd	15.65	259000	7.857
			^{158}Gd	24.84	2.2	1.139
			^{160}Gd	21.86	0.77	5.321

(a) Gamma cascade transition scheme
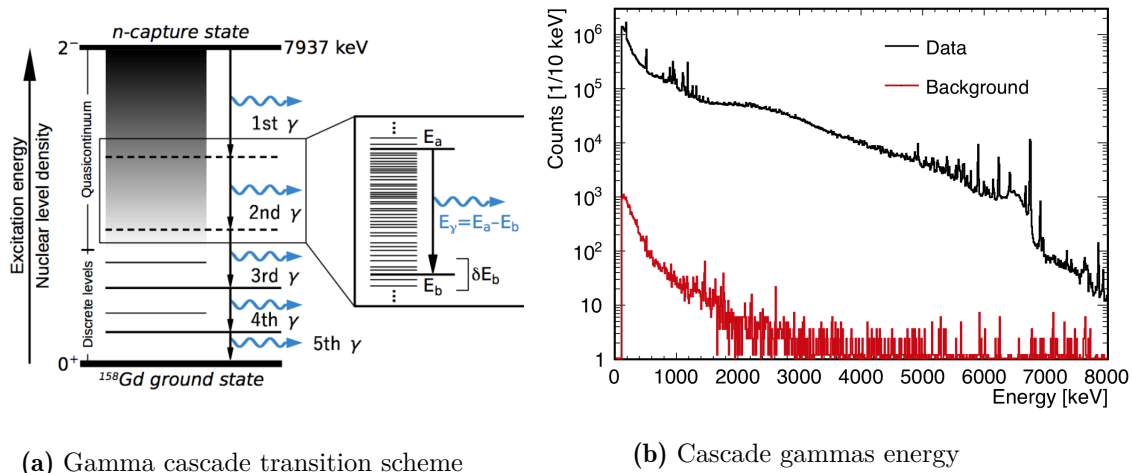
(b) Cascade gammas energy

Figure 3.1.2: (a) Scheme of the gamma cascade transition for ^{158}Gd from [55]. **(b)** Energy spectrum observed in the measurment with an enriched ^{157}Gd sample before background subtraction (black) and its correspondent background contribution (red)[55].

details about how these two models work, in addition to their gamma cascade multiplicity and simulated released energy, are described in the next chapters.

The Gd captures are followed by γ-rays of about $\sim 8\,\text{MeV}$. This total energy emission corresponds to the major gadolinium contributors, ^{155}Gd and ^{157}Gd with a Q-value $8.446\,\text{MeV}$ and $7.857\,\text{MeV}$, respectively. A good energy containment is crucial to identify and treat γ events. Specially for the high energy γs, which have been proven to play an important role in the γ-cascade [55]. Otherwise, if at least one of this γ scatters off the scintillator and escapes, only some fraction of its energy is registered in the detector. To maximize the neutron capture energy deposition, in this type of studies the entire detector (NT + GC) signal is considered.

Neutron Capture Time

Since neutron interactions with the LS depend on the particle energy, the neutron capture time is characterized by the three following factors. First, most of the neutrons lose their energy by elastic scattering. This process is described by an exponential distribution with a characteristic moderation time of $\tau_m \sim \mathcal{O}(100\,\text{ns})$. Second, neutrons slow down to the thermal equilibrium with the LS. This energy loss mechanism is less efficient, with a characteristic time $\tau_{th} \sim \mathcal{O}(1\,\text{µs})$. Finally, once thermalized, neutrons are captured with a characteristic time of about $\tau_{capt} \sim \mathcal{O}(10\,\text{µs})$. This value is intrinsic to the LS, and depends on the nuclei abundance. Since captures on Gd are much faster than on H ($\tau_{capt}^{\text{Gd}} \ll \tau_{capt}^{\text{H}}$), the τ_{capt} is mostly dominated by the gadolinium capture time. This value could differ if we go to the border areas of the NT, since neutrons can move to the GC (free of Gd nuclei) and be captured on hydrogen. In consequence, the overall neutron capture time description is a combination of these three process:

$$P(t) = \left(\frac{1}{\tau_m} e^{-t/\tau_m} \right) \otimes \left(\frac{1}{\tau_{th}} e^{-t/\tau_{th}} \right) \otimes \left(\frac{1}{\tau_{capt}} e^{-t/\tau_{capt}} \right) . \qquad (3.3)$$

However, considering the DAQ pile-up effects and the fact that the moderation time is much faster than the thermalization one $\tau_m \ll \tau_{th}$, the moderation component can be considered

negligible. Then, the previous equation is approximated to:

$$P(t) = \left(\frac{1}{\tau_{th}} e^{-t/\tau_{th}} \right) \otimes \left(\frac{1}{\tau_{capt}} e^{-t/\tau_{capt}} \right) = \frac{1}{\tau_{capt} - \tau_{th}} e^{-t/\tau_{capt}} \cdot \left(1 - e^{-t/\alpha} \right) \ , \qquad (3.4)$$

with,

$$\alpha = \frac{\tau_{th} \tau_{capt}}{\tau_{capt} - \tau_{th}} \ . \qquad (3.5)$$

3.2 AmBe Source Data

The AmBe source is used in the STEREO experiment as a $\gamma + n$ emitter. The source is manufactured by the Eckert&Ziegler company, encapsulated by a double layer of stainless steel of $7.8\,\mathrm{mm}$ of diameter and $10\,\mathrm{mm}$ height. It has an activity of $250\,\mathrm{MBq}$, and can be introduced in the STEREO detector by means of three types of calibrations systems.

On the next subsections, the way AmBe emits γs and neutrons and the applied event selection are explained. Moreover, the interaction properties of the neutron, and its correlated capture time and the neutron capture energy are studied.

3.2.1 AmBe $\gamma + n$ Products

The AmBe source is a homogeneous mixture of AmO_2 oxide and Be metal. First of all, ^{241}Am is obtained directly from plutonium upon absorption of two neutrons. It decays to ^{237}Np by emission of α-particle. This process has $432.2\,\mathrm{yr}$ of half life, and occurs with a Q-value of $5637.81\,\mathrm{keV}$ [62]. Although, most of the process energy is taken by the α-particle ($E_\alpha \leq 5545\,\mathrm{keV}$), a γ particle can also be emitted with low probability and energy $E_\gamma \leq 1015\,\mathrm{keV}$:

$$^{241}_{95}\mathrm{Am} \rightarrow ^{237}_{93}\mathrm{Np} + \alpha + \gamma \ .$$
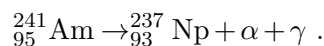
Secondly, ^{9}Be is used as target for the α emitted by the ^{241}Am, due to its high neutron yield, creating as a consequence an excited ^{13}C atom:

$$\alpha + ^9_4\mathrm{Be} \rightarrow ^{13}_6\mathrm{C}^* \ .$$
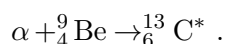
Its transition from this excited state to the GS is accompanied by a n emission, that is commonly followed by a γ. Several $\gamma + n$ channels are possible, and they are illustrated in Fig. 3.2.1a. The ones with the bigger probability on the ^{12}C electromagnetic transition are either the one going directly to the GS,

$$^{13}_6\mathrm{C}^* \rightarrow ^{12}_6\mathrm{C} + n \ ,$$
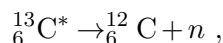
or the one to the first level excited state

$$^{13}_6\mathrm{C}^* \rightarrow ^{12}_6\mathrm{C} + n + \gamma_1 \ \text{with} \ E_{\gamma_1} = 4.438\,\mathrm{MeV} \ [63].$$
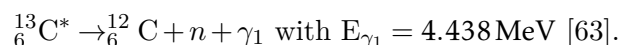
This second channel is the one used along this thesis for the neutron studies, and from now on, when a gamma of $4.438\,\mathrm{MeV}$ is emitted, it will be named γ_{AmBe}. In Table 3.2.1, the most probable particles emitted from the AmBe are summarized. The resulting free neutron distribution has a maximum value of about $\sim 11\,\mathrm{MeV}$, and follows a sub-structure of peaks. The energies and relative intensities of these peaks vary depending on the properties of the containment capsule of the AmBe source, and on the size of the AmO_2 and Be components in the powders employed. In Fig. 3.2.1b the energy distribution for simulated neutrons emitted by a AmBe source is represented. When no γ_{AmBe} is emitted (blue distribution), approximately 25%

(a) ^{12}C energy level diagram

(b) Neutron energy distribution

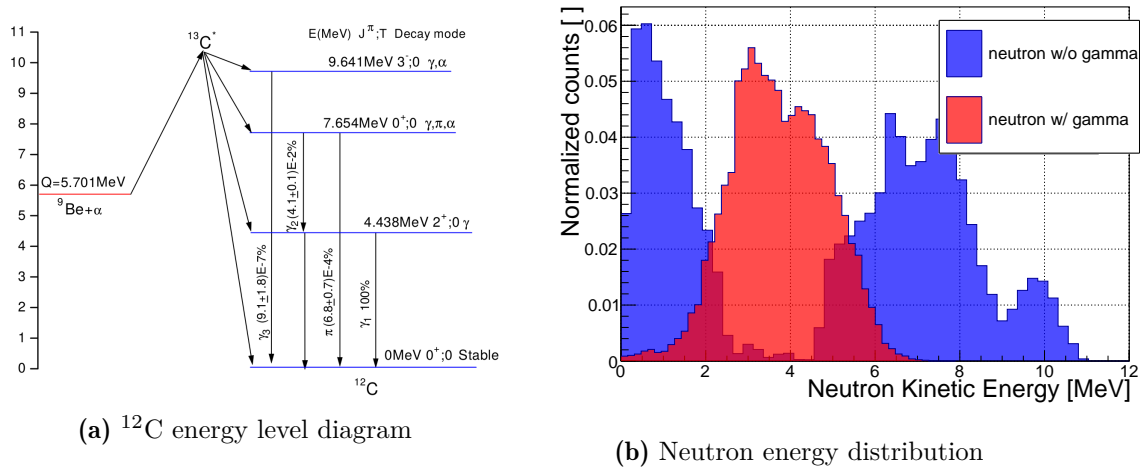**Figure 3.2.1:** **(a)** Diagram of the energy level for ^{12}C [63]. **(b)** True energy distribution for simulated neutrons emitted by AmBe source. In red, events where 4.438 MeV gamma has been mitted alongside the neutron. In blue, events where only neutrons have been emitted [65].

of the emitted neutrons have an energy of less than $\sim$1 MeV with a mean energy of $\sim$400 keV. Fast-neutrons are mostly created by ground level α transitions, or π emissions from the excited level with Q-value 7.654 MeV. When a γ_{AmBe} is created in the process (red distribution), the neutron energies are therefore restricted to a maximum value of $\sim$7 MeV.

The intensity of the ratio between such gamma and the corresponding n is a very important characteristic of this source, and it is estimated

$$R = \frac{S_\gamma}{S_n} = 0.596 \pm 0.017 \ [63] \ .$$

The calibration source used in the STEREO experiment emits $15 \cdot 10^3$ neutrons per second, and a rate of 10^3 s^{-1} gammas. Even if these two particles are created at the same time, neutrons will need additional time to deposit visible energy in the detector. A time selection criteria allows to separate the γ_{AmBe} signal from the released neutron capture gammas.

Table 3.2.1: $\gamma + n$ yield per 10^6 primary α particles of AmBe source [63].

Particle	Energy [MeV]	Intensity	Emitted from
n	Spectrum (0-12)	70	^{9}Be - (α, n) reaction
γ	4.438	41.7	^{9}Be - (γ, n) reaction
γ	0.0595	$3.59 \cdot 10^5$	^{241}Am - (α, γ) reaction
γ	0.0263	$2.41 \cdot 10^4$	^{241}Am - (α, γ) reaction

Table 3.2.2: Labeled positions of the AmBe when it is used for internal calibration

Position [cm]	Label	Phase
80	*top*	I+II
60	*top-center*	II
45	*center*	I+II
30	*center-bottom*	II
10	*bottom*	I+II

3.2.2 Source Deployment

The STEREO detector is characterized by three different types of calibration systems, already mentioned in Section 2.1.5. Only DATA from the internal calibration system is used for the analysis of this thesis. The internal calibration tubes allow the source to be placed at different heights in the NT cells. These heights are labeled with respect to the bottom of the cells (z=0 cm) and their nominal values are summarized in Table 3.2.2. However, this labeling does not take into account the size of the capsule that is holding the source, nor the position of the source with respect to the source holder. For that reason, a ~ 3 cm extra shift with respect to the listed nominal position has been taking into account in the simulation. The AmBe source has been deployed through the internal tubes in a monthly basis. In App. A the calibration days, cells, and positions are summarized. During the entire data taking of the detector, two different configurations have been used for the internal calibration performance modeling. In the time of Phase I, only three positions have been considered: *top*, *center*, and *bottom*. Besides, only the calibration tubes in Cell 1, 4 and 6 have been used. In contrast, the amount of data was significantly incremented during Phase II by the addition of two more positions in the deployment heights list (*top-center* and *center-bottom*), and the use of a calibration tube in Cell 2 and 5 allowing more refined studies.

As it has been seen along this thesis, the position of the source inside of the detector is essential for any study of the neutron interactions. Consequently, the height of the source along the z-axis direction is not the only thing needed, but also the relative position of the calibration tubes with respect to the detector volume. In Fig. 3.2.2, the NT volume on the xz-plane is sketched, together with a representation of the xy-plane of one of the cells. As it can be seen, the calibration tubes are neither placed in the center of the cells along the x- nor y-axes. These shifts of positions have an implication in the analysis of neutron interactions, as it will be seen in Chapter 5 and Chapter 6.
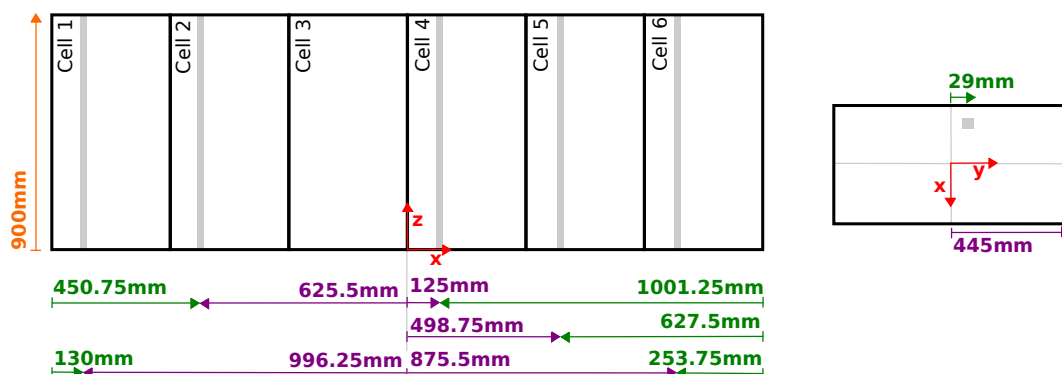
Figure 3.2.2: Internal calibration tubes position in the detector.

3.2.3 Event Selection

To isolate neutrons from γ_{AmBe}, a coincidence search has been applied to the AmBe data. This coincidence selection has been performed with the dedicated `Stereo_Analysis` algorithm. It loops over all the tagged events during the data acquisition (see more information in Section 2.1.3), and applies a time cut to the last three events (`CurrentEventsVector`). Two characteristics are analyzed for the correlated selection search: the time stamp, and the reconstructed energy in the detector. The selection cuts applied over the AmBe data are summarized in the following subsections, and a schematic representation of the selection cuts is shown in Fig. 3.2.3.

Pre-selection

A set of preliminary cuts are applied to all events. They check if any of the listed events in the data file is created by a cosmic μ interaction with the detector. The considered selection cuts to tag such event are: charge in `VETO` volume should be $Q_{\mathtt{VETO}} > 80$ p.e. and the energy in the detector volume $E_{\mathtt{DET}} > 20$ MeV.

AmBe Search Coincidence

The `CurrentEventsVector` is analyzed to see whether it contains a $\gamma_{\mathrm{AmBe}} + n$ pair of events. Firstly, the γ_{AmBe} (prompt event, first element in the `CurrentEventsVector`) is expected to deposit energy in the detector between [4, 7] MeV. Secondly, the released γs after a neutron capture (delayed event, second element in the `CurrentEventsVector`) are expected to occur between 0.5 and 100 µs after the prompt event. To have a clean signal coincidence, a time isolation cut is applied between the 4.4 MeV γ event, the last muon and the next-to-next trigger event. These cuts are summarized as:

AmBe selection cuts

- **Prompt event (cut to select $\gamma_{\mathbf{AmBe}}$):**

  - $4 \leqslant E^{\mathtt{DET}} \leqslant 7$ MeV
  - at least 100 µs after the Last Muon
  - at least 150 µs with reference to next-to-next trigger event

- **Delayed event (cut to select neutron captures):**

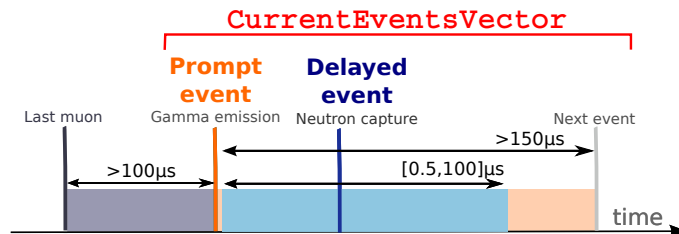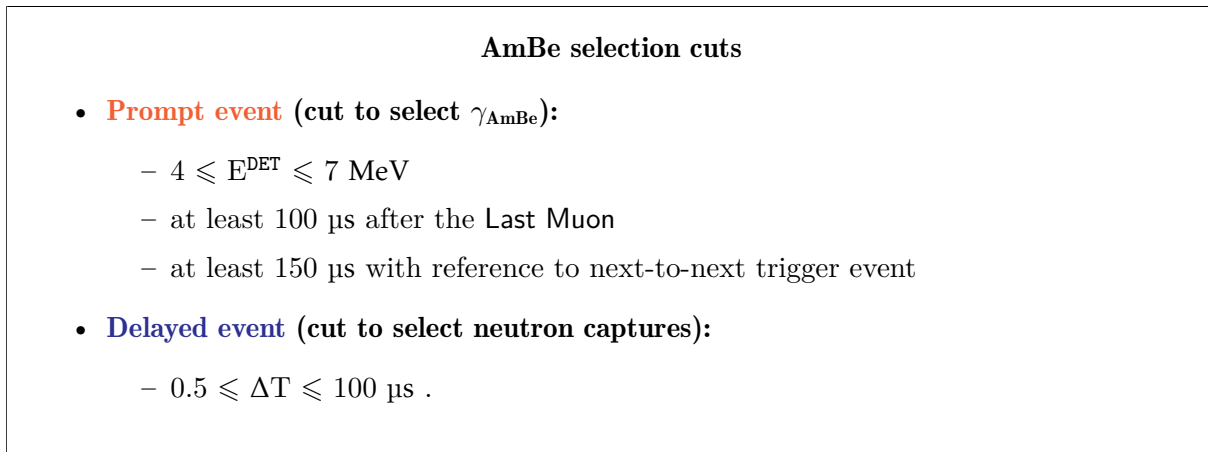 - $0.5 \leqslant \Delta T \leqslant 100$ µs .

Figure 3.2.3: Schematic representation of the `CurrentEventsVector` and the AmBe coincidence search cuts.

Background Subtraction

Due to its clear and powerful signal, AmBe events are expected to be almost background free. Nonetheless, there are several types of events unrelated to the source that can produce a false coincidence. Some possible background combinations are:

- **single events** considered as **delayed**, and correlated with a real prompt AmBe events,

- **two single events** forming a false coincidence,

- **two AmBe events** occurring too close in time, effectively mismatched as prompt and/or delayed events.

These events can be accidental coincidences, or correlated background events from the AmBe source. For simplicity, these events are named accidental background. A possible way to measure accidental events is using the *off-time window method*, depicted schematically in Fig. 3.2.4 and explained in text box **Time-window measurement**. This method estimates statistically the probability that a accidental coincidence occurs. On the `Stereo_Analysis` code this method is repeated every time a prompt candidate of AmBe is found, being stored at the same time the correlated AmBe events and the accidental ones.

Time-window measurement

1. every time the `CurrentEventsVector` fulfills the coincidence pair criteria, the time stamp of the *prompt* event (t_{prompt}) is saved on a `PromptEventsList` as the last entry;

2. a loop along `PromptEventsList` looks for the time stamp of the events and its position with respect to the current *prompt* event, taking into account the number of background windows n_{BG} and their time shift Δt_{vp}:

    - if $(t_{prompt} - t_0) > n_{BG} \cdot \Delta t_{vp}$, the `event 0` is erased and it continues the loop;
    - else if $(t_{prompt} - t_0) \leq n_{BG} \cdot \Delta t_{vp}$, the `event 0` is used to perform the accidental search and the loop is stopped;

3. the saved list `event 0` is shifted along the time space as much as the number of background windows pre-established in the code (with Δt_{vp} time shift) creating the so-called *virtual prompts*. This loop is finished as soon as the position of the *virtual prompts* is between the current prompt and delayed event;

4. for each of these *virtual prompts*, single candidates matching the delayed event AmBe selection criteria are searched;

5. if a single event is observed in this window, it is considered as a background **off-time event**. Both the information about the *virtual prompts* and the delayed **off-time event** are saved and tagged as *accidentals*.
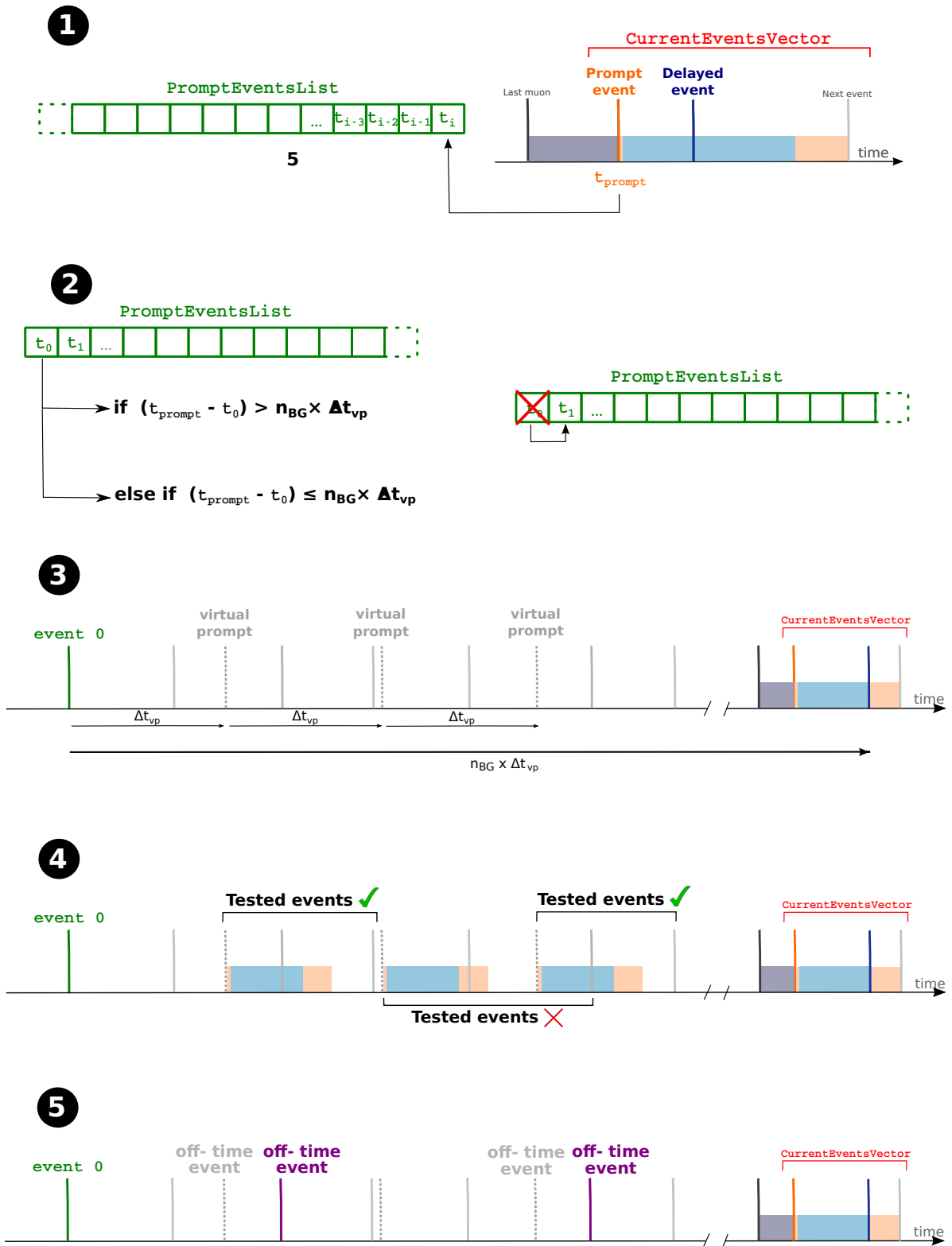

Figure 3.2.4: Schematic representation of the off-time window method for the accidental subtraction.

The accidental search presets used for the AmBe pair search are:

- number of background windows $n_{\mathrm{BG}} = 10$;

- and virtual prompt offset $\Delta t_{vp} = 1000\,\mu s$.

At the end, the number of coincidences is obtained by the statistical subtraction of the accidental events to the correlated backgrounds. However, in order to compare the off-time and on-time ones, a proper scaling factor must be applied. Together with the amount of off-time events per prompt and the number of background windows used, it should be also considered a correction factor coming from the detector dead-time response. This correction factor is estimated considering that at large correlation times, both on-time and off-time distributions should be identical.

3.2.4 Detector Signal

After the coincidence search and the accidental background subtraction, neutron capture time and energy distributions are useful parameters to study the neutron behavior in the entire STEREO detector. In the following subsections a deep look into these spectra is taken.

Neutron Capture Energy Spectra

Neutron capture energy spectra are one of the important outputs of the AmBe calibration. Then, a good subtraction of accidental events is necessary to achieve a pure and clean neutron event signal. In Fig. 3.2.5a, the energy distributions for the on-time events and its corresponding off-time contribution are represented. The accidental events contribute only to the visible energy at low energies with single events. On one hand, the peak events with $E_{delayed}^{\mathrm{DET}} < 1\,\mathrm{MeV}$ are not related to the AmBe source. There are indications that these events are caused by external effects, since their intensity varies in terms of time (for different calibration dates) [70]. While their correlation time with the prompt event remains constant as pictured in Fig. 3.2.5e. However, some events creating a less prominent peak around $1.2\,\mathrm{MeV}$ can be tracked down to the AmBe source, concretely to the γ emission correlated to the α particle creation from the Am decay. On the other hand, for energies greater than $1.5\,\mathrm{MeV}$, off-time events are mostly observed as correlated backgrounds. Two examples of this correlated background are neutron-neutron coincidences with energy contribution near to H and Gd neutron capture peaks, or wrongly selected γ_{AmBe} events, creating an excess in the $4.4\,\mathrm{MeV}$ region.

In MC simulations, it is also important to apply an accidental events subtraction. In the off-time window method, not only single events are evaluated, but also correlated background events coming from the high activity and rate of the source. As it can be seen in Fig. 3.2.5b and Fig. 3.2.5f, high energy events ($E_{delayed}^{\mathrm{DET}} > 1.5\,\mathrm{MeV}$) are taking part in the on-time selected events in a similar way as in DATA. The subtraction of these events on the MC simulation allow to have a good agreement with DATA, key factor for the efficiency studies. On Fig. 3.2.6a, the final neutron capture energy spectra in DATA and MC is represented. These spectra show the good agreement between both distributions, consequence of the correct implementation of the coincidence search and the accidental subtraction. Note that, in this case, the FIFRELIN model is implemented for the Gd n-capture gamma cascade in the MC.
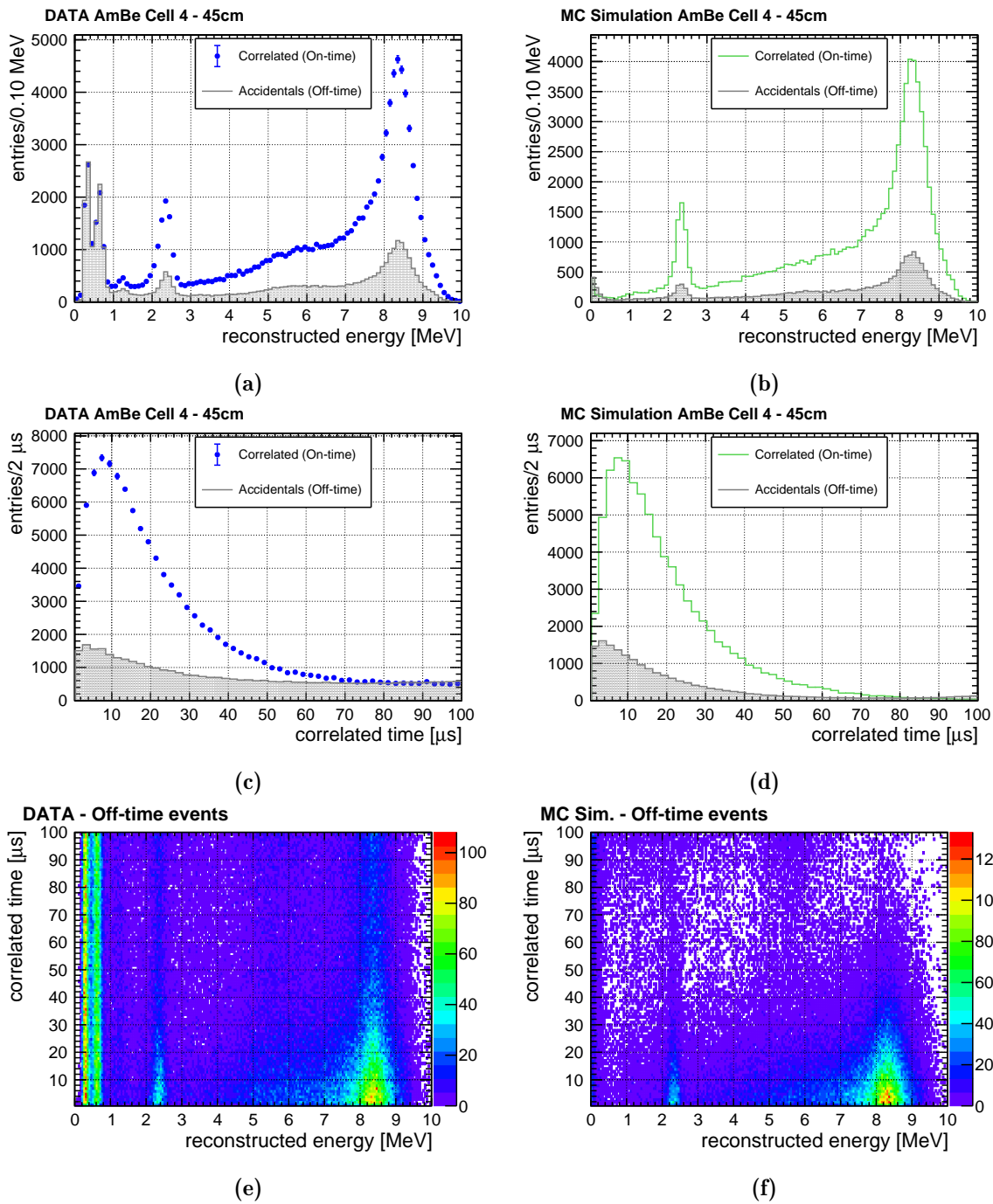
Figure 3.2.5: Energy and correlation time distributions before accidental background (gray) subtraction. Both spectra are represented for DATA (blue) and MC (green) simulations, using the AmBe source at the *center* of `Cell 4` the `20180619`. MC Simulation distributions are scaled to the DATA ones. Uncertainties for DATA are only statistical.

Neutron Capture Time Spectra

Neutron capture time is also an important output from the neutron studies, and its shape is described in Eq. 3.4. In the same way as the reconstructed energy spectra of neutron capture, the accidental subtraction is a very important feature for the capture time studies. On-time correlation time distributions and its correspondent accidental contribution are represented in Fig. 3.2.5c. As it can be seen, accidental events are dominating at long correlation times. This is because these correlated events are not coming from the same initial process. If one takes into account the relation of these events and their reconstructed energy (Fig. 3.2.5e), it is possible to see the previously mentioned uncorrelated low energy events ($E_{delayed}^{DET} < 1.5\,\text{MeV}$). Some of these are also caused by a single event in coincidence with a neutron, creating less prominently the capture lines in H or Gd energy regions. It should also be noted that accidental events are not flat in the correlation time distribution. Neutron-neutron correlated events are also present due to the high activity of the source. The proximity of these two events in time contribute with low correlation time events (below $30\,\text{µs}$) in the accidental spectrum, creating two islands at approximately $2.2\,\text{MeV}$ and $8\,\text{MeV}$ in Fig. 3.2.5e. Looking in the same way to the MC simulations in Fig. 3.2.5d and Fig 3.2.5f, accidental correlations are only caused by neutron-neutron coincidences. This creates a spectrum of accidental events with only contributions at low correlation times $\Delta T \leq 30\,\text{µs}$. The subtraction of these events is important to remove the same neutron-neutron events in both DATA and MC samples. Another important application of the correlation time spectra in MC simulations is the neutron mobility studies. When the source is deployed in the border areas of the NT (like in `Cell 1` or `Cell 6`) a flatter distribution is also observed for long correlation times. This is caused by the neutrons traveling to the GC and being captured on hydrogen nuclei there. Since they need to travel to another volume, their capture time is larger. It is important to remove these high correlation time events in both DATA and MC simulations since some of neutron interactions and processes are not completely well simulated, and they could interfere with other neutron studies like the capture efficiency (mentioned in future sections and chapters). In conclusion, in Fig. 3.2.6b the final neutron capture correlation time distributions for DATA and MC simulations are represented. Both spectra are in good agreement, with only some small tension on the first two bins (below $5\,\text{µs}$) caused by simulated artifacts regarding the neutron interaction at high energies.

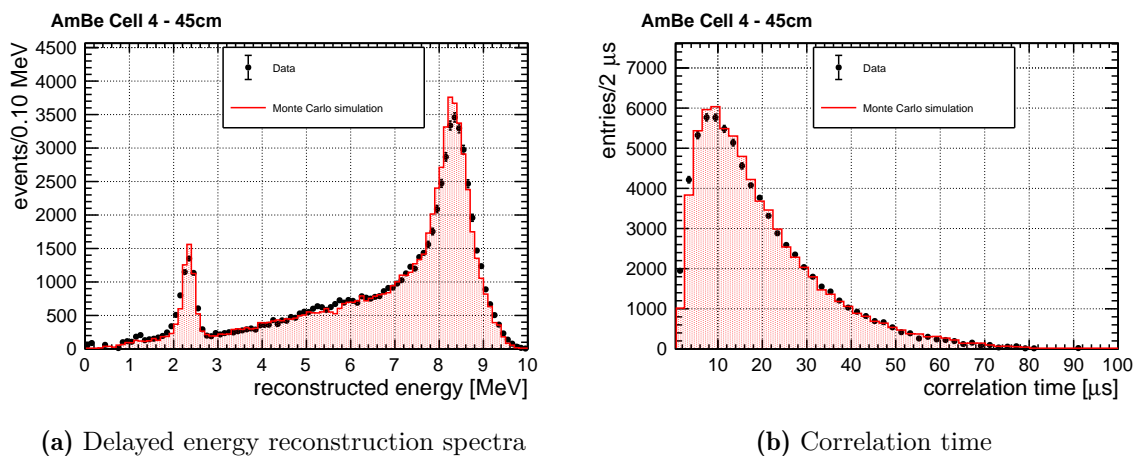**(a)** Delayed energy reconstruction spectra   **(b)** Correlation time

Figure 3.2.6: **(a)** Delayed event energy spectra and **(b)** correlation time in DATA and MC simulations (using FIFRELIN), when the AmBe source is placed at the *center* of `Cell 4` on the `20180619`.

3.3   Detector Monitoring with AmBe Source

The AmBe signals can be used to monitor the stability of the detector response. Along this section, the monthly calibration with the AmBe source have been used to perform a time stability study of the energy reconstruction and the neutron capture time.

3.3.1   Energy Reconstruction Stability

The energy reconstruction performance is tested in the STEREO experiment with a broad set of gamma sources (see Table 2.1.1). In parallel, neutron sources are used to study the high energy gamma released after a neutron capture, including spallation n from cosmic backgrounds and AmBe. On the one hand, these background events homogenously distributed in the entire detector volume allow to review the time stability of the energy reconstruction [72]. On the other hand, the AmBe source can picture the position and shape of both hydrogen and gadolinium peaks at a specific position of the detector. The monthly base calibration of this source allows also to record a time stability. In this section, the hydrogen peak stability is shown. The evaluation of the capture energy is done by a fit of the hydrogen capture peak. In this case, a simple normal distribution is used to model the mono-gamma released in the capture

$$P(E) = \frac{N_o}{\sigma\sqrt{2\pi}} \; e^{-\frac{1}{2}\left(\frac{E-\mu}{\sigma}\right)^2} \; , \tag{3.6}$$

with N_o the normalization component, and μ and σ the mean and the standard deviation respectively. In Fig. 3.3.1a, one calibration date is represented, showing with a red line the fitted function for the hydrogen capture peak using Eq. 3.6. The fit is performed between variable limits depending on the position of the maximum $\mu_{(0)}$, which should be in the capture region between [2, 3] MeV. These variable limits between $[0.9 \cdot \mu_{(0)}, \; 1.1 \cdot \mu_{(0)}]$ help to find the best position of the mean μ due to the sharp form of the peak. In Fig. 3.3.2a, the fit values from the hydrogen capture peak when the source is placed at the *center* are represented along the detector data acquisition time. A value of $\sim 2.330\,\mathrm{MeV}$ is obtained for the reconstructed energy in Phase II, shifted by $\sim 5\%$ with respect to the nominal energy of the hydrogen neutron capture shown in Table 3.1.1. This is caused by the fact that the quenching curve is anchored to the

(a) Hydrogen energy peak fit   (b) Capture time fit
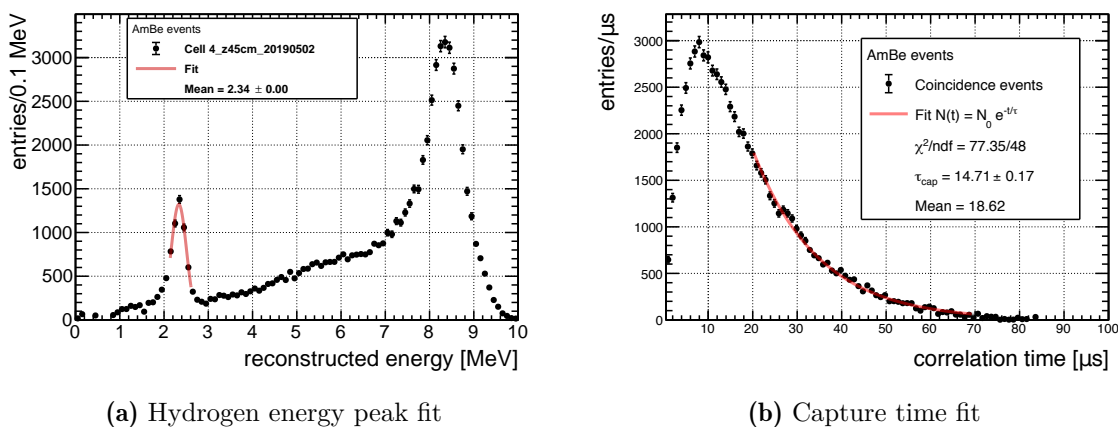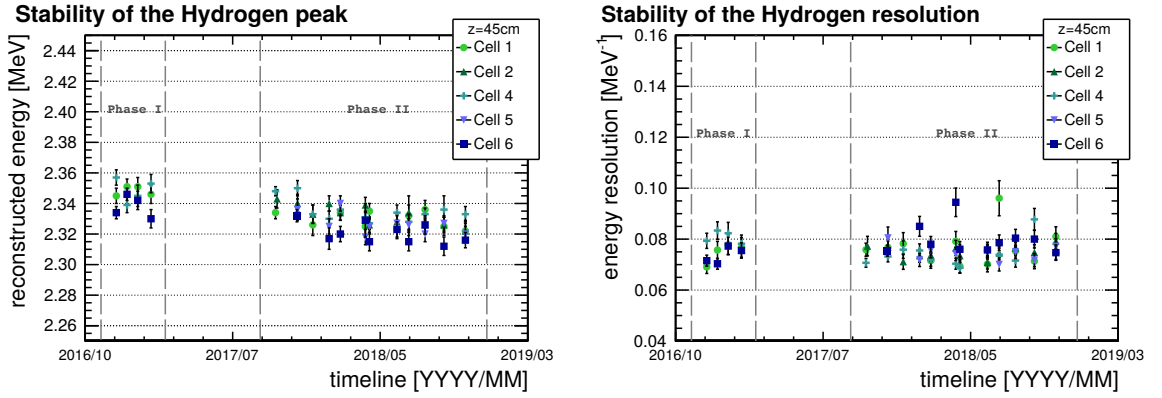
Figure 3.3.1: (a) Hydrogen capture energy peak fit. (b) Capture time fit, obtained when the AmBe source is placed at the *center* of the Cell 4, for the date 20190502. Distributions fitted with the functions in Eq. 3.6 and Eq. 3.7 respectively.

(a) Hydrogen energy peak

(b) Hydrogen energy peak resolution

Figure 3.3.2: Time stability of the **(a)** hydrogen energy peak and **(b)** resolution when the AmBe is placed at the *center* of the cells. Values obtained using Eq. 3.6. Uncertainties are coming from the fit.

[54]Mn point (see Section 2.2.2). This implies that the obtained peaks from the energy scale are typically higher compared to the nominal values. Looking into the time stability, all the NT cells fluctuate within the 0.7% range covered by the energy reconstruction uncertainty (Table 2.2.2). Even though different detector configurations were used between data acquisition phases, energy reconstruction values show compatibility between Phase I and Phase II. This agreement is crucial to combine results of the neutrino spectra from both phases. The resolution of these energy peaks $\left(\frac{\sigma}{\mu}\right)$ is estimated and represented in Fig. 3.3.2b. It confirms the agreement between phases, and points out a light output conservation of the LS during the nearly 3 years of data acquisition.

The hydrogen peak obtained for DATA at different cell heights have been compared to the values
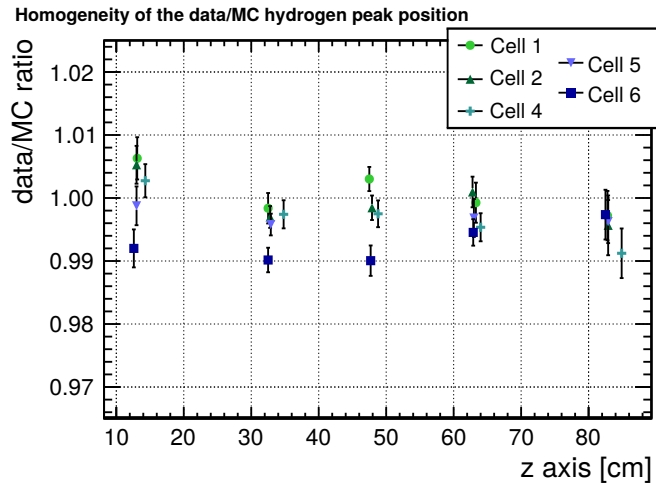

Figure 3.3.3: Homogeneity of the DATA/MC hydrogen peak position for Phase II. DATA values obtained from the time stability average of Fig. 3.3.2a. Uncertainties are obtained by error propagation of the ratio (see Eq. B.7 from the uncertainty appendix), where for DATA the standard deviation from the different calibration dates is considered and for MC the fit error.

from MC simulations. The entire detector energy reconstruction have also been evaluated by this means. In Fig. 3.3.3, these values are represented for all the cells at different heights. Peak positions are compatible between DATA and MC simulations, being all the values in agreement with unity within 1%. *Top/bottom* positions show a good agreement with respect to the *center* area, with a small discrepancy between cells on the *bottom* region. For all the positions, the Cell 6 is below and on the 0.99 ratio region. This cell discrepancy and the non significant *bottom* effect is taken into account on the overall energy reconstruction uncertainty (Table 2.2.2), since neutrino interactions occur homogeneously distributed around the detector volume.

3.3.2 Neutron Capture Time Stability

Neutron capture time is an intrinsic property of the LS, since it depends on its composition and nuclei abundance. It is a value that can differ between experiments, unless they use the same LS sample. This property of the detector is important for the neutrino selection, and it can only be studied with neutron sources that can produce a neutron coincidence. Like for the neutron studies already mentioned, the AmBe source is also studied to characterize this magnitude. This analysis gives understanding of the detector performance, and helps to check for inaccuracies in the implementation of the MC simulation. The correlation time distribution in Fig. 3.2.6b represents the behavior described in Eq. 3.4. The capture time τ_{capt} is the only component studied, and thus the distribution can be simplified to,

$$P(t) = P_o \cdot e^{-t/\tau_{capt}} \; , \tag{3.7}$$

for the correlation time range between [20, 70] µs. In Fig. 3.3.1b, an example of the correlation time distribution fit is represented with a red line. The obtained capture times when the source is deployed at the *center* of the cells are represented in Fig. 3.3.4a. Neutron capture time looks constant in terms of time, with a discrepancy below 3% between the data taking phases. This improvement could be caused by the upgrade of the detector response after repairing all the

(a) Capture time stability

(b) Capture time homogeneity
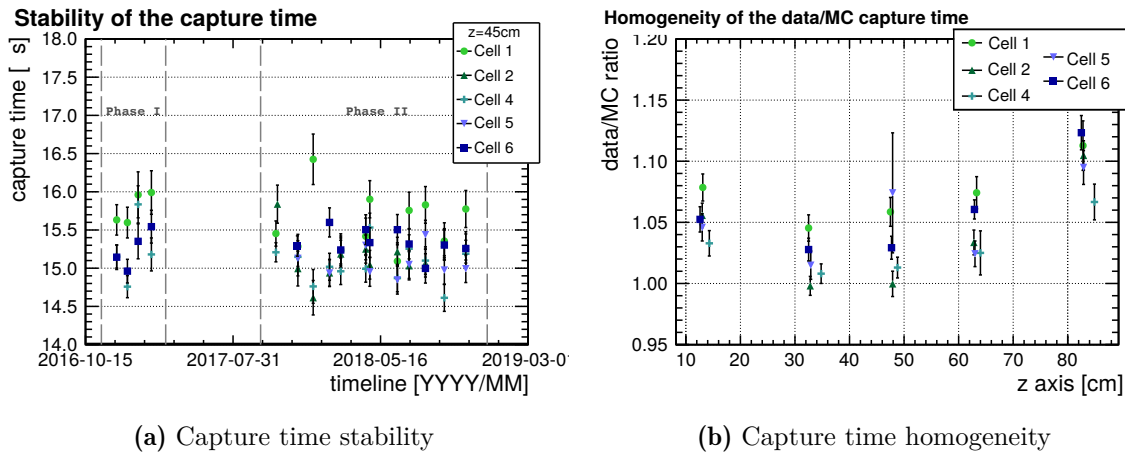
Figure 3.3.4: **(a)** Time stability of the capture time when the AmBe is placed at the *center* of the cells. Values obtained using Eq. 3.7. Uncertainties are coming from the fit. **(b)** Homogeneity of the DATA/MC capture time for Phase II. DATA values obtained from the time stability average of **(a)**. Uncertainties are obtained by error propagation of the ratio (see Eq. B.7 from the uncertainty appendix), where for DATA the standard deviation from the different calibration dates is considered and for MC the fit error.

acrylic walls between data acquisition phases. The obtained values between cells still differ between them, with `Cell 1` always higher than the other ones, and followed by `Cell 6`. This is most certainly caused by a neutron mobility effect. If neutrons are captured on `GC` volumes, they will probably do it on hydrogen nuclei having a higher averaged capture time. Thus, `Cell 4` has a lower n-capture time than the others and it is the one that represents the pure capture time in the `NT`.

The ratios between DATA and MC for different cell heights are illustrated in Fig. 3.3.4b. The physics involving thermal scattering in the MC simulations were fine tuned using solid state models in Geant4 [65]. More details about this improvement can be found in Section 4.2.5. After this improvement, DATA and MC show a complete agreement at the *center* of the cells. However, when the source is placed at the *top/bottom* areas, the $^{\text{DATA}}$/$_{\text{MC}}$ ratio increases. This points towards higher capture times in DATA samples, which means that neutrons in MC simulations are still missing some extra moderation correction. In the *bottom* area, neutrons probably escape from the active volume, most of them being lost in the process due to the shielding layers below the `NT`. The discrepancy in $^{\text{DATA}}$/$_{\text{MC}}$ could be caused by some events in DATA scattering back to the `NT` after escaping and being captured there, physics not being considered in the MC simulation. In the *top* region, a similar process is occurring. Nevertheless, the effect could be more prominent since neutrons are not shielded but moderated in the `Buffer` volume, and most of them come back to the `NT` to be captured. However, the impact of this discrepancy in the $^{\text{DATA}}$/$_{\text{MC}}$ have been studied and it is negligible in the IBD selection. Cut acceptance studies have proven that most of the events, having their vertices in the top region of the detector, are removed in the coincidence selection using the correlation time cut 2 µs in Table 2.2.1 [74].

3.4 Summary and Conclusion

Neutron physics in the STEREO detector need to be understood in order to apply a proper IBD selection. Along this chapter, the main interactions and signals of this type of particles in an organic LS have been described in detail.

The moderation, thermalization and capture processes leave a characteristic trace in the detector that can be seen in terms of the neutron capture energy and capture time. These two main distributions have been studied with the AmBe source, a powerful $\gamma + n$ emitter that can be deployed in the STEREO detector `NT` volume. These two particles, emitted at the same time, are studied with a pair search algorithm in order to have a clean neutron interaction signal. Low energy background events have been statistically subtracted in the code, in addition to correlated background events mimicking the AmBe signal. A good agreement has been reached between DATA and MC simulations, in terms of the neutron capture energy spectra and the correlation time distributions.

The monthly basis calibration of this source is used to monitor the detector response. On one hand, the study of the neutron capture peaks in hydrogen atoms proved a good agreement between data taking phases and between cells. Its comparison with a MC simulation has shown a good agreement on the entire detector volume, with some discrepancies covered with the global energy reconstruction systematic uncertainty. On the other hand, the neutron capture time studies have shown a good stability. Some improvements between `Phase I` and `Phase II` are caused by the upgrade of the detector response after its reparation prior of the `Phase II` data taking period. DATA to MC comparisons have shown some disagreements on the *top/bottom* regions, caused by inaccurate simulated neutron interactions. However, these inconsistencies are under control since cut acceptance studies have proven that most of the event with vertices on the *top/bottom* region are removed.

The selected neutrons from the AmBe are used in the STEREO experiment not only for detector response, but also for the evaluation of the neutron efficiency. In the following chapter, the efficiency treatment of the STEREO detector is described, together with its sensitivity parameters. The last two chapters of this thesis are focused in the study of these values using different MC configurations.

Estimation of the Neutron Selection Efficiency with an AmBe Source

Since the STEREO analysis is based on a DATA to MC comparison, a set of correction coefficients have been introduced to quantify possible discrepancies in the neutron selection efficiency. These correction coefficients are the main topic of this thesis and are studied with neutrons from the AmBe source. In Section 4.1 the importance of these correction coefficients to describe the impact of the Gd selection is presented. All the details about their definition and uncertainty can be found in Section 4.2, together with the information about how these parameters are introduced in the STEREO analysis. All of the information described along this chapter is going to be used for the efficiency estimations in Chapter 5 and 6.

4.1 Neutrino Selection Efficiency

Neutrinos are tagged in the detector through the IBD coincidence selection that depends on the correlation of both the prompt and delayed selection cuts. The neutrino selection efficiency ϵ_{sel} in the detector volume can be defined as the ratio

$$\epsilon_{sel} = \frac{\text{N(selected IBD events in detector)}}{\text{N(neutrinos that interact in detector)}} \ . \tag{4.1}$$

For the evaluation of this efficiency term, all of the IBD selection cuts need to be taken into account. A summary of the main selection cuts presented in Chapter 2 and their acceptances a_{cut} are gathered in Table 4.1.1. The acceptance coefficients a_{cut} represent the impact of removing a specific *cut* in the selection, and for a cut x is defined as [74],

$$a_x = \frac{\text{N(selected IBD events with all cuts)}}{\text{N(selected IBD events without cut x)}} \ . \tag{4.2}$$

These values are computed with a neutrino MC simulation. As it can be seen, the delayed selection cuts are the ones causing a higher impact on the neutrino selection, specially the delayed energy cut for the Gd-selection with an acceptance $a_{\text{E}_{delayed}} = 75.9\%$. Combining all the selection cuts, an overall selection efficiency ϵ_{sel} of 61% is obtained in the NT [4]. Central cells present a similar averaged value (63%), while in `Cell 1` and `Cell 6` a few per-cent lower selection efficiency is observed due to the loss of neutron detection efficiency at the edge of the detector. Besides, `Cell 6` has some extra neutron loss due to the directionality of the incident neutrinos. It could be expected that the neutrino selection efficiency ϵ_{sel} from the MC simulation would be the same that what it is observed in DATA. However, some inaccuracies in the MC

Table 4.1.1: Summary of the main IBD selection cuts presented in Table 2.2.1. For each selection cut, the respective acceptance a_{cut} is computed with Eq. 4.2 using a MC simulation [74, 4]

Type	Cut	a_{cut} [%]
Energy	$1.625\,\text{MeV} < \text{E}^{\texttt{DET}}_{prompt} < 7.125\,\text{MeV}$	89.3
	$4.5\,\text{MeV} < \text{E}^{\texttt{DET}}_{delayed} < 10\,\text{MeV}$	75.9
Coincidence	$2\,\text{µs} < \Delta\text{T} < 70\,\text{µs}$	95.2
	$\Delta\text{X} < 600\,\text{mm}$	99.3
Topology	$\text{E}^{\texttt{Cell}}_{prompt} < 1\,\text{MeV}$, neighbour cell	98.6
	$\text{E}^{\texttt{Cell}}_{prompt} < 0.4\,\text{MeV}$, other cell	97.8
	$\text{E}^{\texttt{NT}}_{delayed} > 1\,\text{MeV}$	97.8

simulations concerning the particle interactions make the equivalence $\epsilon^{\texttt{DATA}}_{sel} = \epsilon^{\texttt{MC}}_{sel}$ not possible. Instead, such relation needs to be constructed as,

$$\epsilon^{\texttt{DATA}}_{sel} = \epsilon^{\texttt{MC}}_{sel} \cdot c_\varepsilon \cdot N_{proton} \ . \tag{4.3}$$

On one hand, the N_{proton} factor is needed to correct the number of protons in the MC simulation, a crucial parameter for the evaluation of the total amount of IBD events. The computation of this value can be found in [61, 65]. On the other hand, c_ε corresponds to the correction coefficient of the neutron selection efficiency. Some innacuracies concerning the neutron physics in the MC simulation create discrepancies with the observed events in DATA. The evaluation and interpretation of the correction coefficient c_ε for the neutron efficiency is the main topic of this thesis, and a closer look into its definition is described in the following section.

4.2 Correction Coefficients for the Neutron Efficiency

The correction coefficient c_ε evaluates the selection of the IBD delayed event, and it is formed by two different terms,

$$c_\varepsilon = c_{\text{Gd}} \times c_{\text{IBD}} \ . \tag{4.4}$$

Each of these terms accounts for a different contribution:

- the efficiency term c_{Gd} considers the fact that only captures on Gd nuclei are used to select neutrinos, compared to other possible captures (e.g. in hydrogen atoms). It is called Gd-fraction because it studies the relative abundance of neutron captures on the Gd-nuclei in the NT;

- the efficiency term c_{IBD} takes into account the impact of the neutron IBD selection cuts (energy and time) with respect to the global amount of Gd events in the detector.

These correction coefficients for the neutron efficiency, c_{Gd} and c_{IBD}, are evaluated by means of the neutron emission of the AmBe source (described in Chapter 3). Each of them is computed through a DATA to MC efficiency ratio,

$$c_x = \frac{\varepsilon^{\texttt{DATA}}_x}{\varepsilon^{\texttt{MC}}_x} \ . \tag{4.5}$$

The efficiency term ε_x is defined as the fraction of events,

$$\varepsilon_x = \frac{n_x}{m} \ . \tag{4.6}$$

where m represents events in a wide range, and n_x the number of events in m passing the cut x. Each of the terms composing the c_ε studies a different cut fraction x. Therefore the total correction coefficient c_ε is computed as,

$$c_\varepsilon = \left(\frac{c_{\mathrm{Gd}}^{\mathsf{DATA}}}{c_{\mathrm{Gd}}^{\mathsf{MC}}} \right) \times \left(\frac{c_{\mathrm{IBD}}^{\mathsf{DATA}}}{c_{\mathrm{IBD}}^{\mathsf{MC}}} \right) \ . \tag{4.7}$$

The following subsections describe how these two terms and their statistical uncertainties are obtained, together with their impact in the STEREO analysis and their MC systematics. The final c_{Gd} and c_{IBD} values used in the STEREO analysis are described in the Chapter 5 and 6.

4.2.1 Neutron Capture Fraction or Gd-fraction

As it has been highlighted in Chapter 3, the neutron capture is a competitive process between the different isotopes in the LS, according to their respective capture cross-section. The abundance of these isotopes in the medium determines the outcome of the process. In the NT, this competition is mainly taking place between the Gd and the H nuclei. The neutrons captured by Gd are expected to release gammas with the total sum energies around 8 MeV, and the H captures are at 2.2 MeV. More information about it can be found in Section 3.1.3. As it was already shown in Fig. 3.2.6a, Gd-capture events are mainly distributed with visible energies between 3 MeV and 10 MeV (Gd-capture peak and its tail), while H-captures are distributed with visible energies in the range [1.5, 3] MeV. Fig. 4.2.1 plots a more representative pictures of the range of events on the neutron capture energy spectra.
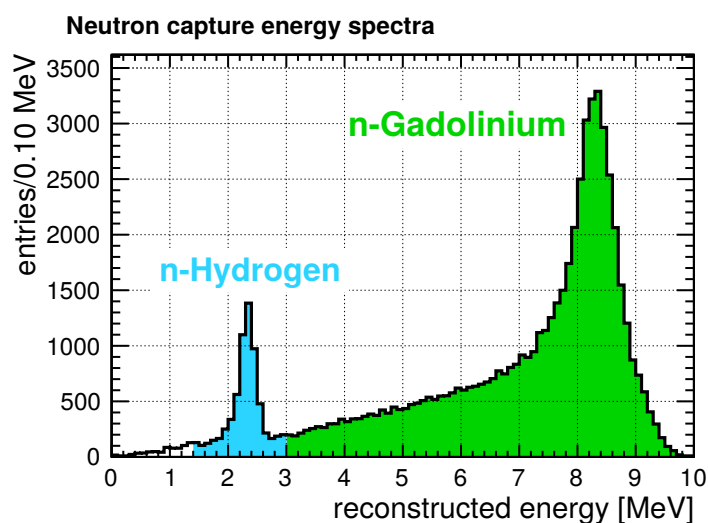

Figure 4.2.1: Neutron capture spectra from the coincidence search on AmBe DATA. The green (blue) area is representing the energy range of the Gd- (H-) captures (full energy peak + tail) used for the computation of the $\varepsilon_{\mathrm{Gd}}$.

Considering these energy ranges, and the efficiency definition in Eq. 4.6, the Gd-fraction is defined as the amount of Gd captures (N_{Gd}) compared to the ones in other nuclei as H (N_H)

$$\varepsilon_{Gd} = \frac{N_{Gd}}{N_{Gd} + N_H} = \frac{N(3\,\text{MeV} < E^{DET} < 10\,\text{MeV})}{N(1.5\,\text{MeV} < E^{DET} < 10\,\text{MeV})} \; , \tag{4.8}$$

where E^{DET} is the reconstructed energy in the detector volume.

4.2.2 IBD Selection Cut Efficiency

The observation of a neutron event tags the neutrino interaction by the coincidence signal of an IBD. These neutrons are selected using the energy and time cuts presented in Table 2.2.1:

$$
\begin{aligned}
4.5\,\text{MeV} &< E^{DET} < 10\,\text{MeV} \; , \\
E^{NT} &> 1\,\text{MeV} \; , \\
2\,\mu s &< \Delta t < 70\,\mu s \; .
\end{aligned}
\tag{4.9}
$$

The IBD cut efficiency evaluates the effect of these cuts on the events classified as Gd captures. Using the neutron events from the AmBe source, Fig. 4.2.2 represents how the time and energy cut would select them. Considering the efficiency definition in Eq. (4.6) and the previously mentioned cuts, the simplest way to define this term is:

$$\varepsilon_{IBD} = \frac{N(4.5\,\text{MeV} < E^{DET} < 10\,\text{MeV} \; \cap \; E^{NT} > 1\,\text{MeV} \; \cap \; 2\,\mu s < \Delta t < 70\,\mu s)}{N(3\,\text{MeV} < E^{DET} < 10\,\text{MeV})} \; , \tag{4.10}$$

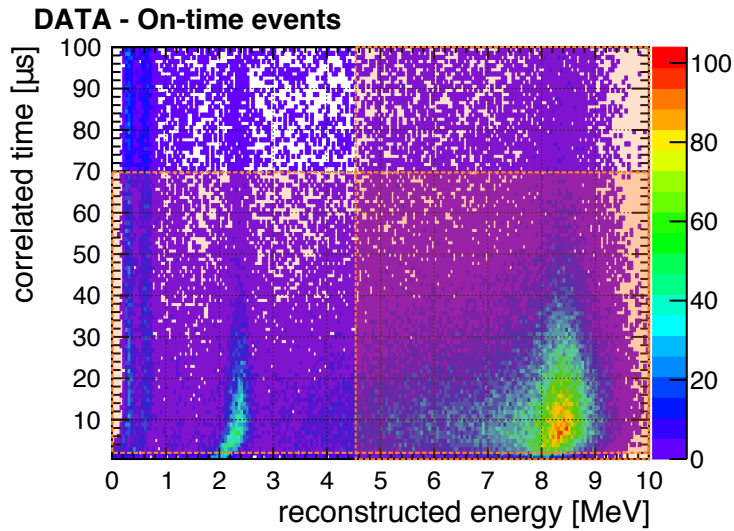with the denominator being the number of Gd captures defined in Fig. 4.2.1.

Figure 4.2.2: Representation of the reconstructed energy versus correlation time for the on-time AmBe events. With orange bands the used IBD selection cuts are represented. Off-time events can not be subtracted in an event basis.

The $\varepsilon_{\mathsf{IBD}}$ term accounts for all correlations between different cuts, allowing a global efficiency term to be written as:

$$\varepsilon = \varepsilon_{\mathrm{Gd}} \times \varepsilon_{\mathsf{IBD}} = \frac{\mathrm{N}(4.5\,\mathrm{MeV} < \mathrm{E}^{\mathrm{DET}} < 10\,\mathrm{MeV} \;\cap\; \mathrm{E}^{\mathrm{NT}} > 1\,\mathrm{MeV} \;\cap\; 2\,\mu\mathrm{s} < \Delta t < 70\,\mu\mathrm{s})}{\mathrm{N}(1.5\,\mathrm{MeV} < \mathrm{E}^{\mathrm{DET}} < 10\,\mathrm{MeV})} \;. \quad (4.11)$$

In this way, the total efficiency term ε includes the selection cuts for the Gd capture events, with respect to all the neutron captures in the `NT` volume.

4.2.3 Statistical Uncertainties

The efficiency terms ε_x (with $x \in \{\mathrm{Gd}, \mathsf{IBD}\}$) are defined as the ratio of events in Eq. 4.6. The statistical uncertainty of this ratio depends on the correlation between numerator and denominator, since the total amount of events m contains both the events that satisfy the cut x (n_x) and the ones that do not (r) fulfilling that $m = n_x + r$. The statistics involving a series of events individually passing the selection cuts can be interpreted by a binomial distribution [76], where for a set of m experiments the probability ε_x, the probability p of a subset n_x randomly passing the cut x is distributed as

$$\mathrm{p}(n_x | \varepsilon_x, m) = \binom{m}{n_x} \varepsilon_x^{n_x} (1 - \varepsilon_x)^{m - n_x}. \quad (4.12)$$

The mean number of successful experiments can be approximated to the mean of a normal distribution $< n_x > = m \cdot \varepsilon_x$. Given that each single experiment can be interpreted as a Bernoulli distribution [77], the variance of the binomial can be proven to be $\mathrm{Var}(n_x) = m\varepsilon_x(1 - \varepsilon_x) = \sigma_{n_x}^2$. From here it is possible to compute the uncertainty of ε_x as

$$\delta\varepsilon_x = \frac{\delta < n_x >}{m} = \frac{\sigma_{n_x}}{m} = \frac{\sqrt{m\varepsilon_x(1 - \varepsilon_x)}}{m} = \sqrt{\frac{\varepsilon_x(1 - \varepsilon_x)}{m}} \;. \quad (4.13)$$

In conclusion, any selection efficiency is written in the form $\varepsilon_x \pm \delta\varepsilon_x$ using Eq. 4.6 and Eq. 4.13.

4.2.4 Correction Coefficients and the STEREO Analysis

The correction coefficients for the neutron efficiency play an important role in the STEREO analysis. On one hand, they are used in the comparison between the measured neutrino candidates and their expectation for an oscillation analysis. On the other hand, the correction coefficients participate in the rate analysis of the absolute neutrino flux. In the following paragraphs the treatment of the c_ε is described in the STEREO analysis:

Oscillation analysis: The c_ε correction coefficients take part in the evaluation of χ^2 already defined in Eq. 2.17,

$$\chi^2 = \sum_{l=1}^{N_{\mathrm{Cells}}} \sum_{i=1}^{N_{\mathrm{E\text{-}Bins}}} \left(\frac{D_{l,i} - \phi_i M_{l,i}}{\sigma_{l,i}} \right)$$
$$+ \sum_{l=1}^{N_{\mathrm{Cells}}} \left(\frac{\alpha_l^{\mathrm{E\text{-}Scale\;unc.}}}{\sigma_l^{\mathrm{E\text{-}Scale\;unc.}}} \right) + \left(\frac{\alpha^{\mathrm{E\text{-}Scale\;c.}}}{\sigma^{\mathrm{E\text{-}Scale\;c.}}} \right) + \sum_{l=1}^{N_{\mathrm{Cells}}} \left(\frac{\alpha_l^{\mathrm{Norm\;unc.}}}{\sigma_l^{\mathrm{Norm\;unc.}}} \right) \;. \quad (4.14)$$

More concretely, they are introduced in the nuisance parameters $\vec{\alpha}$, that account for energy scale, cell volume and neutron efficiency corrections. Assuming only contribution from the neutron

efficiency, a nuisance parameter α_l needs to be evaluated or each cell l. The oscillation fit varies the correction coefficient within its uncertainty like,

$$c_\varepsilon \to \tilde{c}_\epsilon = c_\varepsilon + \delta_{\tilde{c}_\varepsilon} \;, \qquad (4.15)$$

where the variation $\delta_{\tilde{c}_\varepsilon}$ is related to the uncertainty of c_ε, $\delta(c_\varepsilon)$. Within these variations, the nuisance parameter α_l is tested in the $\Delta\chi^2$ as

$$\alpha_l = c_\varepsilon - \tilde{c}_\varepsilon \;. \qquad (4.16)$$

The evaluation of α_l is iterated by changing $\tilde{c}_\varepsilon$ according to Eq. 4.15, until the minimization of $\Delta\chi^2$ is achieved. It needs to be remarked that the nuisance parameters take part in the calculation of the expected number of neutrinos $M_{l,i}$, both in the uncertainty terms $\sigma_{l,i}$ and in the pull terms $(\alpha/\sigma)^2$ in the Eq. 2.17. Therefore, an independent $c_{\varepsilon,l}$ correction coefficient is computed for each cell l. The correct evaluation of these values in the NT is crucial for the oscillation analysis in the Stereo experiment.

Normalization of the absolute neutrino flux: The neutrino selection efficiency needs to be introduced in the evaluation of the detected neutrino flux,

$$\phi_\nu^{det} = \phi_\nu^{em} \cdot \tau_{int} \cdot \epsilon_{sel} \;. \qquad (4.17)$$

This selection efficiency term uses the correction coefficients presented in Eq. 4.3. For the detected neutrino flux, an independent correction coefficient $c_{\epsilon,l}$ for each cell l is computed in the same fashion as the ones for the oscillation analysis. This correction coefficients have been used to compute the rate of neutrinos per cell in Fig. 2.2.9. However, for the absolute normalization of the neutrino flux in Eq. 2.16, a global coefficient $\langle c_\varepsilon \rangle$ for the entire NT volume is evaluated.

4.2.5 Systematic Studies

The c_{Gd} and c_{IBD} correction coefficients need to be able to reproduce the detector effects, with a minimal impact of the selection cuts and MC simulation inaccuracies. Three external factors that could affect the systematic of the DATA to MC efficiency ratios are studied along this section.

Source Position and Neutron Capture

Due to the thermalization process neutrons can travel some distance through the LS before they are capture. In the case of a $\sim 5\,\text{MeV}$ AmBe neutron, a mean free path of approximately $4\,\text{cm}$ [65] is expected. Considering the size of the cell ($L \times l \simeq 36\,\text{cm} \times 90\,\text{cm}$) and the position of the calibration tube (Fig. 3.2.2), the effect of this mean free path is negligible for center cells while it creates an impact on the border ones. The *top* and *bottom* positions are sensitive to the escape of γs, and the intensity of such effect depends on the position of the neutron source. During the first calibration dates, a mismatch between the deployment position in DATA and the MC was observed. A position shift around $\sim 2\,\text{cm}$ can create a discrepancy in the c_ε of $\sim 0.8\%$ in the border regions of the detector (*top*, and *bottom* positions of Cell 1 and Cell 6). The impact of this source position has been treated as part of the systematic uncertainties of the c_ε coefficients. More details about this analysis would be presented in Section 5.4.

Optimization of Neutron Selection Cuts

The c_{IBD} ratio depends on the energy and time cuts used in the coincidence selection (see Section 2.2.4). Even if these cuts are chosen to maximize the neutrino acceptance [74], a discrepancy in the capture time or energy spectra between DATA and MC can cause an additional tension in c_{IBD}. This dependency has been studied performing a scan of the lower energy cut of $E^{\text{DET}} > 4.5\,\text{MeV}$, and the upper time cut of $\Delta T < 70\,\mu\text{s}$.

The lower energy limit has been varied in an energy range of $4\,\text{MeV}$ to $6\,\text{MeV}$, in steps of $0.5\,\text{MeV}$, for fixed time and an upper energy cut like

$$\varepsilon_{\text{IBD}}(X) = \frac{N(X < E^{\text{DET}} < 10\,\text{MeV} \ \cap \ E^{\text{NT}} > 1\,\text{MeV} \ \cap \ 2\,\mu\text{s} < \Delta T < 70\,\mu\text{s})}{N(3\,\text{MeV} < E^{\text{DET}} < 10\,\text{MeV})} \tag{4.18}$$
$$\text{with X} = \{4,\ 4.5,\ 5,\ 5.5,\ 6\}\,\text{MeV} \ .$$

In this way, the energy region covering the Gd peak can be inspected. The c_{IBD} values resulting for a different X_i have been tested and compared to the reference value c_{IBD} used in Eq. 4.10 leading to the discrepancy ratio

$$r_{X_i} = \frac{c_{\text{IBD}}(X_i)}{c_{\text{IBD}}} \ . \tag{4.19}$$

In Fig. 4.2.3a, the obtained values of r_{X_i} are represented. It can be seen that for small energy cut variations of $0.5\,\text{MeV}$, the ratio r_{X_i} keeps constant and stable within $\sim 1\%$ around the used cut $E^{\text{DET}} > 4.5\,\text{MeV}$. A strong impact is obtained when the energy cuts get closer to the Gd peak region, $E^{\text{DET}} \gtrsim 5\,\text{MeV}$. This is caused by an energy bias between DATA and MC simulations. These results show a robust low energy cut of $4.5\,\text{MeV}$, with a low variability covered by the statistical uncertainty of the energy reconstruction (Table 2.2.2).
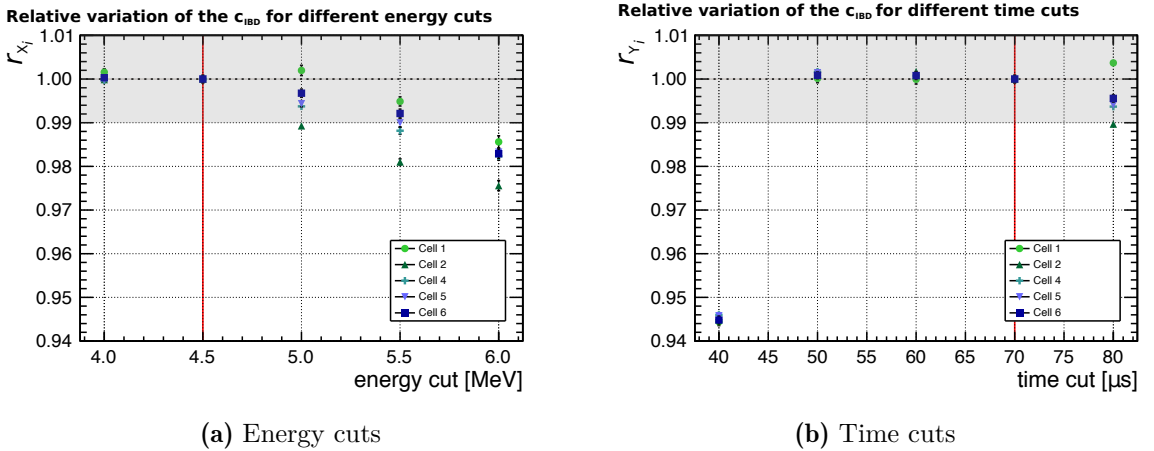

(a) Energy cuts   **(b)** Time cuts

Figure 4.2.3: Relative variations of the c_{IBD} with respect to the **(a)** energy and **(b)** time cut when the AmBe source at the center of the NT cells.

A similar study have been applied for the upper time limit. In this case, the time cut has been varied between $40\,\mu s$ and $80\,\mu s$, in $10\,\mu s$ steps for fixed energy cuts

$$\varepsilon_{\mathsf{IBD}}(Y) = \frac{N(4.5\,\mathrm{MeV} < E^{\mathrm{DET}} < 10\,\mathrm{MeV}\ \cap\ E^{\mathrm{NT}} > 1\,\mathrm{MeV}\ \cap\ 2\,\mu s < \Delta T < Y)}{N(3\,\mathrm{MeV} < E^{\mathrm{DET}} < 10\,\mathrm{MeV})} \tag{4.20}$$
$$\text{with } Y = \{40,\ 50,\ 60,\ 70,\ 80\}\,\mu s\ .$$

Similarly to the analysis of the previous cut, the discrepancy ratios r_{Y_i} can be obtained as

$$r_{Y_i} = \frac{c_{\mathsf{IBD}}(Y_i)}{c_{\mathsf{IBD}}}\ . \tag{4.21}$$

with respect to the reference value c_{IBD} used in Eq. 4.10. The obtained values are represented in Fig. 4.2.3b. A stable situation can be found in the time range between $50\,\mu s$ to $70\,\mu s$, with variations within $\sim 0.1\%$, while the values near the limit cut drift away from the stability. In the first case ($40\,\mu s$), the ratio is sensitive to neutron thermalization discrepancies in the MC spectra (see Fig. 3.2.6b), and produces a decrease of $\sim 4.5\%$. In the second case ($80\,\mu s$), the tail of the correlation time spectra is sensitive to the background subtraction leading to a 1% decrease. Small fluctuations around the used energy and time cuts lead to stable behavior of the correction coefficients, ensuring a good understanding of the event selection in DATA and MC.

Neutron Physics in the MC Simulations

In the MC framework, all the physical processes are simulated and taken into account to compare it with DATA. Nevertheless, the efficiency ratios c_ε are sensitive to the specific implementation of the neutron physics [68, 69]. It is important to know the impact of possible inaccuracies, to be able to disentangle them from other physics effects in DATA. Several physics parameters in the MC simulations, and their impact in the c_ε coefficients, have been studied.

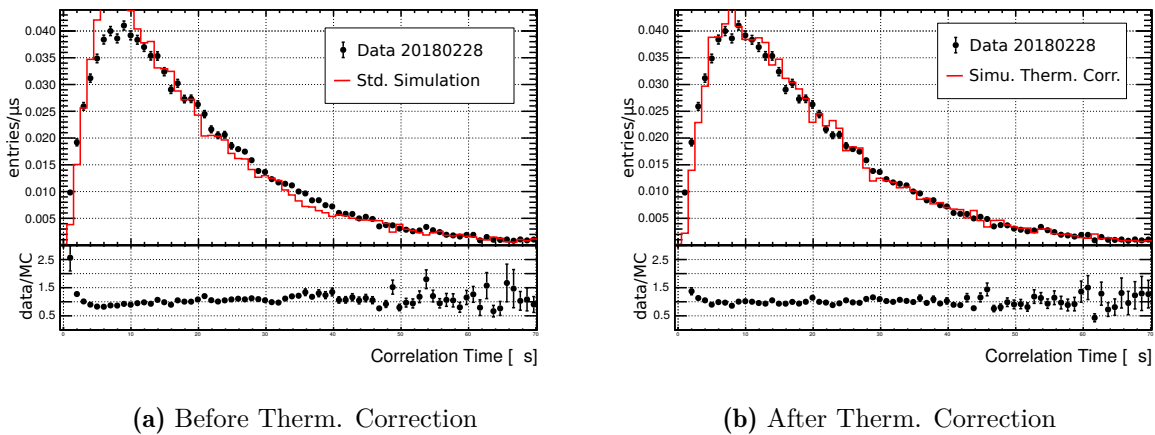(a) Before Therm. Correction   (b) After Therm. Correction

Figure 4.2.4: Correlation time distributions for DATA and MC in `Cell 4 - 45 cm` using the **(a)** standard MC simulation and **(b)** corrected MC simulation including the thermal scattering libraries.

Some tension was observed between the neutron capture time in DATA and MC, prior to the already updated results in Section 3.2.4. An upgrade in the MC implementation of the thermal scattering with neutrons in `Geant4` [65], caused a 1% improvement of the MC capture time leading to a better agreement with DATA. In Fig. 4.2.4b and Fig. 4.2.4b the old and updated time distributions are represented. With this improvement of the thermalization, a better agreement in the c_{Gd} has been observed, with a relative 1% increase [66] of the value. With the updated MC, no impact on the systematic uncertainties is expected.

Another way to significantly affect the neutron physics in the MC simulation is by tuning the concentration of Gd. Such tunning compensates other non-well simulated effects, as the neutron diffusion. Since some tension was observed in the c_{Gd} correction coefficient, a 0.75 reduction of the Gd concentration (current value of $1.8\,\mathrm{mg\,cm}^{-3}$, 0.2%w.t.) has been tested. This tuning has affected the c_{Gd} with a global improvement of a $\sim 1\%$ in all the detector positions, together with a 1% asymmetry when *top/bottom* regions of the detector are compared [67]. At the same time, this variation has increased the neutron capture time by $1\,\mathrm{\mu s}$, creating a disagreement between DATA and MC. This Gd concentration tuning has also shown that an optimal agreement can not be achieved to all of the parameters at the same time. Therefore, the measured value in the laboratory is the one implemented in the simulation.

The major improvement in the MC simulation regarding the neutron physics redefines the γ cascade released upon a Gd capture. As it has been mentioned in Chapter 3, the STEREO simulation framework used initially the `GLG4sim` libraries to account for this. After the implementation of the FIFRELIN model, the reconstructed energy spectra of neutron captures has improved notably. In the following chapters (Chapter 5 and 6) more details about these results will be presented, together with the obtained c_{Gd} and c_{IBD} coefficients for both models.

4.3 Summary and Conclusions

This chapter has introduced all the relevant parameters for the study of the total correction coefficient of the neutron efficiency c_ε. These parameters are needed to described the neutrino selection efficiency and they are consistently used in the STEREO oscillation analysis.

Two different terms have been introduced to conform the total c_ε correction coefficient. On one side, the Gd-fraction c_{Gd} evaluates the ratio of Gd captures with respect to the other possible capture channels in the detector. This efficiency term is based on a cut on the energy spectra of the neutron captures. On the other side, the IBD selection cut efficiency describes the impact of the selection cuts of the Gd channel with respect to all the Gd captures in the detector volume. The possible systematic sources of these efficiency ratios have also been described in this chapter. Some discrepancies in the neutron source position or the energy reconstruction can create a bias between DATA and MC and are considered as part of the systematic uncertainty in future chapters. Inaccuracies in the MC simulation have been taken into account, and tuned in order to reach the best agreement with DATA. These corrections include the thermal neutron scattering, or the Gd concentration of the LS. One major improvement of the MC simulation regarding the neutron physics is the improvement of the γ cascade used in the `GLG4sim` package with the introduction of the FIFRELIN model. The performance of these two models is described in the following chapters, together with results concerning the correction coefficients for the neutron efficiency.

"Come to us, Lazarus, it's time for
you to go."

— Porcupine Tree, *Lazarus*

Correction Coefficients for the Neutron Efficiency using `GLG4sim` MC

The understanding and interpretation of the correction coefficients for the neutron efficiency values plays an important role in the Stereo analysis. As it has been introduced in Section 4.1, these parameters are studied in terms of the DATA to MC efficiency ratios, and are affected by the MC modelization of the gamma cascade after a neutron capture in Gd [51]. This chapter presents the obtained neutron detection efficiencies using the `GLG4sim` package in the Stereo MC framework. In Section 5.1 it is described how this package is implemented in the MC simulation, and its impact on the energy spectra of the neutron capture is shown. Then, in two different parts (Section 5.2 and 5.3) the obtained results for Phase I and Phase II of the data taking are displayed. The time stability and homogeneity of these parameters are also exposed in these sections. A systematic uncertainty study has been done, mostly for the Phase II results and it is developed in Section 5.4. A summary of the correction coefficients used in the Stereo analysis is described in Section 5.5. Finally, the evaluation of the correction coefficients for the absolute normalization of the neutrino flux is shown in Section 5.6.

5.1 Simulated Gamma Cascade from Gd De-excitation using `GLG4sim`

It has been already mentioned in Section 2.2.3 that the Stereo simulation framework is based on Geant4. They are used to build the detector geometry and to describe its response, including the light emission by the LS and its collection. However, the Geant4 Data Libraries (G4NDL) do not model accurately the gamma cascade emission after a neutron capture in Gd. Discrete energy gamma lines typically describe $1-2\%$ of all the neutron captures on Gd and they are not included in these libraries. Their proper modeling is crucial for compact LS based experiments, since the escape of those gammas from the active volume causes structure in the spectrum below the full energy peak deposition.

As a workaround, the empirical gamma cascade designed in the `GLG4sim` package [75] was initially used in the Stereo experiment. This package is inherited from other experiments like Double Chooz [23] and Nucifer [24], and provides a personalisation of the `G4NeutronHP` libraries with a dedicated code to account for Gd gamma final states. `GLG4sim` serves from the G4NDL for the neutron capture cross section (`G4NeutronHPCapture`). As it was highlighted in previous chapters, two main features of the gamma cascade need to be understood and properly modeled: the energy of the emitted gammas and the multiplicity of their emission. The gamma energy spectra used in the `GLG4sim` package is represented in Fig. 5.1.1a. One of the major improvements during the creation of the `GLG4sim` package was the addition of high energy gammas in

Table 5.1.1: Multiplicity of the gamma emission when a neutron capture occurs in one of the gadolinium isotopes using the GLG4sim package [51].

GLG4sim	
Gd isotope	γ **multiciplity**
155	4.271 ± 0.001
157	3.968 ± 0.001

the [5, 8] MeV region that were not present in the initial G4NDL [75]. Concerning the gamma emission multiplicity, in Fig. 5.1.1b the distribution for each Gd isotope is represented. The averaged amount of gammas emitted per isotope is around ~ 4, as it is summarized in Table 5.1.1.

In compact detectors like STEREO, the quality of the gamma cascade model is important when comparing DATA to MC simulations. Since the neutrino interaction is observed with a coincidence selection, an energy cut is applied on the IBD neutron events as explained in Chapter 4. This cut considers the full energy deposition peak of the Gd capture and a part of its tail, two parts sensitive to the gamma cascade model in the reconstructed energy spectra. Besides, the amount of gammas that can escape the active volume and the energy they are carrying when leaving the fiducial volume need to be properly simulated. In the next subsection, the main discrepancies between AmBe neutron capture energy spectra for DATA and MC using the GLG4sim package are presented. Finally, the estimated values for the neutron detection efficiency when the DATA results are compared to MC are shown.

5.1.1 Reconstructed Energy Distribution after a Neutron Capture

In Fig. 5.1.2, the energy spectra obtained after a neutron capture when the AmBe source is placed at different heights in the Cell 1 and Cell 4 are represented. These two cells have been chosen to compare the two different scenarios in the detector: the effect of the source at the center of the detector (Cell 4), and the effect caused by the neutron traveling out of NT limits (Cell 1).
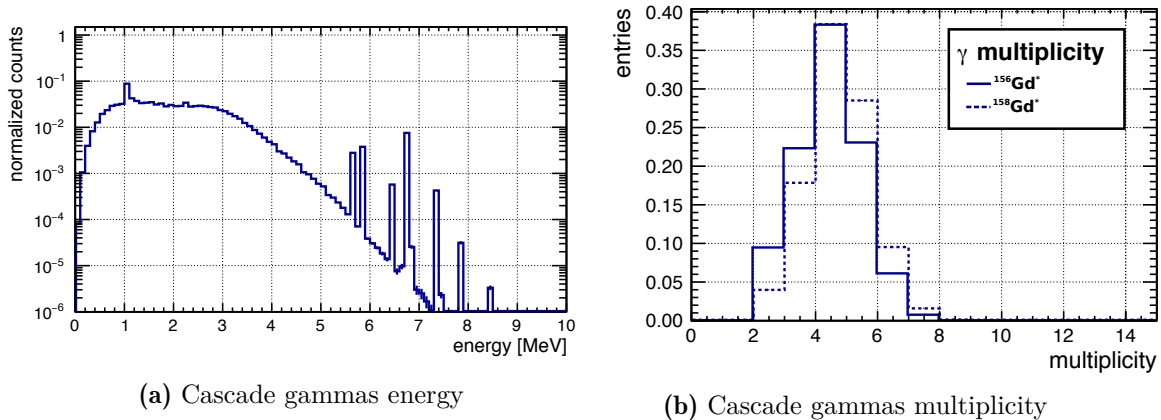

(a) Cascade gammas energy

(b) Cascade gammas multiplicity

Figure 5.1.1: **(a)** Energy distribution of the gamma cascade and **(b)** gammas multiplicity using GLG4sim package [51].

As it can be seen in Fig. 5.1.2c and Fig. 5.1.2d when the source is placed at the *center* of the cells, the hydrogen and gadolinium capture energy peaks are well defined. These two peaks are connected by a continuum coming from the Gd neutron capture, related to the emission distribution of Fig. 5.1.1a. This area presents some discrepancies between DATA (black dots) and MC (blue line) distributions, with stronger tension on the [3, 5] MeV region. This discrepancy is also observed in the energy region below the hydrogen capture peak, where the MC simulations values are also lower than the DATA ones.

It is also important to compare the respective position of the Gd peak. The MC peak is pulling into higher energies than the one in DATA. This is directly linked to the gamma cascade simulation, since it depends on the energy and the multiplicity of the gammas. Even though artifacts on the energy reconstruction could also cause a discrepancy between these two peaks, a wrong modelization of the Gd capture gamma emission would bias the energy capture peak in all the positions simultaneously.

By observing the AmBe distributions in the border regions, another feature can be observed. There is a size discrepancy between the H capture peak and the gadolinium one, pointing to larger amount of neutron captures in hydrogen nuclei in DATA than in MC simulations[1]. This discrepancy could be caused by a wrong modelization of the neutron interactions in the detector, linked to the neutron capture cross section, that does not reproduce accurately the neutron escape from the NT.
When a neutron source is placed at the *top* and *bottom* regions, the energy spectra are mostly affected by the neutron mobility and the gamma escapes from the NT. These escapes cause a less prominent Gd capture energy peak, due to the lower energy deposition in the volume. DATA to MC differences can clearly be observed in Fig. 5.1.2a or Fig. 5.1.2b, where the AmBe source is placed at the *top* position of the cells. On one hand, the `Cell 1` distribution shows a reduced amount of hydrogen capture events in the MC due to not enough simulated neutrons moving to the GC volume and being captured on these nuclei. On the other hand, the Gd neutron capture energy peak is attenuated and less defined than at the *center* position of the cells. The continuum shows a disagreement between the DATA and MC simulations, showing again a stronger tension in the energy area closer to the H capture peak. In Fig. 5.1.2e and Fig. 5.1.2f, the shape of the energy spectra when the source is placed at the *bottom* of the cells it is shown. Better defined Gd capture peaks than in the *top* region are observed, but with some attenuation compared to the *center* of the cell. The reason behing this is that gammas have less probability to escape the reflective walls placed at the bottom of the cell than to escape from the top region to the buffer volume.

Overall, several features have been observed in the MC simulations concerning the neutron capture hydrogen and gadolinium peak positions, the tail connecting them, and the amount of captures. The impact of these discrepancies between DATA and MC simulation using `GLG4sim` is the topic of this chapter, and it is studied with the computation of the correction coefficient. In the next sections, it is shown how these numbers have been interpreted and modeled in the STEREO detector during the data taking of Phase I and Phase II.

---

[1]the internal calibration tube in `Cell 1` is placed at only $13\,\mathrm{cm}$ from the `GCFront` (see Fig. 3.2.2).
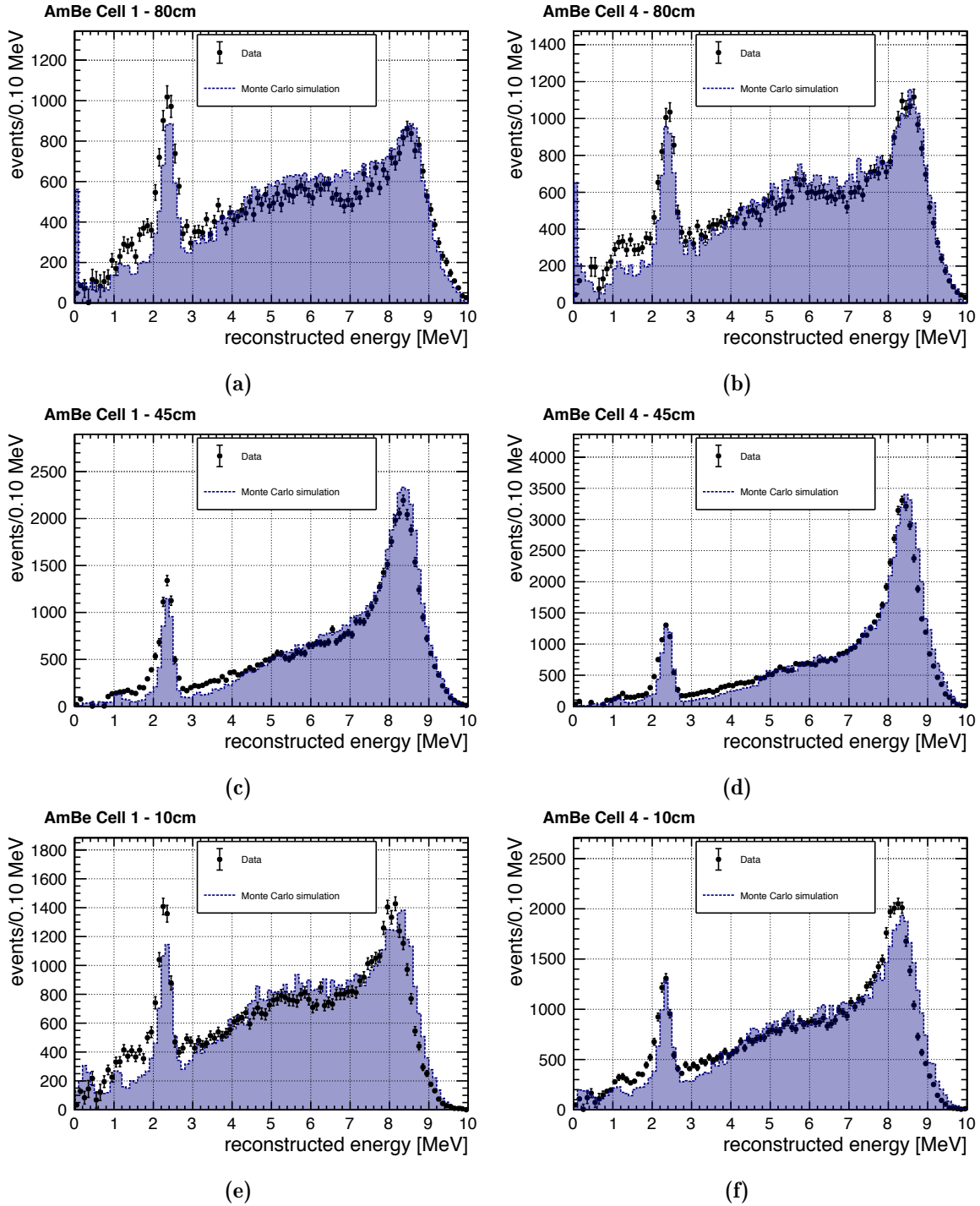
Figure 5.1.2: Reconstructed energy distributions after a neutron capture for DATA and MC simulations, using the AmBe source different heights of `Cell 1` and `Cell 4`. DATA samples are the ones from the `20180619`. MC simulation distributions are obtained using the `GLG4sim` package, are scaled to the DATA ones. Uncertainties are only statistical.

5.2 Correction Coefficients in **Phase I**

As discussed in the previous section, the use of AmBe source at different heights along the NT volume helps to understand the impact of possible border effects. During **Phase I** data acquisition, the configuration of the AmBe calibration was the one presented in Table 3.2.2, with 9 calibration positions in the entire detector. In App. A, the calibration runs performed during that phase, and the used MC simulation samples are summarized. In the following subsections, the obtained results for the $^{\text{DATA}}\!/_{\text{MC}}$ ratio of the Gd-fraction (c_{Gd}) and the IBD cut efficiency (c_{IBD}) are shown using the `GLG4sim` MC simulation.

5.2.1 Gd-fraction Efficiency

Fig. 5.2.2 displays the obtained results of c_{Gd} for the different dates of **Phase I** when the source is placed at different heights. DATA and MC values are obtained using the Eq. 4.8, and their uncertainties are only statistical (from Eq. 4.13). These uncertainties depend only on the deployment time of the source and the amount of events generated in the MC files. It can be seen that cells differ up to $\sim 1\%$ between each other. Looking in detail to the time stability, the efficiency values show a decrease in terms of time up to $\sim 1.5\%$ in all the positions. By using the averaged values over all times for each position, an efficiency mapping of the detector can be obtained. Table 5.2.1 shows the the obtained c_{Gd} together with their standard deviation (Eq. B.2). In addition, results from Table 5.2.1 have been represented in an homogeneity plot in Fig. 5.2.1a.

Looking in detail at these results, three important features are visible. First of all, values for all the cells are lower than unity. Even for `Cell 4` at $45\,\text{cm}$, the value is more than 2% below one. This discrepancy has been already observed in other LS experiments, like Double Chooz [68, 69], and it is caused by the fact that the neutron interactions are hard to simulate in this type of detectors. The second feature observed is that along the z direction (deployment axis) all the cells show a small decrease at the *top* and *bottom* regions with respect to the values at *center*. Finally, `Cell 1` is consistently below the other cells for all the deployment positions. These observations could be linked to the border effects in the neutron capture spectra already shown in Fig. 5.1.2, possibly explained by an incomplete description of either the gamma cascade or the neutron mobility. However, the lack of data and the reduced amount of values along the NT

Table 5.2.1: c_{Gd} and c_{IBD} correction coefficients for **Phase I** using `GLG4sim`. Values are obtained as the averaged value in terms of time from the different deployment dates in Fig. 5.2.2 and Fig. 5.2.3. Uncertainties are obtained statistically using the standard deviation from Eq. B.2.

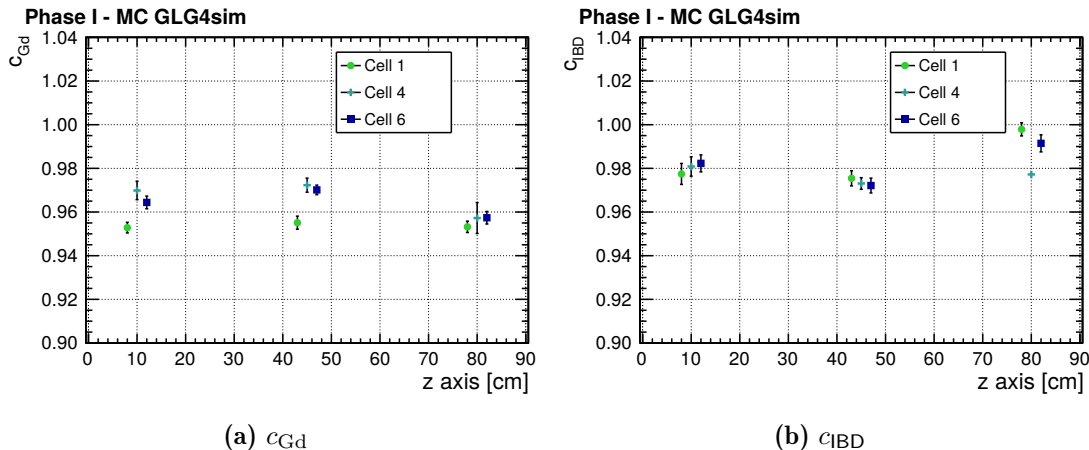| Position | Gd-fraction eff. – Phase I | | | IBD cut eff. – Phase I | | |
	Cell 1	Cell 4	Cell 6	Cell 1	Cell 4	Cell 6
top	1.005	0.976	0.992	0.952	0.957	0.958
80 cm	± 0.005	± 0.002	± 0.004	± 0.003	± 0.007	± 0.003
center	0.971	0.966	0.971	0.955	0.972	0.966
45 cm	± 0.003	± 0.003	± 0.003	± 0.003	± 0.003	± 0.002
bottom	0.979	0.983	0.986	0.953	0.969	0.964
10 cm	± 0.003	± 0.004	± 0.003	± 0.003	± 0.004	± 0.003

(a) c_{Gd}

(b) c_{IBD}

Figure 5.2.1: Homogeneity of the **(a)** c_{Gd} **(b)** c_{IBD} using GLG4sim during Phase I. Values are from Table 5.2.1. Uncertainties are obtained statistically using the standard deviation from Eq.B.2.

prevent any further conclusion. By averaging all of the values in Table 5.2.1, a global c_{Gd} for the entire NT volume can be computed

$$c_{Gd} = 0.961 \pm 0.010 \ , \tag{5.1}$$

which uncertainty is directly extracted from the standard deviation of the values. This result shows that all the c_{Gd} values in the detector are in agreement within 1%. The time fluctuation uncertainty of each point (± 0.003) is negligible for the global value. This uncertainty enclosing both, the border effects and the time stability, is considered as cell-to-cell *uncorrelated* on the global detector analysis.

5.2.2 IBD Cut Efficiency

A similar procedure as in Section 5.2.1 is applied on the estimation of the global c_{IBD} correction coefficient. In Fig. 5.2.3, the time stability of this parameter is represented for all the cells and heights. During Phase I, the c_{IBD} followed a similar trend than the c_{Gd}, although values differ more than $\sim 1\%$, and a small decreasing trend is observed comparing the four dates.

Table 5.2.1 shows the c_{IBD} correction coefficients for each cell and position. Again, uncertainties here are obtained using the standard deviation of the time averaged value. The first characteristic that can be seen from these numbers is that they are closer to 1 than c_{Gd}. This means that the IBD pair search cuts are selecting a similar amount of events in DATA and in MC simulations. If the different cells and heights are compared, no clear trend can be observed. For Cell 1 and Cell 6, a good agreement is achieved in the *top* region. As the source is moved downwards, this value decreases to ~ 0.97 with *center* and *bottom* regions in good agreement with each other. In contrast, Cell 4 displays a more uniform behavior throughout all heights, showing a clear discrepancy with the other cells at the top position. This discrepancy could be caused by the fact that during the Phase I the Buffer volume of this cell leaked the organic oil into the LS, affecting the optical properties of the LS. Nevertheless, during Phase I the information of Cell 4 was the only one used to calibrate the innermost cells of the NT, and if this low correction coefficient is an individual effect of this cell or a common decrease in the center part of the NT can not be know. For this reason, the same approach than for the global c_{Gd} has been applied:

the global c_{IBD} correction coefficient value has been computed as an average for all of the cells and positions, and its uncertainty is the standard deviation between them

$$c_{\text{IBD}} = 0.982 \pm 0.013 \ . \tag{5.2}$$

The global result shows a better agreement between DATA and MC simulations than the c_{Gd}, being the entire NT volume consistent within $\sim 1.3\%$ (with the exception of Cell 1-*top*). The time stability uncertainties are again negligible compared to this $\sim 1.3\%$ global detector uncertainty. Therefore, the uncertainty of this term is again considered cell-to-cell uncorrelated in the oscillation analysis.

5.2.3 Total Correction Coefficient, Systematic Uncertainties and Outlook

The global c_{Gd} and c_{IBD} correction coefficients and their uncertainties are summarized in Table 5.2.2. Both of these terms are combined in a total correction coefficient c_{ε}, as shown in Eq. 4.4. A final value of $c_{\varepsilon} = 0.944 \pm 0.016$ has been obtained, where its uncertainty is derived from the uncertainty propagation of c_{ε} shown in Eq. B.6. The coefficient c_{ε} significantly differs to 1 since it covers all the DATA to MC issues observed along this section: the neutron interactions not perfectly tuned in border regions and contemplated by the c_{Gd}; and the discrepancy on the Gd region concerning the peak position and its tail observed in the c_{IBD}. For these reasons, its implementation in the oscillation analysis is crucial for a proper understanding of the neutrino interactions when a DATA to MC simulation comparison is performed. The c_{ε} uncertainty has been estimated considering a conservative approach of the systematic uncertainty of c_{Gd} and c_{IBD}. The computed standard deviations of c_{Gd} and c_{IBD} along the detector volume are able to cover all the possible systematic effects of the correction coefficients such as source position deployment or energy reconstruction bias. The limited amount of information during this period has not allowed to model or understand further in detail the systematic uncertainties.

As a conclusion, as it was mentioned in previous chapter, some issues were encountered in the STEREO data analysis during Phase I. The leaks of the Buffer volumes and the increase of the light leaks due to the introduction of LS in the acrylic walls were a challenge for the detector response [45]. Besides, the obtained results of c_{ε} have pointed out additional discrepancies between DATA and MC simulations, like a small decrease in the time stability distributions and some tensions in the border regions. The addition of extra calibration positions during Phase II have allowed to perform a different correction coefficients analysis, and to do a deeper study of any systematic contribution. In the next section it is described in detail how the analysis for Phase II has been developed considering the obtained results for Phase I as a starting point.

Table 5.2.2: Summary of the c_{Gd}, c_{IBD} and the total correction coefficient c_{ε} used for the Phase I analysis with a GLG4sim MC simulation.

Phase I– GLG4sim					
Gd-fraction		**IBD cut eff.**		**Total eff.**	
c	$\pm\delta_{unc.}(c)$	c	$\pm\delta_{unc.}(c)$	c	$\pm\delta_{unc.}(c)$
0.961	0.010	0.982	0.013	0.944	0.016

(a) AmBe - 80 cm

(b) AmBe - 10 cm

(c) AmBe - 45 cm
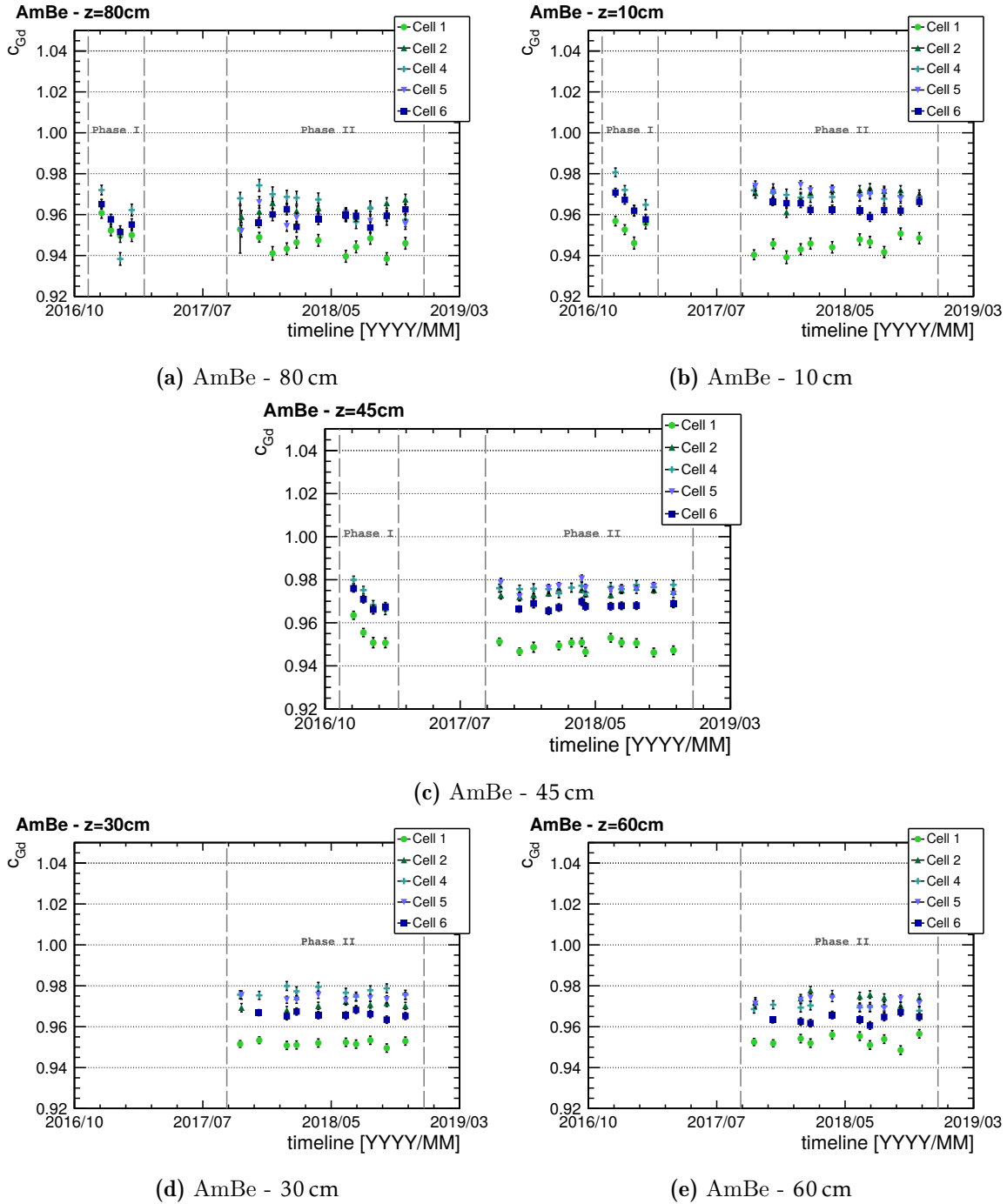
(d) AmBe - 30 cm

(e) AmBe - 60 cm

Figure 5.2.2: Time stability of the c_{Gd} using the GLG4sim MC simulation. Uncertainties are obtained for each ratio (Eq. B.7) considering the statistical fluctuation from Eq. 4.13.
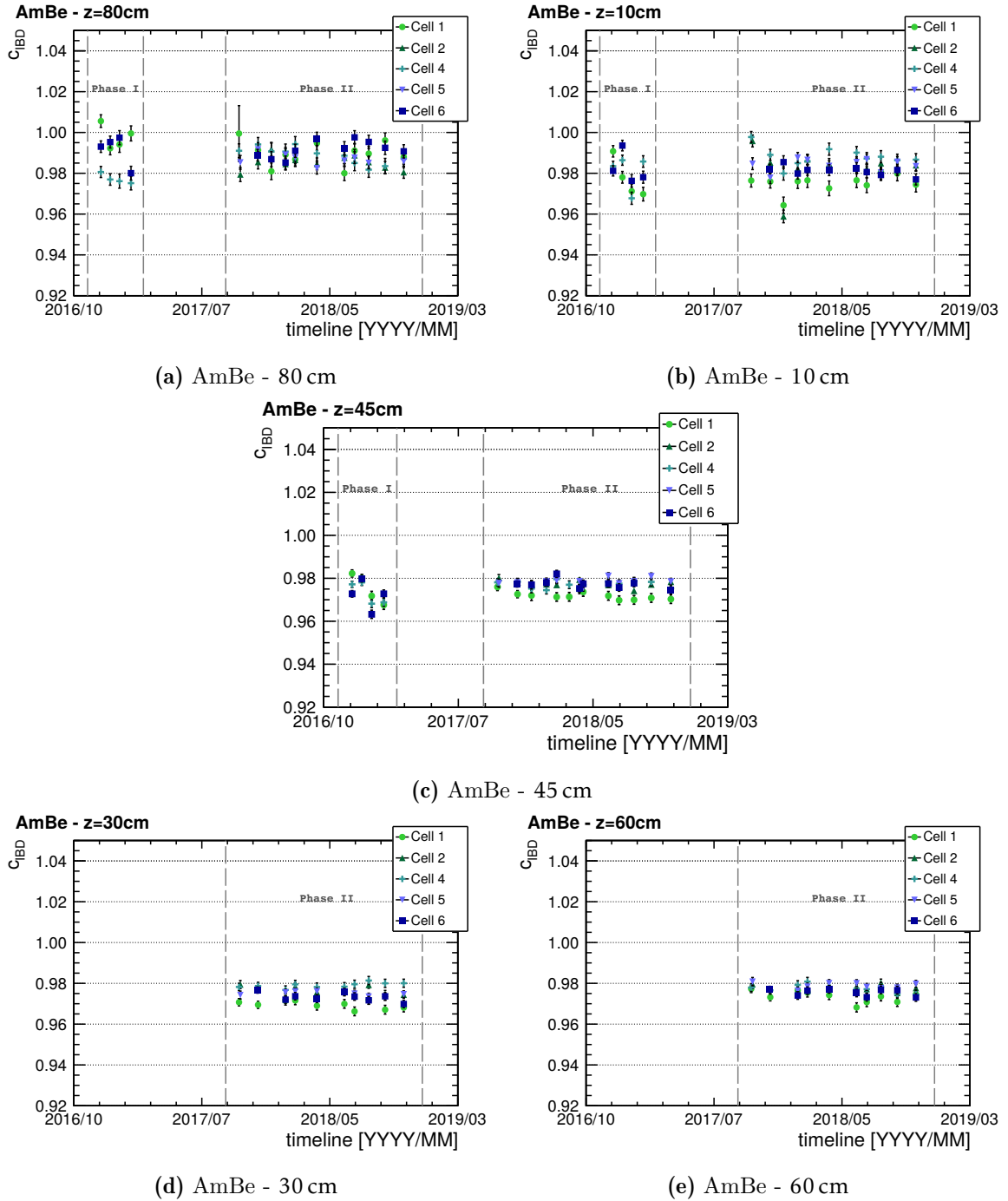
(a) AmBe - 80 cm

(b) AmBe - 10 cm

(c) AmBe - 45 cm

(d) AmBe - 30 cm

(e) AmBe - 60 cm

Figure 5.2.3: Time stability of the c_{IBD} using the MC GLG4sim simulation. Uncertainties are obtained for each ratio (Eq. B.7) considering the statistical fluctuation from Eq. 4.13.

5.3 Correction Coefficients in Phase II

The treatment of the correction coefficients values during Phase II is different from the one performed for Phase I. The increased amount of data taken and the extra calibration points allows a better observation of all the border effects mainly caused by the MC modelization of the Gd gamma cascade and the neutron mobility. Along the next subsection, a three dimensional model is defined, capable to represent the border effects observed along the xz-plane and to extrapolate it to the y-axis. This model improves the systematic uncertainties treatment of the correction factors, as described at the end of this subsection. The way the IBD cut efficiency terms are considered in the global correction factor for Phase II is also described.

5.3.1 Gd-fraction Efficiency

Results

The calculated efficiencies for fifteen calibration dates corresponding to Phase II are represented in Fig. 5.2.2. There, it can be seen that the Gd-fraction correction coefficients are more stable than the ones obtained during Phase I. Values fluctuate below the 1% for each cell independently. In a cell-to-cell comparison, a discrepancy up to a $\sim 3\%$ is regardless observed. To have a closer look to them, the averaged values are summarized in Table 5.3.1. Uncertainties are estimated considering the standard deviation of all the measurements using Eq. B.2.

Similarly to the procedure followed for Phase I, these values are represented for better comparison on an homogeneity plot in Fig.5.3.1. Two main features can be observed from these results. Firstly, all the cells present a non-homogeneous behavior along the z-axis. Values in the *top* and *bottom* regions are in agreement, but they are lower than the *center* ones. This symmetrical tendency decreasing towards the borders could be caused by the DATA to MC discrepancies observed around the Gd capture peak in Fig. 5.1.2. The area around the full energy deposition peak in the MC simulation strongly depends on the γ cascade implementation. Since this effect is observed in all the cells, with the same ratio for the $^{\text{top}}/_{\text{center}}$ and $^{\text{bottom}}/_{\text{center}}$, it is plausible that along this direction the c_{Gd} are affected mainly by this effect. Secondly, some discrepancies can be observed between the border and the inner cells. To understand them, the position of the tube has to be taken into account, specially its distance to the border of the NT. The distance with respect to the GC volumes has already been represented in Fig. 3.2.2. When the AmBe

Table 5.3.1: c_{Gd} values for Phase II using GLG4sim. Uncertainties are estimated taking into account the standard deviation of the data values.

| Position | **Gd-fraction** – Phase II | | | | |
	Cell 1	Cell 2	Cell 4	Cell 5	Cell 6
top	0.9451	0.9626	0.9647	0.9580	0.9586
80 cm	± 0.0013	± 0.0007	± 0.0003	± 0.0007	± 0.0007
top-center	0.9532	0.9543	0.9693	0.9717	0.9637
60 cm	± 0.0008	± 0.0007	± 0.0003	± 0.0007	± 0.0007
center	0.9493	0.9742	0.9760	0.9761	0.9678
45 cm	± 0.0006	± 0.0004	± 0.0003	± 0.0007	± 0.0004
center-bottom	0.9519	0.9706	0.9771	0.9741	0.9659
30 cm	± 0.0003	± 0.0003	± 0.0003	± 0.0003	± 0.0003
bottom	0.9448	0.9703	0.9693	0.9708	0.9633
10 cm	± 0.0011	± 0.0010	± 0.0004	± 0.0008	± 0.0008
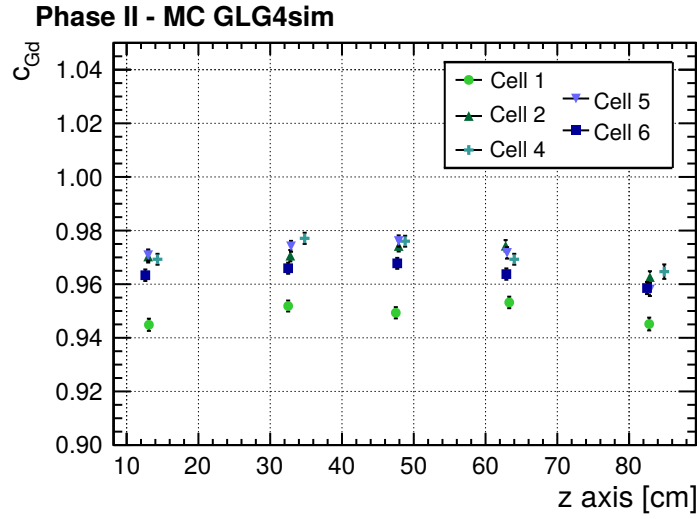
Figure 5.3.1: Homogeneity of the c_{Gd} using `GLG4sim` during Phase II. Values are from Table 5.3.1. Uncertainties are obtained statistically using the standard deviation.

source is close to a `GC` volume, the `MC` simulation is specially sensitive to the simulated neutron physics and capture cross section in the detector. In this way, if the correction coefficients are projected with respect to their distance to the nearest `GC`, the c_{Gd} ratio would be closer to 1, as the source is farther from any `GC` volume.

The discrepancies between cells and positions described above are statistically significant and a global value for the entire detector can not be computed. An alternative approach is the estimation of a Gd-fraction correction factor for each cell, $c_{\mathrm{Gd},l}$ where l represents the `NT` cells $l = 1, ..., 6$. Moreover, it needs to be taken into account that the reactor neutrino interactions are not homogeneously distributed in the entire detector volume due to the position of the detector with respect to the nuclear reactor core (see Fig. 2.2.10). Consequently, a 3 dimensional model has been created to compute a cell Gd-fraction coefficient factor $c_{\mathrm{Gd},l}$. The procedure follows two steps:

- **Step 1.** The correction coefficients from Table 5.3.1, and the position of the source with respect to the `NT` border have been used to build a three dimensional model of the Gd-fraction, $c_{\mathrm{Gd}}(x,y,z)$, where (x,y,z) corresponds to the position of the neutron creation. Each of these directions x, y and z have been treated independently creating 3 different functions $L(x)$, $W(y)$ and $H(z)$, being the global function a combination in such way:

$$c_{\mathrm{Gd}}(x,y,z) = L(x) \cdot W(y) \cdot H(z) \ . \tag{5.3}$$

- **Step 2.** Once the model is created, the correction factor for each cell $c_{\mathrm{Gd},l}$ is evaluated. A neutrino `MC` simulation taking into account the position of the STEREO detector with respect to the reactor core is used to see the position of each neutron creation in the `NT` i.e. $\equiv$ where the `IBD` interaction occur. For each neutrino interaction j, its position (x_j, y_j, z_j) has been used to compute the corresponding $c_{\mathrm{Gd}}(x_j, y_j, z_j)$. A loop over all the neutron interactions j in the `Cell` l are used to obtain the correction coefficient $c_{\mathrm{Gd},l}$:

$$c_{\mathrm{Gd},l} = \frac{\sum\limits_{j}^{\mathrm{N}_l} c_{\mathrm{Gd}}(x_j, y_j, z_j)}{\mathrm{N}_l} \ , \tag{5.4}$$

where N_l is the number of neutrons in `Cell` l. In the following subsections, each of the previously mentioned steps is described in detail for the final computation of the $c_{\mathrm{Gd},l}$.

Step 1 - The HAND Model

The c_{Gd} in Fig. 5.3.1 show that the `x` and `z` directions are affected by independent effects. Along the `z-axis` the detector appears to be sensitive to the implementation of the γ cascade implementation. Parallely the neutron mobility and cross section create a discrepancy on the border regions due to the position of the tube in the `x-axis`. For these reasons, the Height Algorithm of the Neutron Detection (`HAND`) model computing the $c_{\mathrm{Gd}}(x,y,z)$ function has been built, considering each dimension as an independent function (as it is shown in Eq. 5.3). The `z-axis` is studied with a general function for all the cells, while the `x-axis` is constructed considering that at $z = 45\,\mathrm{cm}$ the source is not affected by any *top/bottom* effect. About the `y-axis`, the only information that can be know is the position of the calibration tube in each of the cells. Since no other effect is expected in addition to the already mentioned ones, it is considered that this direction is also affected by a border effect towards the `GC`. Therefore, an extrapolation of the obtained results along the `x-axis` is used. On the following paragraphs it is described how each direction has been treated for the computation of the `HAND` model in Eq. 5.3:

x-axis: The information along this axis is the first one studied. In this case, the position of the calibration tubes along this direction is used from Fig. 3.2.2. To avoid any effect from the *top/bottom* areas, only AmBe calibration data at the *center* positions is used. In Fig. 5.3.2 the c_{Gd} values are represented, where the highest point, i.e. the measurement at $z = 45\,\mathrm{cm}$ in `Cell 4`, has been normalized to one. Thus, the rest of the points have been scaled correspondingly. As it can be seen, a flat behavior is observed in the center cells (`Cell 2, 4` and `5`). Meanwhile, the border areas `Cell 1` and `Cell 6` show a drop in the efficiency. Several options can be considered to represent this distribution, but the approach with less systematic contribution (see Section 5.4) is the use of the *Generalized normal distribution*, or *Subbotin distribution* [71]:

$$ L(x) = \frac{1}{exp\left[-\left(\mu_x/\sigma_x\right)^{\beta_x}\right]} \; exp\left[-\left(\frac{\mid x - \mu_x \mid}{\sigma_x}\right)^{\beta_x}\right] \; . \tag{5.5} $$

This exponential power distribution is described by 3 parameters: μ_x as the center of the continuum; σ_x as the width of the plateau; and the shape parameter β_x that characterizes the smoothness of the normal distribution on the border region. The function is normalized to have $L(x = 0) = 1$. The best-fit distribution is also represented in Fig. 5.3.2 and its parameters are

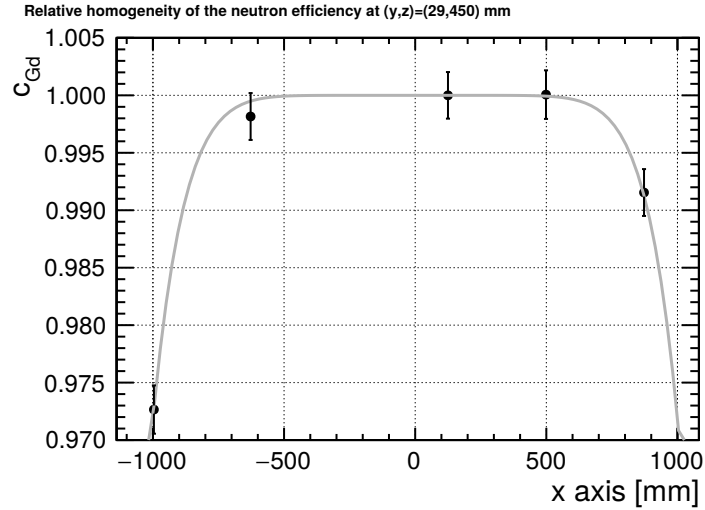$$ \begin{aligned} \sigma_x &= (1510 \pm 50) \text{ mm }, \\ \beta_x &= 8.7 \pm 0.6 \;, \end{aligned} \tag{5.6} $$

Figure 5.3.2: Relative homogeneity and fitted distribution of the c_{Gd} along the `x-axis`, for $(y, z) = (29\,\mathrm{mm}, 450\,\mathrm{mm})$. Values are from Table 5.3.1, scaled to the value for `Cell 4`. Uncertainties are statistically, with the addition of a global 0.2% to minimize the fit function $L(x)$.

for a forced central value $\mu_x \equiv 0$. This fit has converged with a $\chi^2/ndf = 1.51$, considering a global 0.2% extra uncertainty in each of the initial correction coefficient terms. The function shows a good agreement with the distribution, being able to describe the plateau and the decrease at the border regions at the same time.

z-axis: Once the `x-axis` is parametrized, a model describing the *top/bottom* effects in each cell is built. As it is shown in Fig. 5.3.1, all the cells show a similar pattern along the `z-axis`. Therefore a global fit for all the efficiency values from Table 5.3.1 has been the chosen strategy. One could expect that a parabolic function is a good approach for these values due to the symmetric shape between cells; but since it is necessary not only to take into account absolute discrepancies between the maximums but also the relative ones, a different parametrization has been considered:

$$H(z) = e_l \cdot \left[a_z \cdot (z - d_z)^2 + 1 \right] . \tag{5.7}$$

This function depends on two parameters a_z and d_z considered common for all the cells since they describe the shape of the parabola and the position of its maximum respectively. Since the set of correction coefficients for each cell is placed at different heights, the value e_l is externally introduced to represent the position of the local top of the parabola. This term is taken from the previous evaluation of $L(x)$ (from Eq. 5.5), considering that this function is normalized by the c_{Gd} of `Cell 4` at $45\,\mathrm{cm}$:

$$e_l = L_{norm}(x_i) \rightarrow \begin{cases} e_1 = & 0.9494 \ , \\ e_2 = & 0.9754 \ , \\ e_4 = & 0.9759 \ , \\ e_5 = & 0.9758 \ , \\ e_6 = & 0.9674 \ . \end{cases} \tag{5.8}$$

79
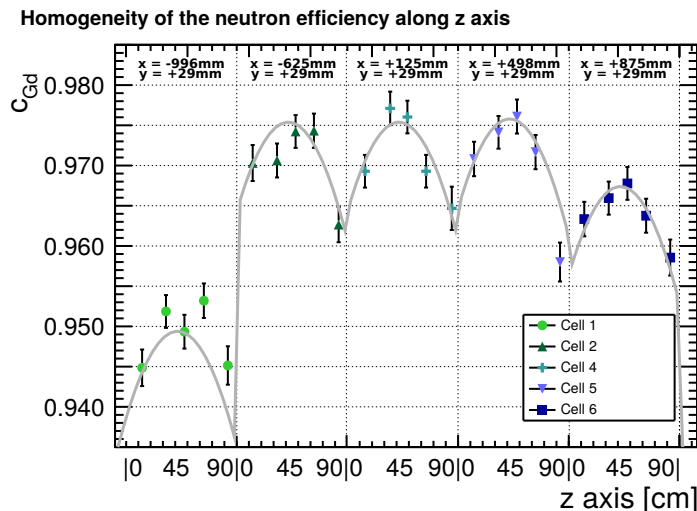
Figure 5.3.3: Homogeneity and fitted distribution of the c_{Gd} along the z-axis for all the cells. Values are from Table 5.3.1. Uncertainties are statistically, with the addition of a global 0.2% to minimize the fit function $H(z)$.

In Fig. 5.3.3, the previously mentioned efficiency values and the fitted distribution from Eq. 5.7 are represented. The same a_z and d_z parameters for all the cells are able to reproduce the parabolic trend along the z-axis. Some discrepancies are observed for Cell 1, since the obtained value at the *center* is a little bit shifted creating therefore some tension with the *top-center* and *center-bottom* points. With only this exception, the obtained results of

$$a_z = (-6.6 \pm 0.6) \cdot 10^{-6} \ \frac{1}{\text{mm}} \ ,$$
$$d_z = (420 \pm 16) \ \text{mm} \ ,$$

(5.9)

allow to create this distribution with a goodness of the fit of $\chi^2/ndf = 1.73$, taking into account a global 0.2% extra systematic uncertainty for all the terms.

y-axis: No information is obtained from the AmBe calibration along this axis since all calibration tubes are aligned at the same position ($y = 29\,\text{mm}$). Along the y-axis, the NT is also delimited by the GC volumes of GCIN20 and GCD19, and thus border effects towards these volumes are expected in the c_{Gd}. Since the GC border effect is already modeled with the x-axis function Eq. 5.5, a reasonable approach is that $L(x)$ is extrapolated into the y-axis. Therefore, the $W(y)$ can be parametrized as:

$$W(y) = \frac{1}{N} \ exp\left[-\left(\frac{|\,y - d_{xy} - \mu_x\,|}{\sigma_x}\right)^{\beta_x}\right]$$
$$\text{with } d_{xy} = \begin{cases} -(d_x - d_y)/2 & \text{if } y > 0 \\ (d_x - d_y)/2 & \text{if } y \leq 0 \end{cases}$$

(5.10)

where the parameters μ_x and σ_x from Eq. 5.6 are considered, and d_{xy} takes into account the length difference of the NT volume along the x-axis (d_x), and the y-axis (d_y). The $W(y)$ function should also be normalized (with the parameter N), to make $c_{Gd}(x,y,z)$ converge to
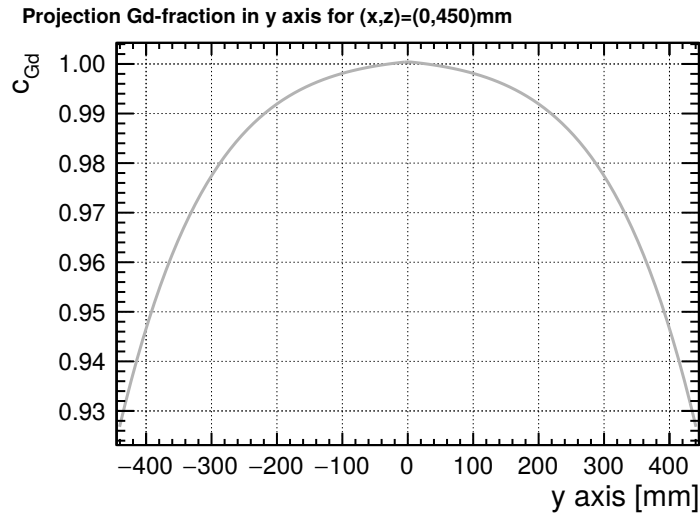
Figure 5.3.4: Used distribution of the c_{Gd} along the `y-axis` for all the cells.

the observed results along the calibration tubes. Since it is placed at $y = 29\,\mathrm{mm}$, the parameter N will satisfy the normalization to 1 at that position, being the maximum of Eq. 5.10 above 1. The shape of this extrapolation considering the size of the detector is represented in Fig. 5.3.4.

The `HAND` model can give a representation of how the correction coefficient map of Table 5.3.1 would extrapolate to the entire detector volume. In Fig. 5.3.5, the `HAND` model is represented for the `xz-plane` of the detector. As it can be seen, the $c_{\mathrm{Gd}}(y = 0|x, z)$ function can reproduce the border effects of `Cell 1` and `Cell 6`, and the global behavior in the center cells. *Top* and *bottom* regions are also well reproduced, creating an small asymmetry due to the fact that the maximum of the $H(z)$ function is placed slightly below the center of the tube (see values in Eq. 5.9). Overall, it can be concluded that these functions can reproduce the discrepancies between the Gd-fraction efficiency terms between DATA and MC. A deep study about the systematic uncertainties coming from this method is described in Section 5.4.
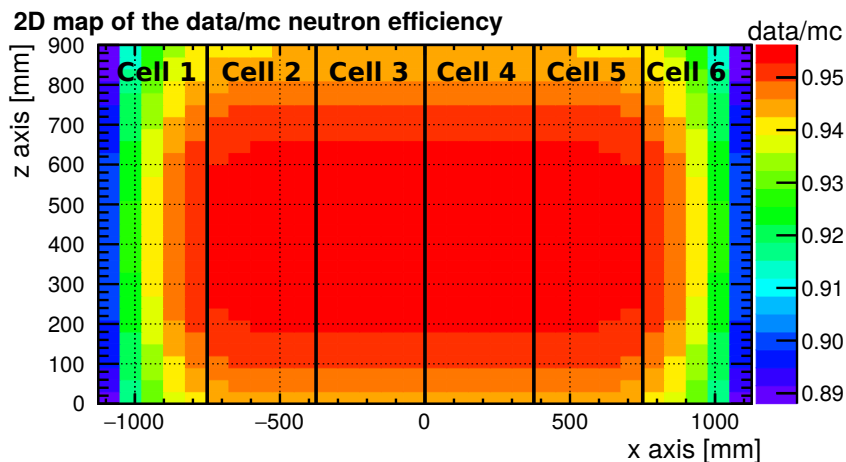
Figure 5.3.5: Distribution of the $c_{\mathrm{Gd}}(x, y, z)$ along the `xz-plane` for $y = 0$.

Table 5.3.2: c_{Gd} values for each cell l after the implementation of the HAND model in a neutrino MC simulation. Uncertainties will be described an summarized in Section 5.4.

	Cell 1	Cell 2	Cell 3	Cell 4	Cell 5	Cell 6	NT
n events	11,569	10,224	9,469	8,964	5,602	8,023	54358
corrected n events	10,715	9,713	8,998	8,519	8,076	7,436	51341
$c_{\mathrm{Gd},l}$	0.9262	0.9501	0.9503	0.9504	0.9499	0.9269	0.9445

Step 2 - Reactor Neutrino Flux

The HAND model function $c_{\mathrm{Gd}}(x,y,z)$ can reproduce how the Gd-fraction term looks at any point of the detector. For an homogenous neutrino distribution, the mean integral of this function over the volume of the cells gives the correction coefficient for each of them. However, the neutrino flux has some directionality since the STEREO detector is not radially oriented with respect to the reactor core, and together with the inverse square law, a reduction of the amount of neutrinos is expected for the farther cells. This was represented in Fig. 2.2.10, where the STEREO detector (orange color) is slightly tilted with respect to the right solid angle $d\Omega$ area. Consequently, for the calculation of the $c_{\mathrm{Gd},l}$ it is necessary to consider the inhomogeneity of the neutrino interaction. The applied procedure uses a neutrino MC simulation to check the position (x,y,z) of the neutrino interactions. This position is used both, to tag the event in a specific cell and to compute the $c_{\mathrm{Gd}}(x,y,z)$, as it has been shown in Eq. 5.4. The obtained results after checking a MC neutrino simulation in which 617,734 neutrons have been generated in the detector, are summarized in Table 5.3.2.

The directionality of the neutrinos creates non-symmetric correction coefficients along the detector volume, and gives a realistic approach of the DATA/MC correction factors. Besides, this accurate method provides a value for Cell 3 that can only be extrapolated from the neighbor cells. These values are the final correction coefficients used for the Phase II fit. No uncertainties are quoted in the table, since a detailed description can be found in Section 5.4.

5.3.2   IBD Cut Efficiency

Following the same procedure as in Phase I, the values of the c_{IBD} have been estimated for fifteen calibration dates, and are compared to a MC simulation. These values are shown in Fig. 5.2.3. The correction coefficients for Phase II show a steady behavior around the ∼0.98 mark, with a dispersion lower than $\sim 1.5\%$. Making a cell-to-cell comparison, there is no disagreement between the center and the border volumes of the NT for any of the heights.

An averaged value is estimated for each cell and calibration height. They are summarized in Table 5.3.3, and represented in a homogeneity plot in Fig. 5.3.6. Following what has been seen on the stability plots, a good agreement between cells can be observed. The plotted values could point to a possible *top/bottom* effect, but below the $\sim 1\%$. In contrast to c_{Gd}, the obtained results for the c_{IBD} are stable along the entire detector. A small asymmetry between the *center* and the *top/bottom* regions also appears along the z-axis. Since this effect is below the $\sim 1\%$, the c_{IBD} does not require modelling and a global c_{IBD} value is computed for the entire NT volume.
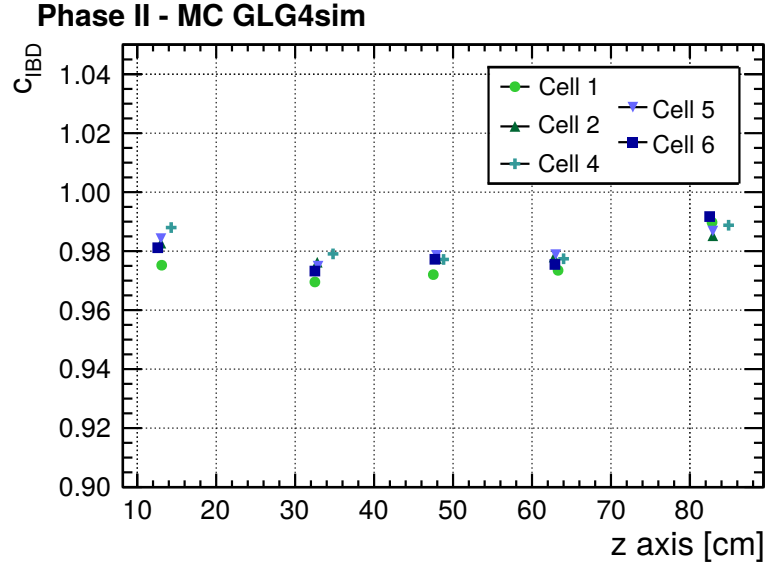
Figure 5.3.6: Homogeneity of the c_{IBD} using `GLG4sim` during Phase II. Values are from Table 5.3.3. Uncertainties are obtained statistically using the standard deviation.

Following the same procedure that was applied for Phase I an averaged value of the detector is obtained,

$$c_{\text{IBD}} = 0.9797 \pm 0.0059 \; . \tag{5.11}$$

Due to the increased amount of calibration DATA samples and the good agreement between the different cells and positions, the standard deviation of the global c_{IBD} is a factor two smaller than the one obtained for Phase I (Eq. 5.2). However, for Phase II a detailed systematic uncertainty is computed to cover any discrepancy along the cells height. More details can be found in the following section.

Table 5.3.3: c_{IBD} values for Phase II using `GLG4sim`. Uncertainties are estimated taking into account the standard deviation of the data values.

	IBD cut eff. – Phase II				
Position	**Cell 1**	**Cell 2**	**Cell 4**	**Cell 5**	**Cell 6**
top	0.9898	0.9852	0.9887	0.9867	0.9915
80 cm	± 0.0018	± 0.0011	± 0.0012	± 0.0009	± 0.0013
top-center	0.9735	0.9780	0.9774	0.9788	0.9755
60 cm	± 0.0009	± 0.0005	± 0.0007	± 0.0005	± 0.0005
center	0.9720	0.9775	0.9772	0.9786	0.9772
45 cm	± 0.0006	± 0.0004	± 0.0004	± 0.0005	± 0.0007
center-bottom	0.9695	0.9762	0.9790	0.9749	0.9732
30 cm	± 0.0006	± 0.0008	± 0.0004	± 0.0003	± 0.0007
bottom	0.9752	0.9827	0.9879	0.9842	0.9812
10 cm	± 0.0013	± 0.0027	± 0.0013	± 0.0010	± 0.0007

5.4 Systematic Uncertainties in Phase II

An extensive study of the systematic uncertainties have been performed on c_{Gd} and c_{IBD} for Phase II. Several sources of error uncertainty are taken into account, and described in the following sections. A summary of the Phase II correction coefficients, together with their uncertainty is described in Section 5.5 and Section 5.6.

5.4.1 Time Stability

The first contribution taken into account in the calculation of the final correction coefficients uncertainty comes from the time variation during the DATA acquisition. This term contains not only statistical fluctuation information, but also external effects affecting distinctly the different calibration runs. For example, temperature and pressure changes, detector response variations, inaccuracies during the manual source deployment, etc. The uncertainties already described in Table 5.3.1 and Table 5.3.3 represent these time fluctuations, independent to each calibration position and laying around the 0.10% mark. Fig. 5.2.2 and Fig. 5.2.3 portray these time fluctuations in similar ways for both correction coefficients, displaying a cell wise uncorrelation between these efficiency terms.

5.4.2 Energy Reconstruction Bias

A second study considers possible bias on the energy reconstruction between DATA and MC distributions. As it is seen in Fig. 5.1.2, the position of the hydrogen and gadolinium full energy deposition peaks differ slightly between DATA and MC, and they do it in a different way for each position along the z-axis. This discrepancy between samples could be caused by energy reconstruction issues related neither to the source nor to the MC simulation. In addition to the energy reconstruction contribution in the global systematic uncertainty (see Table 2.2.2), their impact in the efficiency would be included as systematic uncertainty of the correction coefficients. These terms are strongly dependent on the energy cuts, for which the reconstructed energy is crucial and any minor change would affect the number of events observed.

The procedure to quantify the impact of a bias in the energy reconstruction is the re-evaluation of the correction coefficients under a global energy shift R. This shift has been estimated using the position of the reconstructed hydrogen peak in both DATA and MC, computed as

$$R = \frac{\mu_{DATA}}{\mu_{MC}} \tag{5.12}$$

using the mean values μ from a fit like the one already shown in Eq. 3.6. The global shift R has been applied on the MC energy reconstruction code, being considered in an event-by-event basis. The efficiency results obtained after this shift have been compared again to the DATA efficiency correction factors. To have a full control over the entire volume, this analysis has been performed in the center and both border cells, at three different positions summarized in Table 5.4.1.

By inspecting c_{Gd} cell-by-cell, it is possible to see that the *center* values are not affected by any change in the energy reconstruction. Such result is expected since this position is less sensitive of this MC bias. In the *top* region, values differ but stay still within the statistical fluctuations already mentioned in the previous subsection ($\sim 0.10\%$). On the contrary, the *bottom* region portrays larger discrepancies between cells, specially for Cell 1 and Cell 6. Contrarily, the obtained values for the c_{IBD} differ significantly on both *top* and *bottom* regions. In this case,

Table 5.4.1: Discrepancy between DATA and MC correction coefficients using the normal energy reconstruction, and adding the correction factor R from Eq 5.12 to the global reconstructed values.

| | Gd-fraction eff. | | | | | | IBD cut eff. $-$ Phase II | | | | | |
| | Cell 1 | | Cell 4 | | Cell 6 | | Cell 1 | | Cell 4 | | Cell 6 | |
	MC normal	MC corr.	MC normal	MC corr.	MC normal	MC corr.	MC normal	MC corr.	MC normal	MC corr.	MC normal	MC corr.
top	0.9451	0.9441	0.9647	0.9631	0.9586	0.9567	0.9898	0.9882	0.9887	0.9853	0.9917	0.9829
	-0.10%		-0.16%		-0.19%		-0.16%		-0.34%		-0.88%	
center	0.9493	0.9492	0.9760	0.9761	0.9678	0.9676	0.9720	0.9712	0.9772	0.9768	0.9772	0.9765
	-0.01%		+0.01%		-0.02%		-0.08%		-0.04%		-0.07%	
bottom	0.9448	0.9472	0.9693	0.9697	0.9633	0.9651	0.9752	0.9811	0.9879	0.9919	0.9812	0.9884
	+0.24%		+0.04%		+0.18%		+0.59%		+0.40%		+0.72%	

values reach a discrepancy of 0.88%. Meanwhile, the center region is not affected by this energy reconstruction change in the same fashion as for c_{Gd}. These discrepancies have been considered as the impact of an energy reconstruction bias in the correction coefficient factors. The averaged absolute error is estimated (Eq. B.4), and it is considered as the systematic component from this source. The uncertainty for the c_{Gd} is 0.11%, which is a value of the same order as the time fluctuation uncertainty discussed in the previous section. Meanwhile, the averaged absolute error of c_{IBD} is 0.36%, 3 times larger than the statistical fluctuation obtained for the c_{Gd}. Even if these discrepancies occur in the same direction for both efficiency terms, it is clear that the impact is different for each correction coefficient term. Therefore, a full uncorrelation between the efficiency terms is assumed. On the same way, since the effect is not the same between cells, these uncertainties take part of the cell-to-cell uncorrelated contribution.

5.4.3 Source Position Bias

The third analysis developed in the search for possible systematic sources of uncertainty is focused in the test of a possible position bias between the calibration DATA samples and the MC simulation. As it was highlighted in Section 4.2.5, a shift of the source position can create a discrepancy between DATA and MC, mostly on the border regions which are more sensitive to any gamma escape. During the analysis of Phase II calibration DATA, some inaccuracies on the labeled positions of the calibration cables along the z-axis have been observed. These positions have been corrected and introduced properly in the MC simulation. To account for this type of uncertainty a new systematic source h introduced in the analysis. To quantify this effect, a set of MC simulations with a systematic shift in all the positions have been produced. In this case, the position of the source in the simulation have been increased with global $+1\,\mathrm{cm}$ for all the deployments along the z-axis. Only the information of Cell 4 has been studied in this analysis with the purpose of isolating this systematic error from border effects. The obtained results for the different configurations are summarized in Table 5.4.2.

Comparing the *top* and *bottom* heights, it is observed that for both efficiency terms differs significantly from the standard values, but with opposite directions. More concretely, the efficiency at the *top* region decreases while it increases at the *bottom* of the detector. Such effects comes from the fact that shifting the simulated position of the source upwards approaches the source to the top border in the case of the *top* position, while effectively moving it away from the bottom border for the *bottom* position. This reduces the agreement for the former and increases it for

Table 5.4.2: Discrepancy between c_{Gd} and c_{IBD} values using the position in DATA and MC and adding an extra source position in the MC.

Cell 4 position	Gd-fraction eff.			IBD cut eff. $-$ Phase II		
	$pos_{MC} = pos_{DATA}$	$pos_{MC} = pos_{DATA}+1\,cm$	diff.	$pos_{MC} = pos_{DATA}$	$pos_{MC} = pos_{DATA}+1\,cm$	diff.
top	0.9647	0.9610	-0.37%	0.9887	0.9818	-0.69%
top-center	0.9693	0.9709	+0.16%	0.9774	0.9759	-0.15%
center	0.9760	0.9768	+0.08%	0.9772	0.9781	-0.09%
center-bottom	0.9770	0.9610	-0.01%	0.9788	0.9818	-0.02%
bottom	0.9693	0.9739	+0.46%	0.9879	0.9918	+0.39%

the latter. For the *center* positions, the discrepancies are not significant and are within the statistical uncertainty. The averaged absolute errors for the c_{Gd} and the c_{IBD} are 0.22% and 0.27% respectively. These values are considered as the contribution of the total systematic uncertainty from the source location uncertainty. This position bias is in a similar order of magnitude for c_{Gd} and c_{IBD}, and points out to the same direction in each of the positions. Therefore, a full correlation is going to be considered between both efficiency terms in this type of systematic source. Since this effect is independent of any other border issue, the collected information for `Cell 4` will be used to describe all of the cells in the detector. Consequently, these uncertainties are considered cell-to-cell uncorrelated for both c_{Gd} and c_{IBD} efficiency terms.

5.4.4 Inhomogeneity Model - Gd-fraction Efficiency

Finally, a systematic term concerning the spatial homogeneity treatment of the correction coefficients is included. In this case, each efficiency term is treated independently. To analyze the spatial inhomogeneites of the calculation of c_{Gd}, the `HAND` model developed in Section 5.3.1 is used. This treatment uses: a **cell-to-cell uncorrelated term** evaluating the model; and one **cell-to-cell correlated term** studying different parametrizations These two computations are covering any possible systematic effect in the treatment of the Gd-fraction correction coefficients, and are summarized in the final Section 5.5.

Cell-to-cell Uncorrelated Systematic Uncertainty: This term has been computed by comparing the obtained coefficients from the AmBe calibration runs summarized in Table 5.3.1, and the obtained values after the evaluation of the $c_{Gd}(x, y, z)$ `HAND` model at the position where the source is deployed. Considering the position of the calibration tubes in Fig. 3.2.2 and the position of the source from Table 3.2.2, the discrepancy value Δ for `Cell` l at the height `z` is defined as

$$\Delta_{l,z} = c_{Gd}\Big|_{\text{Table 5.3.1}} - c_{Gd}(x_l, y_l, z) \ . \tag{5.13}$$

The values of $\Delta_{l,z}$ are represented in Fig. 5.4.1a. A good agreement at the *bottom* and *center* positions can be seen, with Δ values below $\sim 0.25\%$. The higher discrepancies are observed at the *bottom-center* position, and at the *top*. In the last case, the obtained values reach a difference of $\sim 0.70\%$. Looking into the $\Delta_{l,z}$ distribution for all of the positions in Fig. 5.4.1b, the discrepancy values distribute normally around $\Delta = 0$. The highest discrepancy would be within the 2σ range at a 90% confidence level. In this scenario, and interpreting such discrepancies as the systematic uncertainty of the $c_{Gd}(x, y, z)$ model,
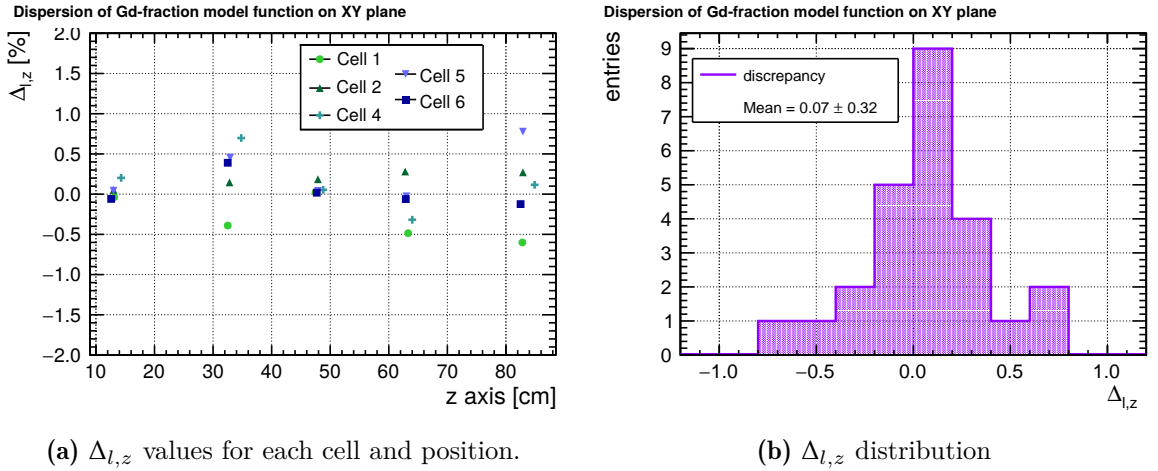
(a) $\Delta_{l,z}$ values for each cell and position.

(b) $\Delta_{l,z}$ distribution

Figure 5.4.1: Obtained $\Delta_{l,z}$ values using the Eq. 5.13 initial values from Table 5.3.1 and the `HAND` model for `GLG4sim`.

$$\Delta_{l,z}\Big|_{max} = 0.70\% \equiv 2\sigma \Rightarrow \sigma = 0.35\% \ . \tag{5.14}$$

This value 0.35% covers all possible systematic effects of the data treatment, and is considered a conservative approach of the cell-to-cell uncorrelated systematic uncertainty. It only contains the information of any fluctuation between the model, and initial parameters. In the next section the uncertainty coming from the model would be described.

Cell-to-cell Correlated Systematic Uncertainty: In this paragraph, the cell-to-cell correlated uncertainty estimation is detailed. As it has been described in Section 5.3.1, the $c_{\mathrm{Gd}}(x,y,z)$ `HAND` function is built from the composition of a normal distribution along the `x-` and `y-axis`, and a parabolic behavior for the `z-axis`. Given that the cells are placed along the `x-axis`, only $L(x)$ function is inspected for a cell-to-cell correlated systematic uncertainty. This $L(x)$ function is created using 5 calibration points, that can not provide accurate information about the transition from the plateau to the parabolic trend when the source is close to the borders, exactly at the end point of the function when it touches the border of the `NT`. To account for these two information gaps, a second function is defined to test the reliability of $L(x)$ in these areas. In this case, a function defined by parts is considered:

$$L_{\mathsf{TEST}}(x) = \begin{cases} -a_{\mathsf{T}} \cdot (x + pos)^2 + b_{\mathsf{T}} \cdot (x + pos) + 1 & \text{if } x < -pos \ , \\ 1 & \text{if } -pos < x < pos \ , \\ -a_{\mathsf{T}} \cdot (x - pos)^2 + b_{\mathsf{T}} \cdot (x - pos) + 1 & \text{if } x > pos \ , \end{cases} \tag{5.15}$$

which consist of a flat constant and two symmetric parabolic contributions. $L_{\mathsf{TEST}}(x)$ depends on three parameters: a_{T} and b_{T} which describe the shape of the parabolic distributions, and *pos* which represents the point where the flat contribution begins and finishes. This **TEST function** has been used to

(a) $L(x)$

(b) $W(y)$
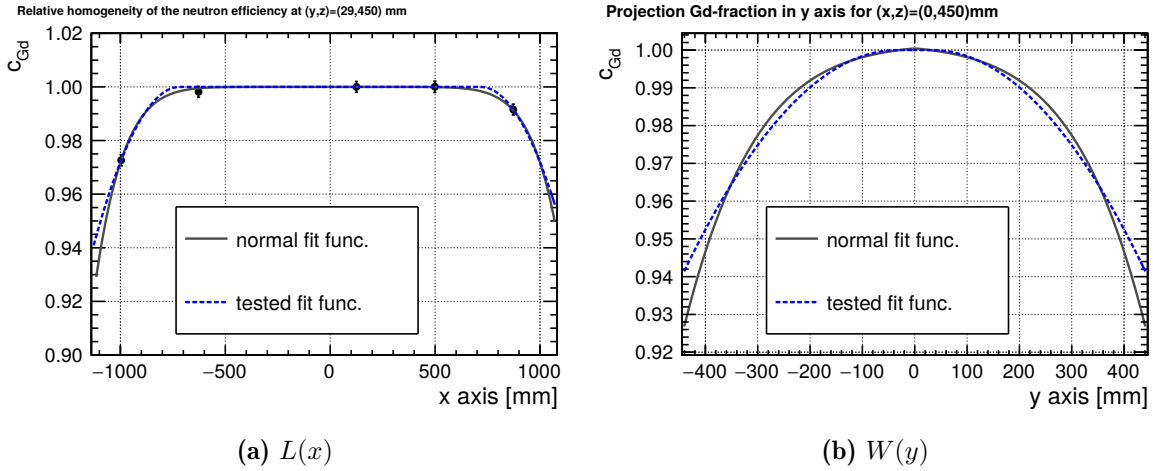
Figure 5.4.2: Shape of the $L(x)$ and $W(y)$ functions using the HAND model and the TEST function from Eq. 5.15.

fit the obtained values at the *center* of the cells, leading to the distribution shown in Fig. 5.4.2a. It represents a simple approach that matches with the correction coefficients. The corresponding parametrization satisfying the Fig. 5.4.2a are,

$$
\begin{aligned}
a_{\mathsf{T}} &= (3.5 \pm 1.2) \cdot 10^{-7} \ \mathrm{mm}^{-2} \ , \\
b_{\mathsf{T}} &= (6.332 \pm 0.006) \cdot 10^{-12} \ \mathrm{mm}^{-1} \ , \\
pos &= 720 \pm 40 \ \mathrm{mm} \ .
\end{aligned}
\tag{5.16}
$$

To quantify the impact of this **TEST function**, a new $c_{\mathrm{Gd}}(x,y,z)$ has been constructed,

$$
c_{\mathrm{Gd}}^{\mathsf{TEST}}(x,y,z) = L_{\mathsf{TEST}}(x) \cdot W_{\mathsf{TEST}}(y) \cdot H(z) \ .
\tag{5.17}
$$

Since the construction of $W(y)$ is inherently attached to $L(x)$, in this case it also has to be substituted by $W_{\mathsf{TEST}}(y)$. The way the y-axis function using the TEST model looks like is represented in Fig. 5.4.2b. As it can be seen, this axis is also affected by the end position of the correction coefficient function when a neutron interacts closer to the GC wall.

With this new function $c_{\mathrm{Gd}}^{\mathsf{TEST}}(x,y,z)$, the correction coefficients ratios considering the reactor neutrino flux have been obtained inserting the TEST function in Eq. 5.15. Values obtained for each cell are summarized in Table 5.4.3, together with the NT result. Both 3D models have been compared, and the discrepancy between the respective correction coefficients is also included in the table. For the center cells (Cell 3 and 4), there is not big discrepancy between both functions. This is because the x-axis component has the same plateau for both of them, and any discrepancy is only coming from the y-axis. Consequently, the border cells are more affected reaching a $\sim 0.4\%$ discrepancy between both models. The discrepancies between the HAND model and the TEST function give a conservative approach of the two problematic regions aforementioned. Their discrepancy are considered as the systematic uncertainty, in this case for the cell-to-cell correlated component.

Table 5.4.3: c_{Gd} values for each cell l after the implementation of the TEST model in a neutrino MC simulation. Values are compared to the ones obtained with the HAND model in Table 5.3.1. The absolute discrepancy between both models is considered as the cell-to-cell correlated uncertainty.

	Cell 1	Cell 2	Cell 3	Cell 4	Cell 5	Cell 6	NT
$c_{\text{Gd},l}^{\text{TEST}}$	0.9304	0.9520	0.9518	0.9518	0.9518	0.9310	0.9445
$c_{\text{Gd},l}^{\text{HAND}}$	0.9262	0.9501	0.9503	0.9504	0.9499	0.9269	0.9420
abs. discrep. [%]	0.42	0.19	0.15	0.15	0.19	0.41	0.25

5.4.5 Homogeneity Model - IBD Cut Efficiency

In the case of the IBD cut efficiency, no homogeneity model has been used. The overall c_{IBD} term in Eq. 5.2 has been computed considering the averaged value for all the cells and positions. Its uncertainty 0.59% has been calculated using the mean error of the standard deviation described in App. B, and it conservatively covers all the possible inhomogeneities of the term. Therefore, this value has been taken into account as the *systematic homogeneity* term of the IBD cut efficiency.

5.4.6 Summary of the Uncorrelated Systematic Uncertainties

The previously quoted values concerning the cell-to-cell uncorrelated systematic uncertainties are summarized in Table 5.4.4. An overall value of 0.44% has been obtained for the c_{Gd} term, which is mostly dominated by the source position bias component and the homogeneity uncertainty. Concerning the computation of the c_{IBD}, a final value of 0.75% has been retrieved. In this case, it is mostly caused by the inaccuracy of the energy reconstruction and the inhomogeneity of the correction coefficients. Combining both systematic uncertainty terms, and taking into account the efficiency-to-efficiency correlation, a value of 0.90% of cell-to-cell uncorrelated systematic uncertainty is reached for the total correction coefficient. The cell-to-cell correlated uncertainty terms are the same as the already listed ones in Table 5.4.3, computed testing a different fit function for the AmBe efficiency ratios. All of these correlated and uncorrelated systematic values are compiled in the following section.

Table 5.4.4: Summary of the cell-to-cell uncorrelated uncertainties for the c_{Gd} and the c_{IBD} using the GLG4sim package for the MC simulation.

Syst. source	Gd-fraction [%]	IBD cut eff. [%]	eff to eff corr. [%]
time variation	0.10	0.10	0
energy reco. bias	0.11	0.36	0
source pos. bias	0.22	0.27	100
homogeneity uncert.	0.35	0.59	0
total	0.44	0.75	

Table 5.5.1: Obtained c_{Gd} and c_{IBD} correction coefficients and their uncorrelated ($\delta_{unc.}(c)$) and correlated ($\delta_{c.}(c)$) cell-to-cell total uncertainties using the GLG4sim package. The c_{tot} values are computed using Eq. 4.4, and their uncertainties are obtained considering the correlations of Table 5.4.4.

<div align="center">Phase II– GLG4sim</div>

Cell	Gd-fraction			IBD cut eff.			Total eff.		
	c	$\pm\delta_{unc.}(c)$	$\pm\delta_{c.}(c)$	c	$\pm\delta_{unc.}(c)$	$\pm\delta_{c.}(c)$	c	$\pm\delta_{unc.}(c)$	$\pm\delta_{c.}(c)$
1	0.9262		0.0042				0.9074		0.0042
2	0.9501		0.0019				0.9308		0.0019
3	0.9503		0.0015	0.9797	0.0075	–	0.9310		0.0015
4	0.9504	0.0044	0.0015				0.9311	0.0090	0.0015
5	0.9499		0.0019				0.9306		0.0019
6	0.9269		0.0042				0.9081		0.0041

5.5 Correction Coefficients for Oscillation Analysis

The already mentioned IBD cut efficiency and Gd-fraction correction coefficient terms are presented in Table 5.5.1, where each cell volume is computed individually. The total correction coefficient c_ε from Eq. 4.4 is also estimated for each cell, and can be found in the same table. The correction coefficient c_ε lies between 0.9074 and 0.9311. The position of the STEREO detector with respect to the reactor core creates a different correction coefficient for Cell 1 and 6. The global uncertainty of the total correction coefficient is approximately between 0.91% and 0.99%, with a higher value on the border cells due to the lack of information on the y-axis. These values have been used for the evaluation of the oscillation analysis presented in Table. 2.3.1-**(ii)**.

5.6 Correction Coefficients for the Absolute Normalization of the Neutrino Flux

The correction coefficients summarized in Table 5.5.1 are the ones used for the oscillation analysis described in Section 2.2.6. However, for the evaluation of the absolute normalization of the neutrino flux a global correction coefficient $\langle c_\varepsilon \rangle$ for the entire NT needs to be computed. This value is crucial for the comparison of the detected and predicted neutrino fluxes, and it is implemented in analysis of the electron anti-neutrino rate mentioned in Section 2.2.5. The global correction coefficient is constructed as the previous ones,

$$\langle c_\varepsilon \rangle = \langle c_{Gd} \rangle \cdot \langle c_{IBD} \rangle \,, \tag{5.18}$$

and can be estimated as the correction coefficients for the oscillation analysis. For the IBD cut efficiency $\langle c_{IBD} \rangle$, the global correction coefficient is already computed in Table 5.5.1,

$$\langle c_{IBD} \rangle = 0.9797 \pm 0.0075 \text{ (cell-to-cell corr.)} \,. \tag{5.19}$$

The uncertainty of $\langle c_{IBD} \rangle$ is the one summarized in Table 5.4.4, and it encloses both the statistical and the systematic component from the previous analysis. However, this term covers the entire detector absolute efficiency, and no extra information can be obtained concerning uncertainty correlations. For that reason, the most conservative approach is to assume a full cell-to-cell correlation on this uncertainty.

For the Gd-fraction correction coefficient, a global detector value needs to be computed. Following the same procedure than for the correction coefficients, a `NT` value can be obtained taking into account the reactor flux and the three dimensions c_{Gd} model. This value already estimated in Table 5.3.2 is

$$\langle c_{\mathrm{Gd}} \rangle = 0.9420 \pm 0.0050 \text{ (cell-to-cell corr.)} , \tag{5.20}$$

but in this case its uncertainty 0.50% is obtained from the combination of two separately uncertainties: a first term 0.42% which is considering the time stability, source position and energy reconstruction bias, and the homogeneity systematic uncertainty from Table 5.4.4; and secondly the obtained value of 0.25% from the discrepancy between two different models, summarized in Table 5.4.3. These two uncertainties have been considered cell-to-cell correlated in the absolute efficiency computation. This procedure is caused by the lack of information about cell correlations and gives the most conservative approach in the analysis.

Combining both terms, the global correction coefficient for the absolute normalization of the neutrino flux is written

$$\langle c_{\varepsilon} \rangle = 0.9229 \pm 0.0093 \text{ (cell-to-cell corr.)} , \tag{5.21}$$

where the uncertainty takes into account any possible correlation between the previous mentioned Gd-fraction and IBD cut efficiency terms.

5.7 Summary and Conclusion

Along this chapter the first results of the neutron detection efficiency using the `MC GLG4sim` package have been presented. This package uses a dedicated model of the gamma emission from gadolinium excited states, and it has performed successfully for Phase I data analysis shown on the first publication of the STEREO experiment [1]. The energy spectra of the neutron captures have been presented in Fig. 5.1.2 for different regions of the detector using AmBe calibration `DATA` and `MC GLG4sim` simulations, displaying some tensions between them. Two of the main disagreements can be seen in the position of the gadolinium capture peak and its low energy tail in the [3, 5] MeV region. While the simulated peak is slightly shifted towards higher energies with respect to `DATA`, the simulated tail is not able to reproduce the observed distribution. Both effects are caused by an inaccurate implementation of the energy and multiplicity of the emitted gammas. An additional issue concerning the neutron mobility and capture cross section is observed through an under-representation of the amount of neutron captures in the hydrogen energy region in the simulation.

The neutron correction coefficients introduced in Section 4.1 are designed to quantify the level of disagreement between `DATA` and `MC`. In this chapter, the impact of the `GLG4sim` package in these coefficients has been shown for AmBe calibration `DATA` taken during the Phase I and Phase II. During the Phase I period of the STEREO experiment, the Gd-fraction and the IBD cut efficiency correction coefficients c_{Gd} and c_{IBD} have shown a relative agreement for the different cells and positions. Some discrepancies on the *top/bottom* region up to 1.0% and 1.3% have arisen for c_{Gd} and c_{IBD} respectively, and their study is limited by the few calibration data samples available for this period. Taking into account these features throughout the entire detector volume, a total correction coefficient of $c_{\varepsilon} = 0.944 \pm 0.016$ has been finally computed. This correction coefficient was implemented in the first oscillation analysis presented and published in Table. 2.3.1-(i).

Extra calibration positions have been introduced for the Phase II analysis, providing additional information concerning the observed border effects. Regarding the behavior of the c_{Gd}, two

features have been recognized. The first one is a *top/bottom* effect along z-axis caused by the gamma cascade implementation and the energy reconstruction. A second feature portrays a discrepancy between cells relative to their respective distance to the GC volume, as a consequence of the implementation of the neutron mobility and capture cross section in the MC. The spatial dependency of c_{Gd} has been described by the three dimensional HAND model, designed to reproduce the border effects using the combination of a normal and a parabolic distributions for the x, y, and for z axes respectively. The model is fed with information of the neutrino flux directionality and its interaction probability in the detector, provided by a MC simulation. With this method a set of independent c_{Gd} for each cell has been obtained.

Concerning the c_{IBD}, no significant border effects have been observed, and thus no specific model is required to account for them. Instead, a global coefficient has been calculated as the averaged value for all the positions. A total correction coefficient c_ε per cell has been computed as the product of these two terms c_{Gd} and c_{IBD}. The obtained results asymmetrically range between 0.9074 and 0.9311 along the detector, as a consequence of the directionality of the neutrino flux. An in-depth study of the systematic uncertainties completes the study of the correction coefficients for Phase II, taking into account time stability, energy reconstruction and source position biases, and spatial inhomogeneities. These studies can be summarized in two cell-to-cell terms, an uncorrelated one of 0.90% covering the entire volume, and a cell-dependent correlated term of up to 0.43%. The increased amount of data points and better understanding of the detector inhomogeneities with respect to Phase I can be inferred from these improved results. The $c_{\varepsilon,l}$ values for Phase II computed with the HAND model were used for the oscillation analysis performed in Table. 2.3.1-(ii), providing a significant improvement with respect to the computed value for Phase I.

Finally, an global correction coefficient term has been estimated for the prediction of the detected flux of neutrinos. From the computation of the oscillation analysis correction coefficients, a value of $\langle c_\varepsilon \rangle = 0.9229 \pm 0.0093$ has been obtained. This term comprises the border effects of both the $\langle c_{\mathrm{Gd}} \rangle$ and $\langle c_{\mathrm{IBD}} \rangle$, with a final cell-to-cell correlated uncertainty.

The correction coefficients obtained using a GLG4sim simulation have manifested inaccuracies in the neutron capture energy spectra, as a consequence of the gamma cascade modelization. The GLG4sim package was initially created to complement and extend the simulation of captures in gadolinium loaded LS. Nowadays, libraries using information from ENDF/B-VIII are able to recreate with better accuracy the emitted gamma cascade than GLG4sim. However, in small LS based experiments like STEREO these models are not capable to account for the escape of single gammas from the active volume. The STEREO experiment, in collaboration with CEA implemented the FIFRELIN code in the MC framework of STEREO [51], a model that uses experimental fission data to build the energy and multiplicity of the gamma cascade. In the next chapter the details of this model and its impact in both the neutron energy spectra and the efficiency values are shown.

Correction Coefficients for the Neutron Efficiency using FIFRELIN MC

Most of the DATA to MC discrepancies presented along the Chapter 5 have been proven to be directly linked with the modelization of the gamma cascade. One of the major improvements in the STEREO analysis has been the implementation of the FIFRELIN code on the MC simulation framework [51], and its impact in the neutron efficiency studies is presented along this chapter. In Section 6.1 an introduction to the model and its implications on the neutron energy spectra are shown. The updated neutron efficiency results for Phase I and Phase II are computed in Section 6.2. Together with these values, an improved systematic uncertainties analysis is presented in Section 6.3. The used correction coefficients in the STEREO analysis are summarized in Section 6.4, together with the revised values for the absolute normalization of the neutrino flux in Section 6.5. Finally, the impact of the FIFRELIN gamma cascade in the correction coefficients is reviewed in Section 6.6.

6.1 Simulated Gamma Cascade from Gd De-excitation using FIFRELIN

The FIFRELIN code [79] has been developed at CEA (Saint Paul Lez Durance, France) to accurately represent fission data, and its validity has been proven to predict neutron and gamma related observables. This code allows first to model the assignment of the initial states of the excited fission fragments, and then describes the de-excitation of these fragments. For the simulation framework of STEREO, only the de-excitation part is used, with the excited Gd states after a neutron capture as initial condition, thus mainly covering the description of the gamma multiplicities and energies in the de-excitation processes [51]. As it was highlighted in Chapter 3, when a thermal neutron is captured on ^{155}Gd and ^{157}Gd nuclei, the excited nucleus is at a resonance state S_n characterized by an energy E and spin parity J^{π}. Its transition to the GS proceeds mainly through γ emission. In FIFRELIN, once the initial state is given, a set of nuclear level schemes is sampled taking into account nuclear structure uncertainties. These energy level schemes are drawn in the following way [51]:

- $E \leq E^{RIPL}$: they are collected from the Reference Input Parameter Library (RIPL-3), and if a spin and/or a parity are missing, the code completes them using the theoretical momentum and parity distributions;

- $E^{RIPL} < E \leq E^{limit}$: only few levels are experimentally gathered, the rest are sampled in discrete levels computed theoretically (energy range defined until the level number matches the theoretical level density with E^{limit});

- $E > E^{limit}$: the energy region corresponds to the continuum with innumerable levels, therefore they are gathered in energy bins having a specific J^π given by the model.

This principle is illustrated in Fig. 6.1.1. The transition between these levels is performed using experimental knowledge and a theoretical nuclear model for the missing information. The theoretical nuclear level density $\rho(E, J^\pi)$ taken into account during a de-excitation step is computed as

$$\rho(E, J^\pi) = \rho_{tot}(E) \cdot P(J \mid E) \cdot P(\pi) , \qquad (6.1)$$

where $\rho_{tot}(E)$ corresponds to the total level density, $P(J \mid E)$ to the energy dependent angular distribution, and $P(\pi)$ the parity distribution. In FIFRELIN all the transition probabilities between an initial (i) and final (f) state (having both a given spin-parity J^π) emitting a particle p with given properties α, are computed in the following way

$$\Gamma_p(i \to f, \alpha) = \overline{\Gamma}_p(\epsilon_p, \alpha) \cdot \Pi_{i,f}(\alpha, J^{pi}) \cdot \rho(E_f, J_f^\pi) \, dE , \qquad (6.2)$$

where $\overline{\Gamma}_p(\epsilon_p, \alpha)$ is the averaged partial width of the transition energy ϵ_p; the $\Pi_{i,f}(\alpha, J^{pi})$ coefficient accounts for the spin and parity selection rules and the Porter-Thomas factor simulating the transition probabilty fluctuation [80]; and $\rho(E_f, J_f^\pi) \, dE$ is the number of levels in f. For a separation energy S_n, neutron emissions are unlikely, conversion electrons can occur and their transition probability is taken from the BrIcc code [81]. Gamma emissions are then computed using the average partial width

$$\overline{\Gamma}_\gamma(\epsilon_\gamma, XL) = \frac{\epsilon_\gamma^{2L+1} f_{XL}(\epsilon_\gamma)}{\rho(E_i, J_i^\pi)} . \qquad (6.3)$$

This width depends on the emitted gamma energy (ϵ_γ), its type X (electric or magnetic), its multipolarity L and the radiative strength function model ($f_{XL}(\epsilon_\gamma)$). Additional details about this FIFRELIN computation can be found in [51].

The de-excitation cascades from FIFRELIN have been directly implemented in the STEREO MC simulation, carrying three main discrepancies with respect to the `GLG4sim` package presented in
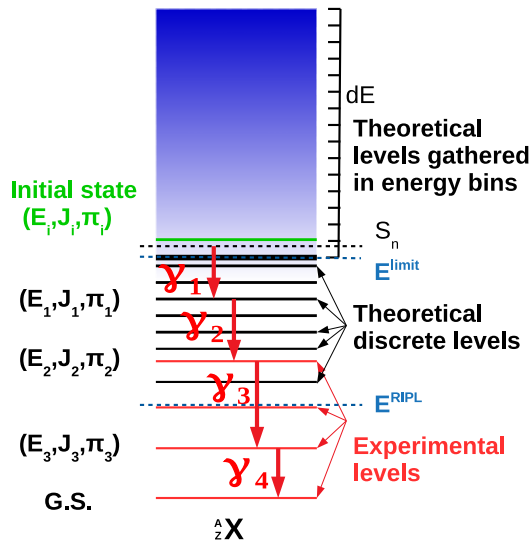
Figure 6.1.1: Sketch of the γ cascade implementation in FIFRELIN [51].

(a) Cascade gammas energy

(b) Cascade gammas multiplicity
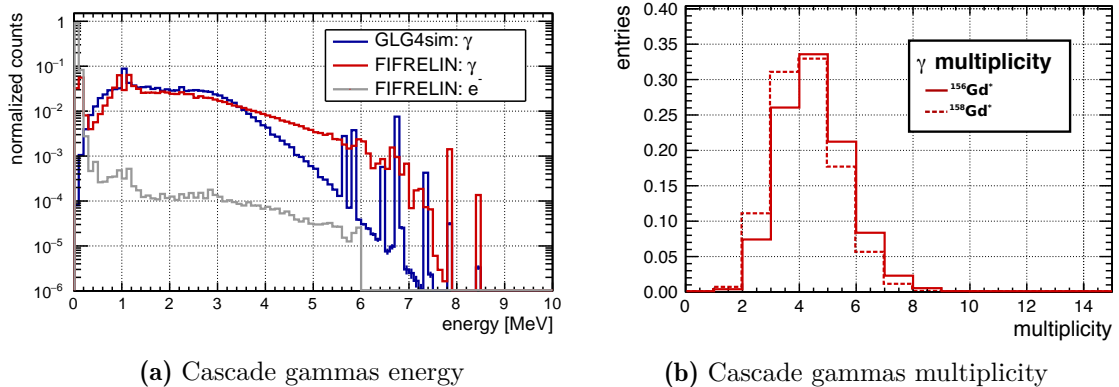
Figure 6.1.2: **(a)** Energy distribution of the gamma cascade and **(b)** gammas multiplicity using FIFRELIN package [51].

Chapter 5. First of all, the gamma multiplicity distributions for the two gadolinium isotopes shown in Fig. 6.1.2b are different than the already shown for `GLG4sim` in Fig. 5.1.1b. The averaged values of these distributions are summarized in Table 6.1.1, where a $\sim 4\%$ difference between cascade models can be seen. Secondly, in the energy distributions of single de-excitations presented in Fig. 6.1.2a, the FIFRELIN simulation has 15% more gammas above 3.5 MeV than the `GLG4sim` package. These high energy γs are needed for an accurate description of the cascade [51]. Finally, in the `GLG4sim` code, electrons are not taken into account. These particles contribute to about 70% of the cascades for the FIFRELIN code, with a most probable energy of 70 keV. The impact of these differences on the reconstructed energy spectra is shown in the next subsection.

6.1.1 Reconstructed Energy Distribution after a Neutron Capture

In Fig. 6.1.3 the energy spectra of AmBe events from `DATA` and a `MC` simulation using the FIFRELIN gamma cascade (red) are represented. For comparison, the already shown distributions using `GLG4sim` (blue) from the previous chapter are included. The distributions show three different heights for the source in `Cell 1` and `Cell 4` that allow to see the impact of the FIFRELIN gamma cascade on the homogeneity of the response.

The `GLG4sim` package has presented some tensions on the gadolinium capture peak and its low energy tail along the [3, 5] MeV. With the implementation of FIFRELIN, the `MC` simulation matches the behavior of `DATA` and both issues are no longer observed. First of all, a less steep tail next connecting both capture peaks is observed, with an extension to the hydrogen capture region. Secondly, an agreement on the sub-percent level is achieved on the gadolinium mean peak position. All of these improvements are observed for central positions like `Cell 4 - 45 cm`,

Table 6.1.1: Multiplicity of the gamma emission when a neutron capture occurs in one of the gadolinium isotopes using the FIFRELIN[51]. `GLG4sim` values are also represented, taken from Table 5.1.1.

Gd isotope	`GLG4sim` γ **multiciplity**	FIFRELIN γ **multiciplity**
155	4.271 ± 0.001	4.058 ± 0.001
157	3.968 ± 0.001	3.778 ± 0.001
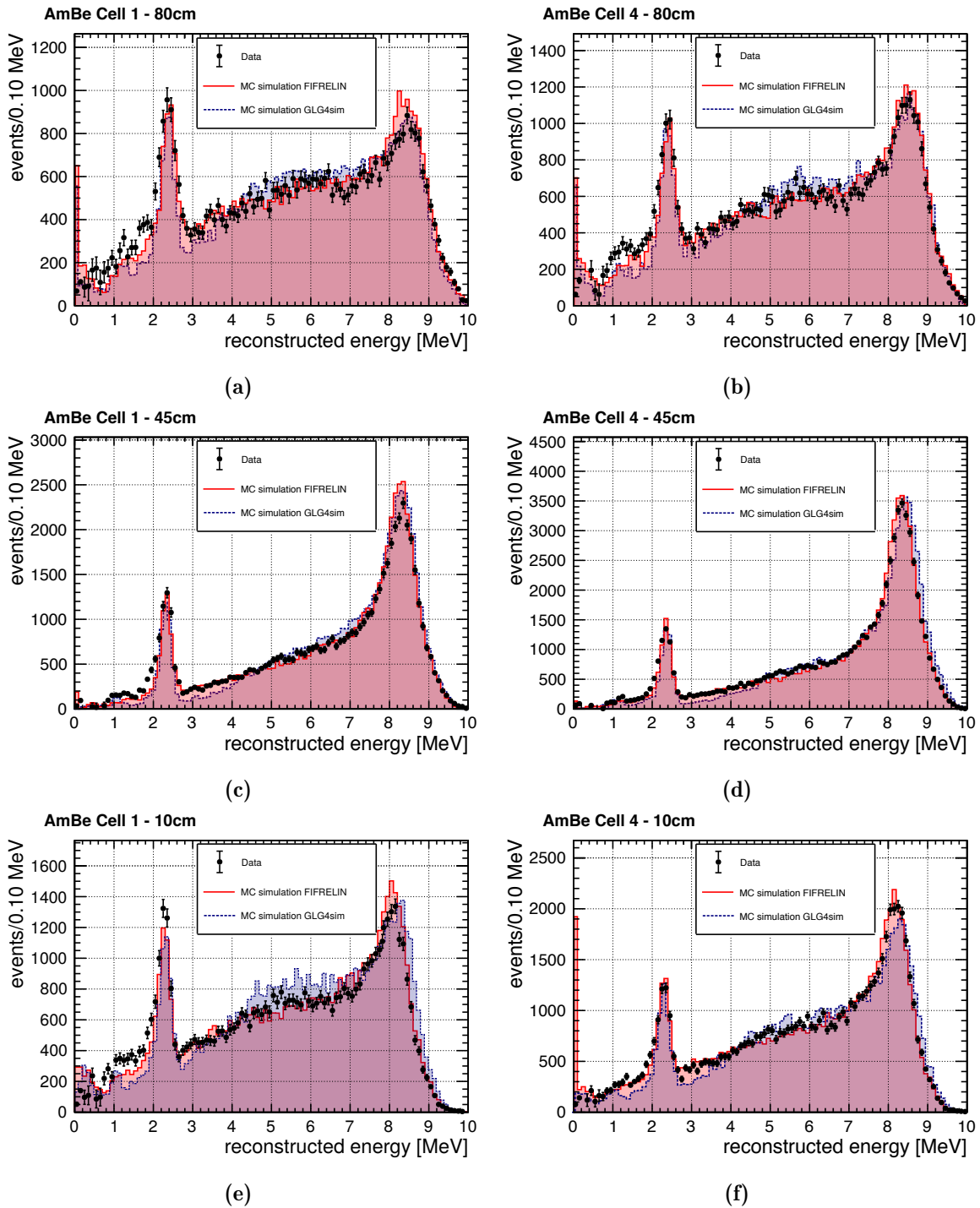
Figure 6.1.3: Reconstructed energy distributions after a neutron capture for DATA and MC simulations, using the AmBe source different heights of `Cell 1` and `Cell 4`. DATA samples are the ones from the `20180619`. MC Simulation distributions are scaled to the DATA ones. Uncertainties are only statistical. To avoid energy reconstruction issues, the `GLG4sim` MC distributions are scaled to the position of the hydrogen peak in the MC simulation with Fifrelin.

as well as on the border regions of the detector like `Cell 4 - 10 cm`. In contrast, border positions as the ones for `Cell 1` still show a lower amount of hydrogen captures in the MC simulation. The already mentioned inaccuracies of the neutron mobility and/or capture cross section are still present on this updated simulation.

All in all, the FIFRELIN gamma cascades improve the description of gammas from the Gd cascade in the MC simulation. Along this chapter the impact of this updated gamma cascade on the neutron efficiency values is studied. In the next section the values for Phase I and Phase II are shown, together with their impact on the systematic uncertainties estimation.

6.2 Correction Coefficients in **Phase I** and **Phase II**

The implementation of FIFRELIN in the MC simulation has caused an impact on the reconstructed energy spectra, and in the IBD selection. The reevaluation of the correction coefficients for the neutron detection efficiency has helped to quantify the improvement of the simulation in the STEREO experiment [51]. In contrast to how it was presented in Chapter 5, DATA from Phase I and Phase II runs are analyzed simultaneously, and the obtained values of c_{Gd} and c_{IBD} are presented in the following subsections.

6.2.1 Gd-fraction Efficiency

The obtained c_{Gd} using FIFRELIN are presented for all of the calibration dates in Fig. 6.2.1. The values for Phase I present a small decrease of $\sim 1\%$ in terms of time. This trend has been already presented for the `GLG4sim` simulation in Fig. 5.2.2, but in this case a better agreement is observed between phases. Proceeding with the same type of analysis than in the previous chapter, the averaged values over all times for each position and phase have been summarized in Table 6.2.1 and represented in Fig. 6.2.2. Comparing these values with the `GLG4sim` ones summarized in Table 5.3.1, a significant improvement of the correction factors is observed in the center areas of the detector being enhanced up to a 1.6%, with a discrepancy of less than 0.5% from 1. Lower values are still observed on border cells, but the relative discrepancy of 3.1% has been reduced to 2.2%. The updated gamma cascade described in Section 6.1 have helped to improve the shape of the correction coefficients along the `z-axis`.

The uncertainties represented in Fig. 6.2.2 correspond to the standard deviation between the different calibration dates. Phase II counts with a large amount of calibration runs and thus the uncertainty is smaller than for Phase I, as discussed in Chapter 5. In Table 6.2.2 the absolute discrepancies between phases are summarized for the available calibration positions of Phase I. Discrepancies between periods are within 2σ of the statistical fluctuation of Phase I. Only for `Cell 1 – 80 cm` a significant variation can be observed, reaching a deviation up to 3σ. Since the Phase I data taking period has less information from the center positions of the detector (`Cell 2` and `Cell 5`), an analysis only using these data points would overweight the border effects in a global detector correction coefficient. Due to the observed agreement between phases, the obtained correction coefficients from Phase II are used in the analysis of both phases.

The correction coefficients obtained using FIFRELIN for Phase II have been analyzed in a similar way to the procedure applied in Chapter 5 using `GLG4sim`. To compute a global correction coefficient for each cell, a MC neutrino flux is used together with the `HAND` model from Section 5.3.1, implemented on the different cells along the detector. However, the FIFRELIN efficiency results do not present a *top/bottom* effect along the `z-axis` as the one observed for `GLG4sim`. Improve-
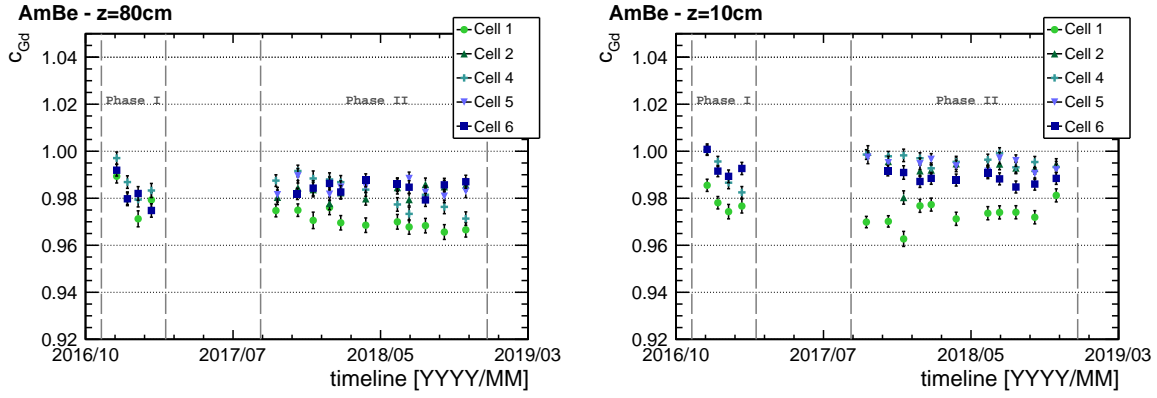
(a) AmBe - 80 cm

(b) AmBe - 10 cm
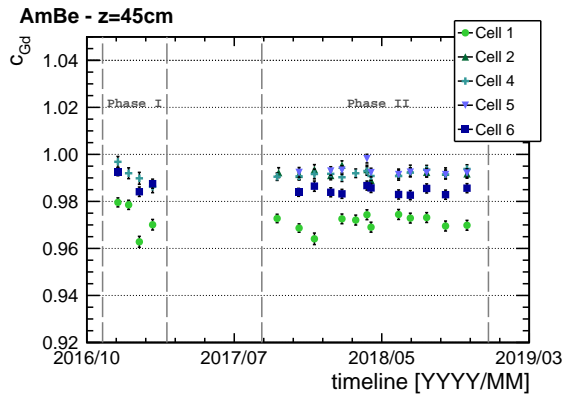
(c) AmBe - 45 cm
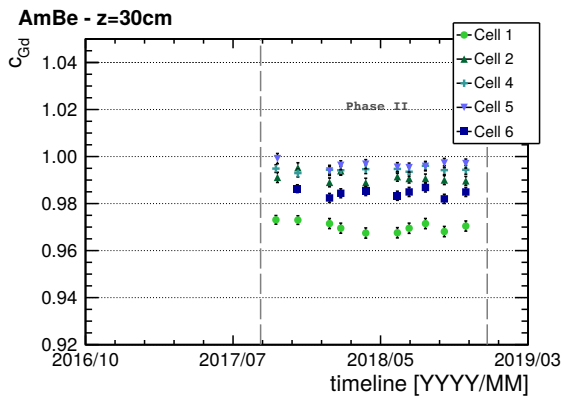
(d) AmBe - 30 cm
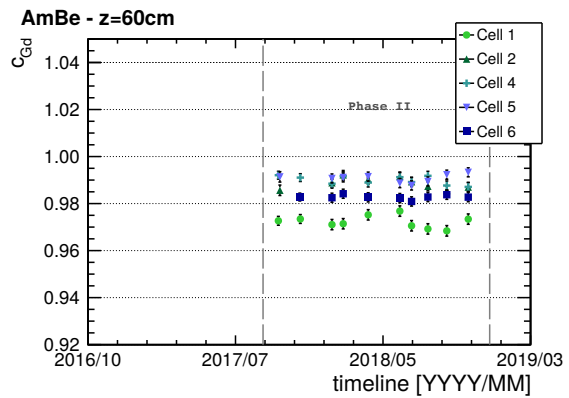
(e) AmBe - 60 cm

Figure 6.2.1: Time stability of the c_{Gd} using the FIFRELIN package in the MC simulation. Uncertainties are obtained for each ratio (Eq. B.7) considering the statistical fluctuation from Eq. 4.13.

Table 6.2.1: c_{Gd} values for Phase I and Phase II using FIFRELIN. Uncertainties are the standard deviation (see Eq. B.2) of the data values from Fig. 6.2.1.

Gd-fraction Position	Phase I Cell 1	Cell 2	Cell 4	Cell 5	Cell 6	Phase II Cell 1	Cell 2	Cell 4	Cell 5	Cell 6
top 80 cm	0.9791 ± 0.0005	–	0.9847 ± 0.0026	–	0.9829 ± 0.0049	0.9698 ± 0.0010	0.9826 ± 0.0008	0.9818 ± 0.0008	0.9843 ± 0.0006	0.9845 ± 0.0003
top-center 60 cm	–	–	–	–	–	0.9722 ± 0.0010	0.9886 ± 0.0008	0.9897 ± 0.0006	0.9907 ± 0.0006	0.9827 ± 0.0003
center 45 cm	0.9735 ± 0.0026	–	0.9905 ± 0.0007	–	0.9881 ± 0.0025	0.9709 ± 0.0009	0.9923 ± 0.0005	0.9918 ± 0.0003	0.9929 ± 0.0003	0.9845 ± 0.0005
center-bottom 30 cm	–	–	–	–	–	0.9698 ± 0.0006	0.9911 ± 0.0007	0.9943 ± 0.0005	0.9963 ± 0.0005	0.9845 ± 0.0006
bottom 10 cm	0.9758 ± 0.0017	–	0.9924 ± 0.0029	–	0.9942 ± 0.0034	0.9733 ± 0.0016	0.9929 ± 0.0014	0.9959 ± 0.0007	0.9945 ± 0.0008	0.9884 ± 0.0007

Table 6.2.2: Absolute discrepancy of the c_{Gd} between phases, relative to averaged value. Values are taken from Table 6.3.1.

Position	Cell 1	Cell 4	Cell 6
top	1.02%	0.45%	0.24%
center	0.19%	0.06%	0.37%
bottom	0.54%	0.47%	0.52%

99
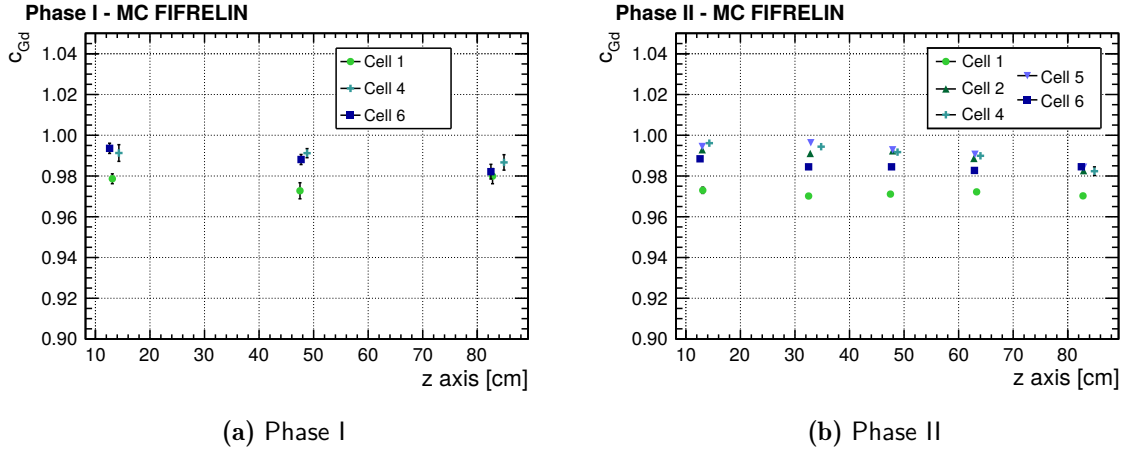
Figure 6.2.2: Homogeneity of the c_{Gd} using FIFRELIN for **(a)** Phase I and **(b)** Phase II. Values are from Table 6.2.1. Uncertainties are obtained statistically using the standard deviation.

ments on the energy reconstruction, together with the implementation of the FIFRELIN gamma cascade, have created an homogeneous correction coefficient at the different heights of a cells. Therefore, this direction is not considered in the modelization of the correction coefficients. This updated version of the HAND model, named BAND from now on (Border Algorithm of the Neutron Detection), is described in the following subsections together with its implementation on a MC neutrino flux.

Step 1 - the BAND model

The correction coefficient obtained using FIFRELIN have been studied using a 2 dimensional model of the $c_{Gd}(x, y)$ that depends on the position of the neutron creation in the (x,y) plane:

$$c_{Gd}^{BAND}(x, y) = L(x) \cdot W(y) . \tag{6.4}$$

Since the same border effect is expected than using the GLG4sim γ cascade, the same functions $L(x)$ and $W(x)$ are used, Eq. 5.5 and Eq. 5.10 respectively. In these calculations, an averaged $\bar{c}_{Gd}$ value for each cell is computed using the 5 different heights:

$$\begin{aligned}
\bar{c}_{Gd,1} &= 0.9712 \pm 0.0012 , \\
\bar{c}_{Gd,2} &= 0.990 \pm 0.003 , \\
\bar{c}_{Gd,4} &= 0.992 \pm 0.002 , \\
\bar{c}_{Gd,5} &= 0.991 \pm 0.003 , \\
\bar{c}_{Gd,6} &= 0.986 \pm 0.003 .
\end{aligned} \tag{6.5}$$

In the following paragraphs, the contribution in the x- and y-axis is described.

As described in Chapter 5, the study of the x-axis depends on the independent treatment of cell-wise deployments of the calibration source. The averaged correction coefficients per cell are represented in Fig. 6.2.3a, with respect to the position of the calibration tubes. As it can be seen, the same flat behavior observed in the center cells Cell 2, 4 and 5 as with GLG4sim values is still present, while in the the border cells a drop in the efficiency is shown. The values are fitted to the *Generalized normal distribution $L(x)$* described in Eq. 5.5. The obtained fit distribution

(a) $L(x)$ function

(b) $W(y)$ function
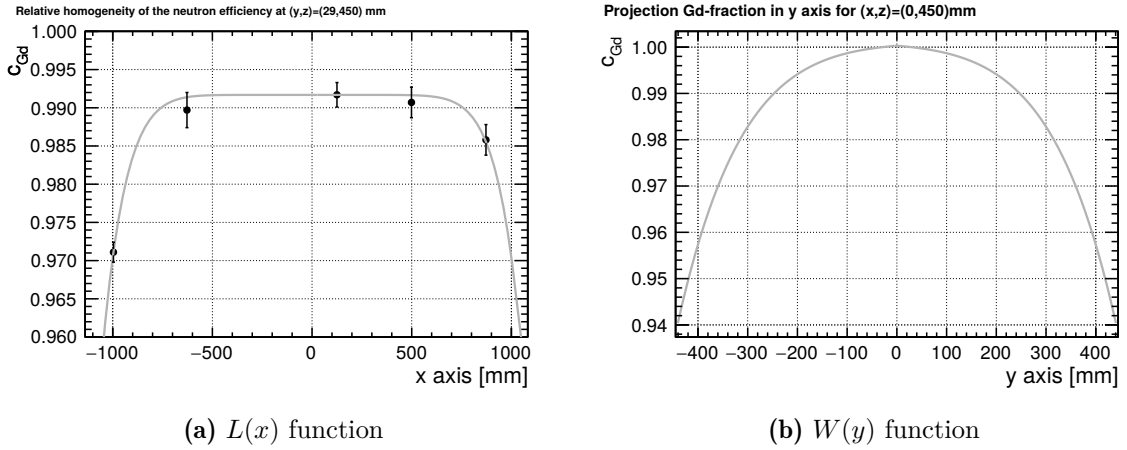
Figure 6.2.3: (a) Relative homogeneity and fitted distribution of the c_{Gd} along the x-axis, for $(y, z) = (29\,\text{mm}, 450\,\text{mm})$. Values are the averaged terms in each cell from Eq. 6.5, and the uncertainties correspond to their standard deviation. **(b)** Used distribution of the c_{Gd} along the y-axis for all the cells.

for the FIFRELIN values is represented in Fig. 6.2.3a for $\mu_x \equiv 0$. With a $\chi^2/ndf = 0.89$, the results of the fit are,

$$\sigma_x^{\text{B}} = (1520 \pm 70)\ \text{mm} ,$$
$$\beta_x^{\text{B}} = 9.2 \pm 0.9 .$$

$$(6.6)$$

The border effects in the y-axis are expected to be the same as for the x-axis since the transition to the GCLong volumes is topologically equivalent to the short ones. Such premise is necessary to cover the lack of information on the y-axis obtained from the AmBe calibration. Therefore, the $W(y)$ function is extrapolated from the $L(x)$ as described in Eq. 5.10. The parameters μ_x^{B} and σ_x^{B} obtained from Eq. 6.6 are used together with the length difference of the NT volume along the x-axis and the y-axis. To make $c_{\text{Gd}}(x, y)$ converge to the observed results, the $W(y)$ function is scaled to 1. The shape of this extrapolation considering the previous pa-

(a) $L(x)$ comparision

(b) $W(y)$ comparision
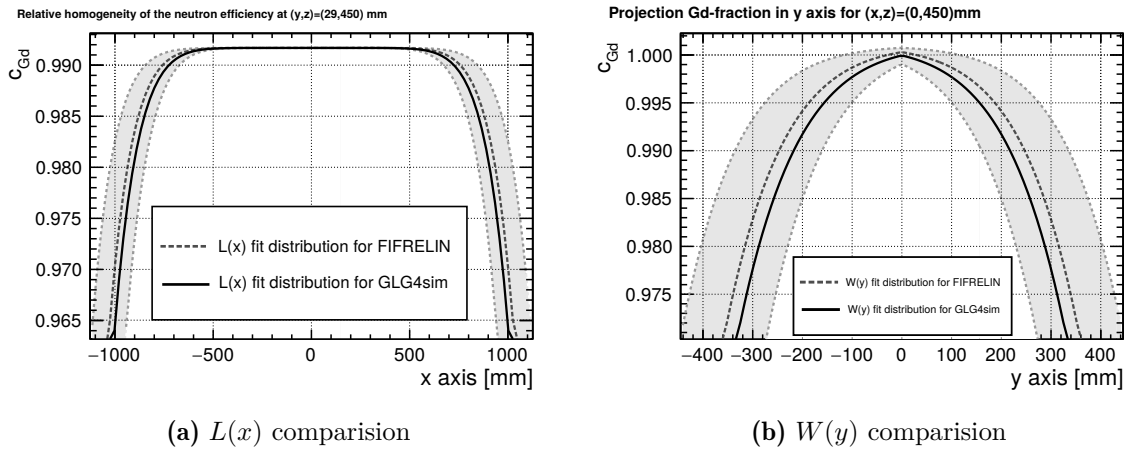
Figure 6.2.4: Comparison between the obtained fit functions for FIFRELIN (gray line and error band) and GLG4sim (black line) for the **(a)** $L(x)$ and **(b)** $W(y)$ functions.
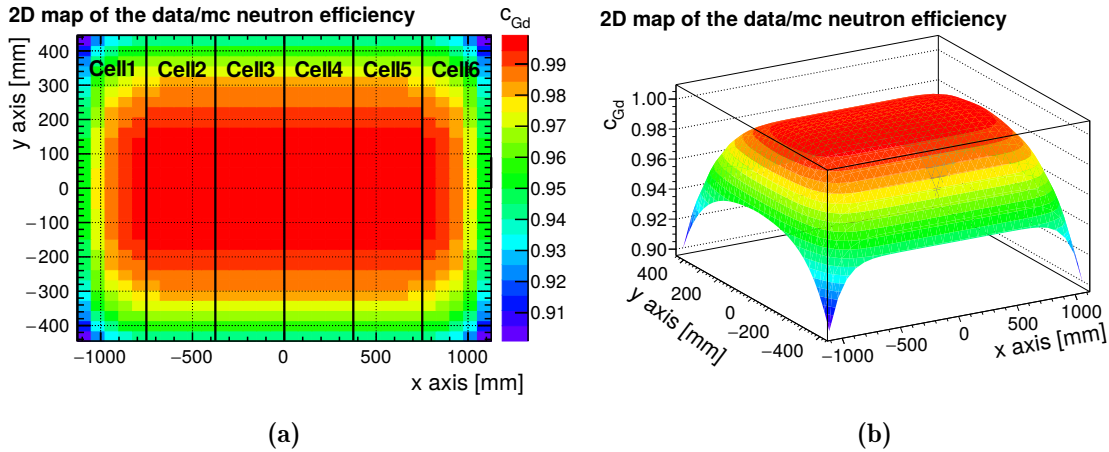
Figure 6.2.5: Distribution of the $c_{Gd}(x,y)$ along the NT volume.

rameters and the size of the detector is represented in Fig. 6.2.3b.

Comparing the obtained fit parameters with `GLG4sim` and Fifrelin, compatible fit parameters for $L(x)$ and $W(y)$ functions are observed. The obtained functions along the `xy-plane` are represented in Fig. 6.2.4, together with the extrapolation of the fit uncertainty in σ_x^B and β_x^B. The fit functions of the `HAND` model have been normalized to the `BAND` ones to do a relative comparison. Both shapes show a notable agreement with each other. This proves that the same border effects are observed for both `GLG4sim` and Fifrelin gamma cascade models, and that is dependent on external simulation inaccuracies as neutron mobility or capture cross section.

The `BAND` model can be represented on the `xy-plane` in Fig. 6.2.5. Since the same correction coefficients are applied homogeneously along the `z-axis`, this figure represents how the $c_{Gd}^{BAND}(x,y)$ would be evaluated at any position of the detector. $c_{Gd}^{BAND}(x,y)$ reproduces successfully the border effects of `Cell 1` and `Cell 6`, and the global behavior in the center cells.

Step 2 - Reactor neutrino flux

Once the $c_{Gd}^{BAND}(x,y)$ function is created, a correction coefficient for each cell can be computed. A neutrino `MC` simulation is used to obtain the position (x_j, y_j, z_j) where a neutron j is created. In this way, the location of the Stereo detector is taken into account (which is not oriented parallel to the radial direction of the reactor). This `MC` simulation is composed by nearly 1 million of events around the `NT` where the Fifrelin gamma cascade has been included. The neutron creation position (x_j, y_j, z_j) is used to evaluate the Eq. 5.4 for the $c_{Gd,l}$ estimation. The obtained correction coefficients in each cell using the $c_{Gd}^{BAND}(x,y)$ function are summarized in Table 6.2.3. Due to the directionality of the neutrinos, an asymmetric behavior of the correction coefficients is observed along the detector volume. With the Fifrelin simulation, values closer to 1 are observed along the detector. For `Cell 1` and `Cell 6` a similar value around ~ 0.965 is obtained after the border effects consideration. Besides this consideration and accounting for border effects, this methods also extrapolates the response of `Cell 3` from the neighbor cells. In the same fashion as in Chapter 5, the uncertainties of the correction coefficients are computed later in Section 6.3. These numbers and the ones obtained with `GLG4sim` are reviewed in Section 6.6.

Table 6.2.3: $c_{\mathrm{Gd},l}$ values for Phase II using FIFRELIN after the implementation of the BAND model and the neutrino flux directionality. Uncertainties are described and summarized in Section 6.3.

	Cell 1	Cell 2	Cell 3	Cell 4	Cell 5	Cell 6	NT
n events	192,012	174,537	161,942	151,082	140,923	136,136	919,949
corrected n events	185,348	171,829	159,474	148,780	138,741	131,513	919,949
$c_{\mathrm{Gd},l}$	0.9650	0.9843	0.9846	0.9846	0.9844	0.9657	0.9789

6.2.2 IBD Cut Efficiency

The obtained c_{IBD} values using the FIFRELIN simulation are represented in Fig. 6.2.6 for all of the calibration dates. The correction coefficients for Phase I present up to a $\sim 1\%$ decrease over time in the same way as for the c_{Gd}. For the second period of data taking, values for all of the positions slightly fluctuate around one. The averaged values are independently estimated for each phase, and are summarized in Table 6.2.4. There, statistical fluctuations are represented by the standard deviation of all the dates. The same correction coefficients are represented in the homogeneity plots of Fig. 6.2.7. FIFRELIN presents a significant improvement in terms of c_{IBD} showing a global increase of 2% in the $^{\mathrm{DATA}}/_{\mathrm{MC}}$ ratios. Such increase is a direct consequence of the improvement in the reconstructed Gd peak seen in Fig. 6.1.3. This efficiency term is sensitive to changes in the energy range between [3, 4.5] MeV, and therefore to the full energy deposition peak and its tail. Comparing the different parts of the detector, some disparity is observed between Cell 1 and the rest of the NT. This effect is mostly enhanced at the *top* region, where a discrepancy of 1.47% from $c_{\mathrm{IBD}} = 1$ is observed.

Discrepancies between calibration phases are seen through Table 6.2.5, where an agreement within 2σ is reached at the different positions with the exception of Cell 4 − 10 cm. A maximal discrepancy of 1.5% is observed, where this value is significantly below the others during Phase I. As explained in Chapter 2, several effects concerning the detector response of this cell were encountered during Phase I and could be the source of disagreement.

From these results two conclusions can be drawn. First, the computed values from Phase I are missing information about the central positions of the detector, but they statistically agree with the obtained ones for Phase II. Consequently, the obtained values from Phase II are the ones used for the global computation of the c_{IBD}. Second, the correction coefficients present minor discrepancies between cells (below $\sim 1\%$), allowing the computation of a global correction coefficient for the entire detector. This estimation is performed in the same way as for GLG4sim. The averaged value for the entire detector taking into account the 25 calibration positions is

$$c_{\mathrm{IBD}} = 0.9985 \pm 0.0051 \ . \tag{6.7}$$

This global c_{IBD} is 2% higher than the one obtained with GLG4sim (Eq. 5.11), and compatible with 1 within 1σ. Besides, due to the good agreement between the different cells and positions its uncertainty is lower than the one obtained with the old simulation. In the next subsections a similar systematic study as in Section 5.4 will be performed for both c_{Gd} and c_{IBD}, and the total correction coefficients will be computed accordingly.
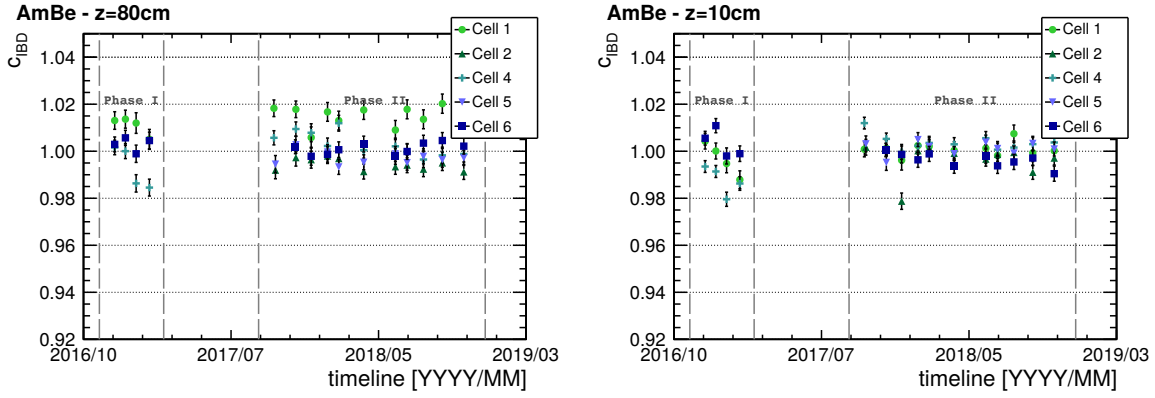
(a) AmBe - 80 cm

(b) AmBe - 10 cm
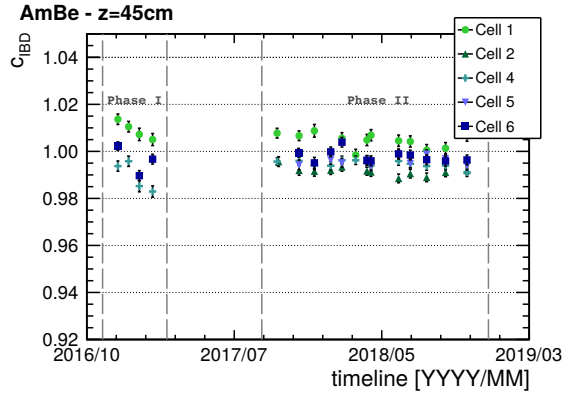
(c) AmBe - 45 cm
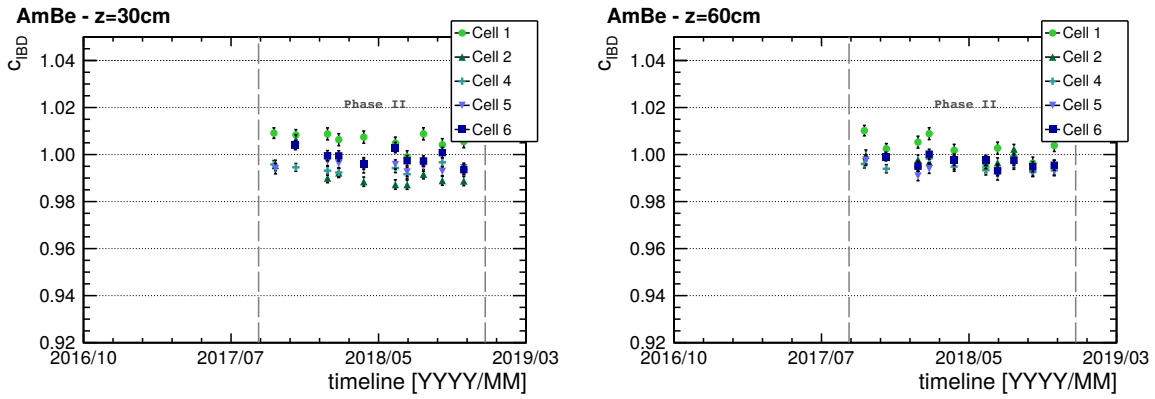
(d) AmBe - 30 cm

(e) AmBe - 60 cm

Figure 6.2.6: Time stability of the c_{IBD} using the FIFRELIN package in the MC simulation. Uncertainties are obtained for each ratio (Eq. B.7) considering the statistical fluctuation from Eq. 4.13.

Table 6.2.4: c_{BD} values for Phase I and Phase II using FIFRELIN. Uncertainties are the standard deviation (see Eq. B.2) of the data values from Fig. 6.2.6.

IBD cut eff. Position	Phase I					Phase II				
	Cell 1	Cell 2	Cell 4	Cell 5	Cell 6	Cell 1	Cell 2	Cell 4	Cell 5	Cell 6
top 80 cm	1.0110 ± 0.0019	—	0.9931 ± 0.0045	—	1.0030 ± 0.0015	1.0147 ± 0.0014	0.9943 ± 0.0007	1.0027 ± 0.0016	0.9971 ± 0.0009	1.0010 ± 0.0008
top-center 60 cm	—	—	—	—	—	1.0017 ± 0.0015	0.9975 ± 0.0008	0.9946 ± 0.0006	0.9941 ± 0.0008	0.9967 ± 0.0008
center 45 cm	1.0091 ± 0.0019	—	0.9894 ± 0.0031	—	0.9962 ± 0.0036	1.0044 ± 0.0009	0.9915 ± 0.0005	0.9946 ± 0.0004	0.9959 ± 0.0006	0.9979 ± 0.0008
center-bottom 30 cm	—	—	—	—	—	1.0059 ± 0.0010	0.9916 ± 0.0018	0.9944 ± 0.0007	0.9947 ± 0.0005	0.9989 ± 0.0011
bottom 10 cm	0.9967 ± 0.0035	—	0.9877 ± 0.0031	—	1.0033 ± 0.0031	1.0009 ± 0.0009	0.9968 ± 0.0020	1.0028 ± 0.0006	1.0013 ± 0.0009	0.9963 ± 0.0010

Table 6.2.5: Absolute discrepancy of the c_{BD} coefficients obtained between phases, relative to averaged value. Correction coefficients taken from Table 6.2.4.

Position	Cell 1	Cell 4	Cell 6
top	0.37%	0.96%	0.20%
center	0.47%	0.56%	0.17%
bottom	0.42%	1.52%	0.70%
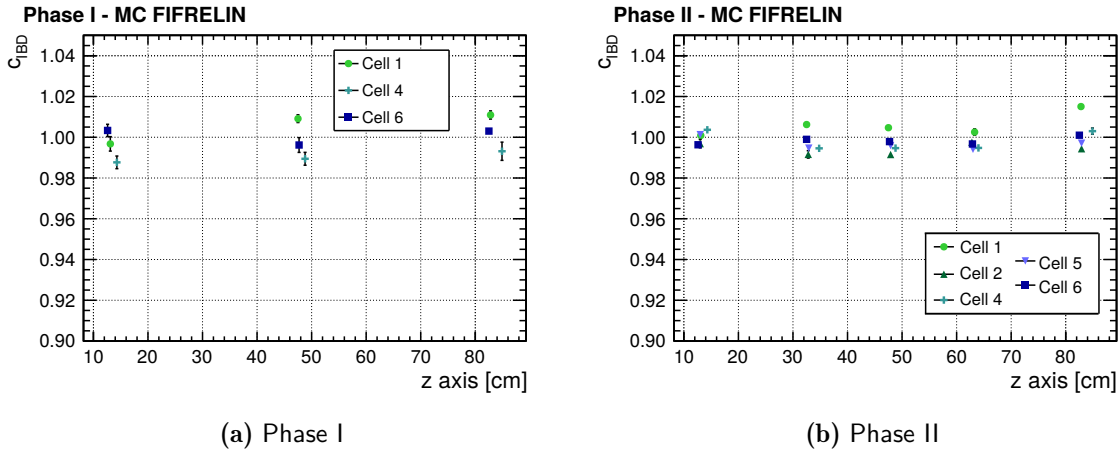
(a) Phase I

(b) Phase II

Figure 6.2.7: Homogeneity of the c_{IBD} using FIFRELIN for **(a)** Phase I and **(b)** Phase II. Values are from Table 6.2.4. Uncertainties are obtained statistically using the standard deviation.

6.3 Systematic Uncertainties

Following the study of systematic uncertainties in Chapter 5, a similar analysis has been performed for c_{Gd} and c_{IBD} obtained from FIFRELIN simulations. Several sources of error like the time stability, position bias of the calibration source, or the homogeneity model described in Section 6.2.1 are also going to be taken into account for the current analysis. However, contrarily to what has been done for `GLG4sim` simulations, the impact of an energy reconstruction bias is not considered as part of the systematic sources for FIFRELIN. The implementation of the FIFRELIN gamma cascade in the MC was accompanied by a crucial improvement in the MC light collection, causing an impact in the energy reconstruction algorithm. Consequently, the remaining systematics from a possible energy bias are therefore assumed negligible. The rest of the systematic sources already mentioned are developed in the following subsections. The final results of the correction coefficient summarized together with their correspondent uncertainty are shown in Section 6.4.

6.3.1 Time Stability

For the correction coefficients a systematic term concerning the time variation is taken into account. This term contains information of the statistical fluctuation and other external effects affecting distinctly the different calibration runs and it is described by the standard deviation of all of the available calibration dates. The obtained values in Table 6.2.1 and Table 6.2.4 represent the time fluctuations observed in Fig. 6.2.1 and Fig. 6.2.6. A $\sim 0.10\%$ statistical fluctuation can be observed for both c_{Gd} and c_{IBD} terms independently to each calibration position. Therefore, similarly to the `GLG4sim` analysis, a 0.10% cell-to-cell uncorrelated uncertainty is considered for both efficiency terms.

6.3.2 Source Position Bias

Another term considered in the total systematic uncertainty is the contribution of a bias in the source position between the DATA samples and the MC simulation. An extensively study was performed with the `GLG4sim` simulation in Section 5.4, where the impact of a systematic shift of +1 cm in several positions along the calibration tube of `Cell 4` was applied. The obtained results for the different configurations were summarized in Table 5.4.2, where the source position

bias was affecting both efficiency terms in the same direction. An averaged absolute error of 0.22% and 0.27% was obtained for c_{Gd} and c_{IBD} respectively, with a full correlation between the efficiency terms. A source position bias would equally affect the correction coefficients in both MC models. Therefore, the values obtained by using the GLG4sim simulation are also used as part of the FIFRELIN systematic contribution for the source position bias.

6.3.3 Inhomogeneity Model - Gd-fraction Efficiency

Lastly, the spatial homogeneity of the correction coefficients is also going to be included as a systematic term. In this subsection the impact of the spatial inhomogeneities of the BAND model are studied, for both a **cell-to-cell uncorrelated** and the **cell-to-cell correlated** systematic uncertainties. These two values are covering possible systematic effects in the treatment of the c_{Gd}.

Cell-to-cell Uncorrelated Systematic Uncertainty: This term is computed in the same way as for the GLG4sim model. The obtained c_{Gd} values from the AmBe calibration runs are summarized in Table 6.2.1, and they are compared with the evaluation of the $c_{Gd}(x,y)$ BAND model at the position that the source is deployed. There, the discrepancy term $\Delta_{l,z}$ is represented. This term for a Cell l and the source placed at a z position was already introduced as,

$$\Delta_{l,z} = c_{Gd}\Big|_{\text{Table 6.2.1}} - c_{Gd}(x_l, y_l) \ . \tag{6.8}$$

The discrepancies for each position of the detector are represented in Fig. 6.3.1. Central areas show a good agreement with 0, while at the *bottom* positions a $\Delta \sim 0.25\%$ is observed. The *top* position is the one with higher discrepancies for some of the cells. Assuming that $\Delta_{l,z}$ distributes normally around 0, the highest discrepancy would be within the 2σ range at a 90% confidence level. Accordingly, the discrepancies are interpreted as the systematic uncertainty of the $c_{Gd}(x,y)$ model

$$\Delta_{l,z}\Big|_{max} = 0.98\% \equiv 2\sigma \Rightarrow \sigma = 0.49\% \ . \tag{6.9}$$

(a) $\Delta_{l,z}$ values for each cell and position.

(b) Δ_l distribution
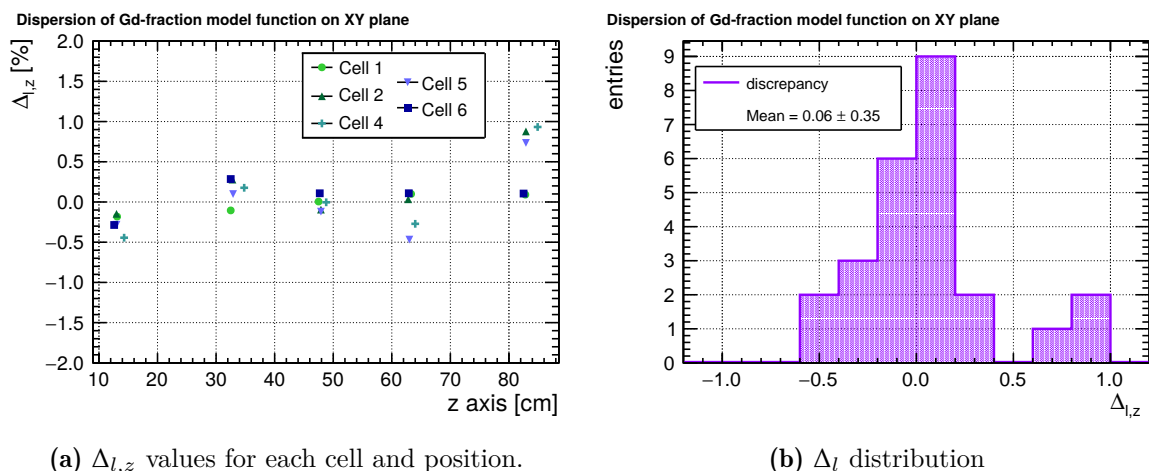
Figure 6.3.1: Obtained Δ_i values using the Eq. 6.8, with the initial values from Table 6.2.1 and the BAND model for FIFRELIN.

(a) $L(x)$

(b) $W(y)$
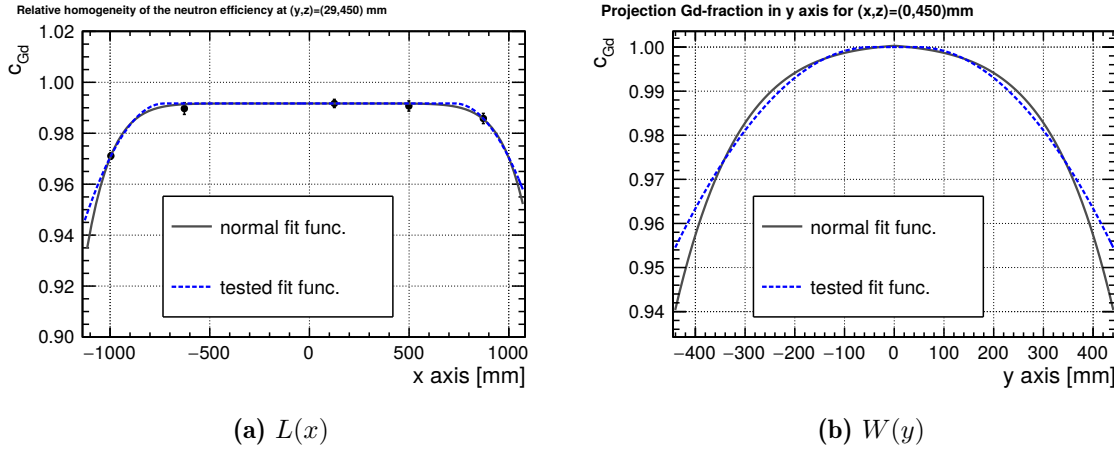
Figure 6.3.2: Shape of the $L(x)$ and $W(y)$ functions using the BAND model and the TEST function from Eq. 5.15.

The obtained value of 0.49% from the FIFRELIN results provides a conservative approach of the cell-to-cell uncorrelated systematic uncertainty, covering all possible systematic effects of the data treatment as a fluctuation between the model and the initial parameters. Uncertainties coming from the model itself will be described in the following paragraph.

Cell-to-cell Correlated Systematic Uncertainty: This term evaluates the impact of choosing a specific function to fit the obtained values for the different cells. In the previous chapter, a **TEST function** was defined in Eq. 5.15 to test the reliability of the function $L(x)$ in two different areas: at the borders of the central plateau, and at the extremes of the function. This function defined by parts depends on three parameters: a_T and b_T which describe the shape of the parabolic distributions, and the position *pos* where the flat contribution begins and finishes. This simple approach represented in Fig. 6.3.2a is able to reproduce the correction coefficients with the same level of agreement than the BAND function. The obtained parameters satisfaying the values from Table 6.2.1 are

$$a_\mathsf{T} = (2.90 \pm 0.12) \cdot 10^{-7} \text{ mm}^{-2} \;,$$
$$b_\mathsf{T} = (4.1775 \pm 0.0009) \cdot 10^{-7} \text{ mm}^{-1} \;, \tag{6.10}$$
$$pos = 729 \pm 165 \text{mm} \;.$$

Since the definition of $W(y)$ is inherently attached to $L(x)$, it also needs to be substituted by $W_\mathsf{TEST}(y)$ in the final construction of $c_\mathrm{Gd}^\mathsf{TEST}(x,y)$,

$$c_\mathrm{Gd}^\mathsf{TEST}(x,y) = L_\mathsf{TEST}(x) \cdot W_\mathsf{TEST}(y) \;. \tag{6.11}$$

The shape of the TEST function on the y-axis is also represented in Fig. 6.3.2b. The impact of the endpoint parametrization of the BAND model when determining the correlated uncertainties can be studied by means of this function. More specifically, Eq. 6.11 has been used to reevaluate the correction coefficients in each cell and in the NT volume using a reactor neutrino simulation, as performed in Section 6.2.1. The obtained values are summarized in Table 6.3.1, in addition to the already computed values using the BAND function and their discrepancy. Comparing both correction coefficients, the center cells differ by less than $\sim 0.15\%$, since they are only affected by

Table 6.3.1: c_{Gd} values for each cell l after the implementation of the TEST model in a neutrino MC simulation. Values are compared to the ones obtained with the BAND model in Table 6.2.3. The absolute discrepancy between both models is considered as the cell-to-cell correlated uncertainty.

	Cell 1	Cell 2	Cell 3	Cell 4	Cell 5	Cell 6	NT
$c_{\mathrm{Gd},l}^{\mathrm{TEST}}$	0.9691	0.9859	0.9859	0.9859	0.9859	0.9697	0.9809
$c_{\mathrm{Gd},l}^{\mathrm{BAND}}$	0.9650	0.9843	0.9846	0.9846	0.9844	0.9657	0.9789
abs. discrep. [%]	0.41	0.15	0.13	0.13	0.15	0.40	0.20

the component on the y-axis. On the contrary, the border regions covered by Cell 1 or Cell 6 present $\sim 0.4\%$ variation, due to the already mentioned differences between both functions. The impact of the use of the TEST function is considered again as the systematic uncertainty of the model, being this conservative approach picturing a cell-to-cell correlated error up to 0.40%.

6.3.4 Homogeneity Model - IBD Cut Efficiency

Since no homogeneity model has been used to describe the c_{IBD} correction coefficients, the obtained mean error of the different cells and positions along the detector is considered. The uncertainty presented in Eq. 6.7 (0.51% uncertainty) covers any possible inhomogeneity of the detector, and it is considered as the systematic uncertainty of the c_{IBD}.

6.3.5 Summary of the Uncorrelated Systematic Uncertainties

The cell-to-cell uncorrelated systematic uncertainties obtained in the previous paragraphs are summarized in Table 6.3.2. In this analysis, the c_{Gd} presents an 0.57% uncertainty dominated by the discrepancy between the homogeneity model and the values from the *top* position of the cells. The c_{IBD} presents an improved 0.59% relative uncertainty, mostly caused by the homogeneity of the correction coefficients along the detector. Combining both efficiency terms, a cell-to-cell systematic uncertainty of 0.84% is obtained taking into account the efficiency-to-efficiency correlations. The cell-to-cell correlated uncertainties presented earlier are used for the final computation of the c_{Gd}, summarized in the next section.

Table 6.3.2: Summary of the cell-to-cell uncorrelated uncertainties for the c_{Gd} and the c_{IBD} using the FIFRELIN package for the MC simulation.

Syst. source	Gd-fraction [%]	IBD cut eff. [%]	eff to eff corr. [%]
time variation	0.10	0.10	0
source pos. bias	0.22	0.27	100
homogeneity uncert.	0.49	0.51	0
total	0.57	0.59	

Table 6.4.1: Obtained c_{Gd} and c_{IBD} correction coefficients and their uncorrelated $\delta_{unc.}(c)$ and correlated $\delta_{c.}(c)$ cell-to-cell total uncertainties using the FIFRELIN package. The c_{tot} values are computed using Eq. 4.4, and their uncertainties are obtained considering the correlations of Table 6.3.2.

Phase I + Phase II – FIFRELIN

Cell	Gd-fraction			IBD cut eff.			Total eff.		
	c	$\pm\delta_{unc.}(c)$	$\pm\delta_{c.}(c)$	c	$\pm\delta_{unc.}(c)$	$\pm\delta_{c.}(c)$	c	$\pm\delta_{unc.}(c)$	$\pm\delta_{c.}(c)$
1	0.9650		0.0041				0.9635		0.0041
2	0.9843		0.0015				0.9828		0.0015
3	0.9846	0.0057	0.0013	0.9985	0.0059	-	0.9831	0.0084	0.0013
4	0.9846		0.0013				0.9831		0.0013
5	0.9844		0.0015				0.9829		0.0015
6	0.9657		0.0040				0.9643		0.0040

6.4 Correction Coefficients for Oscillation Analysis

The total correction coefficient c_ε (Eq. 4.4) is estimated by the combination of the two terms c_{Gd} and c_{IBD}. The values for the oscillation analysis using the FIFRELIN model are compiled in Table 6.4.1. A value for each cell is used for c_{Gd}, while a global value of c_{IBD} is considered in the entire NT. The coefficient c_ε varies between $c_\epsilon^{min} = 0.9635$ and $c_\epsilon^{max} = 0.9831$, and covers the border effects observed in the Gd-fraction and the global agreement of the IBD cut efficiency. The total correction coefficients reach in the border cells a total 0.93% uncertainty, while in the center of the detector a reduced value of 0.85% is obtained. These values have been used in the oscillation analysis presented in Table. 2.3.1-**(iii)**. A detailed comparison of these numbers and the ones obtained with the `GLG4sim` simulation is developed in Section 6.6.

6.5 Correction Coefficients for the Absolute Normalization of the Neutrino Flux

The absolute normalization of the neutrino flux needs a global correction coefficient $\langle c_\varepsilon \rangle$ for the entire NT. The global correction coefficient is constructed as the previous ones,

$$\langle c_\varepsilon \rangle = \langle c_{\text{Gd}} \rangle \cdot \langle c_{\text{IBD}} \rangle \,, \tag{6.12}$$

where $\langle c_{\text{Gd}} \rangle$ and $\langle c_{\text{IBD}} \rangle$ are obtained using the same procedure as in the previous section. On one hand, the IBD cut efficiency term is obtained from the correction coefficient defined in Eq. 6.7,

$$\langle c_{\text{IBD}} \rangle = 0.9985 \pm 0.0059 \text{ (cell-to-cell corr.)} \,. \tag{6.13}$$

The same uncertainty than the one in Table 6.4.1 is considered, since it covers all the statistical and systematic uncertainties. No extra information can be obtained concerning uncertainty correlations, and therefore the conservative approach is the assumption of a full correlation between cells.

On the other hand, a global detector value is computed from the Gd-fraction correction coefficient. For this purpose, the NT value from Table 6.2.3 has been used, since it covers border effects in the c_{Gd} model and the reactor neutrino flux. The used value for the absolute normalization is

$$\langle c_{\mathrm{Gd}} \rangle = 0.9789 \pm 0.0060 \text{ (cell-to-cell corr.)} , \qquad (6.14)$$

where the total uncertainty 0.60% has been obtained from the quadratic sum of: the 0.57% term obtained from a time stability, a source position bias and a homogeneity study from Table 6.3.2; and a 0.20% from the discrepancy between models also summarized in Table 6.3.1. Again, full cell-to-cell correlation has been considered, due to the lack of information about cell correlations. The total absolute normalization term is therefore written as

$$\langle c_\varepsilon \rangle = 0.9774 \pm 0.0084 \text{ (cell-to-cell corr.)} , \qquad (6.15)$$

where any possible uncertainty correlation between the previous mentioned Gd-fraction and IBD cut efficiency terms is taken into account. This value is needed for the comparison of the detected and predicted neutrino fluxes, and it is implemented in analysis of the absolute rate mentioned in Section 2.2.5.

6.6 Impact of the Gamma Cascade Simulation in the Correction Coefficients

All in all, the obtained values with FIFRELIN present a better DATA/MC agreement than with the `GLG4sim` gamma cascade. Most of the absolute discrepancies observed with the old gamma cascade are corrected after the FIFRELIN implementation, which leads to a better understanding of the neutron detection response in the detector.

The neutron correction coefficients c_ε using both a `GLG4sim` and a FIFRELIN MC simulation are summarized in Table 6.6.1. In the same way, the efficiency numbers for the absolute normalization are compiled in Table 6.6.2. The two samples have been treated identically, and therefore any discrepancy on the efficiency ratios is directly caused by the implementation of a different gamma cascade in the MC simulation. A global $\sim 5.4\%$ increase can be seen for both the oscillation analysis and the absolute normalization correction coefficients after the FIFRELIN implementation, reducing the DATA to MC discrepancy from $\sim 7\%$ to $\sim 2\%$. This improvement in the DATA/MC is connected with the better reproduced neutron capture energy spectra presented in Fig. 6.1.3.

Looking in detail into the correction coefficients in Table 6.6.1 for the `GLG4sim` simulation, a relative 2.5% discrepancy has already been observed between the center of the detector and

Table 6.6.1: Comparison between obtained total correction coefficients c_ε with `GLG4sim` and FIFRELIN. Values retrieved from Table 5.5.1 and Table 6.4.1 respectively.

Oscillation analysis correction coefficients

Cell	GLG4sim c	$\pm\delta_{unc.}(c)$	$\pm\delta_{c.}(c)$	FIFRELIN c	$\pm\delta_{unc.}(c)$	$\pm\delta_{c.}(c)$
1	0.9074		0.0042	0.9635		0.0041
2	0.9308		0.0019	0.9828		0.0015
3	0.9310	0.0090	0.0015	0.9831	0.0084	0.0013
4	0.9311		0.0015	0.9831		0.0013
5	0.9306		0.0019	0.9829		0.0015
6	0.9081		0.0041	0.9643		0.0040

Table 6.6.2: Comparison between obtained absolute normalization values with GLG4sim and FIFRELIN.

	Absolute normalization correlation coefficients					
	Gd-fraction		**IBD cut eff.**		**Total abs. norm.**	
MC γ-cascade	$\langle c_{Gd} \rangle$	$\pm \delta_{c.}(\langle c_{Gd} \rangle)$	$\langle c_{IBD} \rangle$	$\pm \delta_{c.}(\langle c_{IBD} \rangle)$	$\langle c_{\varepsilon} \rangle$	$\pm \delta_{c.}(\langle c_{\varepsilon} \rangle)$
GLG4sim	0.9420	0.0051	0.9797	0.0075	0.9229	0.0093
FIFRELIN	0.9789	0.0060	0.9985	0.0059	0.9774	0.0084

the border cells. At the same time, the implementation of the FIFRELIN gamma cascade has caused a minor impact in the border area of the NT volume, and a relative discrepancy of 2% is still present. As it has been represented in Fig. 6.2.4, both models satisfy a modelation along the x-axis with the same function and a compatible parametrization. It points out to another inaccuracy in the MC simulation, related to the neutron interactions and capture cross section.

Table 6.6.1 also portrays a general improvement on the uncertainties after the introduction of FIFRELIN. Such changes can be specially appreciated for c_{IBD}. First of all, mainly due to the energy reconstruction component present in the GLG4sim analysis. This component is not needed for the FIFRELIN studies. Secondly, on the other side a better homogeneity is observed after the FIFRELIN implementation. On the contrary, a slightly worse homogeneity error is obtained with the FIFRELIN simulation on the Gd-fraction efficiency. In Fig. 6.3.1, it has been shown a maximum discrepancy of 1% between the BAND model and the obtained parameters in the *top* region of the cells. This bias is not intrinsically created by the model, but rather by an exogenous source. Since a constant Gd-fraction along the z-axis is considered only for FIFRELIN, a systematic uncertainty covering the *top* discrepancies needs to be taken into account.

6.7 Summary and Conclusions

This chapter has described the impact of the implementation of the FIFRELIN model in the STEREO MC framework. This model, initially developed for the evaluation of fission data, provides useful information to Gd-loaded scintillator experiments about the emitted particles in the process of de-excitation of the Gd nuclei. More concretely, it uses experimental information and theoretical models to describe the level transition between the excited state of the Gd nuclei and the GS. This updated code has brought additional information, like the inclusion of gammas with energy higher than $3.5\,\mathrm{MeV}$ and the reduction by a 4% of the averaged multiplicity with respect to GLG4sim, described in Chapter 5. Both features together with the implementation of electrons as part of the emitted particles in the de-excitation process, have been critical for a proper description of the gamma cascade.

The revised ratio between the emitted gammas and their energy in FIFRELIN has caused a direct impact in the reconstructed energy spectra of the neutron capture. These spectra have been studied with an AmBe neutron source. The discrepancies in the energy region connecting the hydrogen and gadolinium capture energy peaks that were observed when DATA are compared with a GLG4sim simulation, are no longer present after the FIFRELIN implementation. This energy region has a special relevance in the STEREO analysis, since the lower energy cut applied to select neutrons for the IBD correlated signal lies in this area.

The direct impact of the FIFRELIN gamma cascade in the neutrino selection has been investigated with the study of the neutron correction coefficients c_{Gd} and c_{IBD} defined in Section 4.1. These coefficients have been evaluated for all the available DATA during the Phase I and Phase II and they have been compared to MC simulation using FIFRELIN. A better time stability has been observed during Phase II for both correction coefficients at the different heights of the calibration source inside of the cells in Fig. 6.2.1 and Fig. 6.2.6. Consequently, the computed values from Phase II are the ones used to study the impact of FIFRELIN in the detector due to the additional calibration positions available in them. The FIFRELIN cascade has caused a different impact in each of the correction coefficients, thus being studied independently.

The Gd-fraction correction coefficients c_{Gd} presented a $\sim 1.6\%$ improvement with respect to the ones obtained with GLG4sim. The 2% discrepancy between the border and the center of the detector already observed with GLG4sim is still present for Cell 1 and 6, but the discrepancies along the z-axis described in Chapter 5 are no longer observed. A two dimensional model has been implemented on the c_{Gd} values to reproduce the observed border effects when the AmBe source is placed close to the GC walls. This model called BAND uses the same normal distributions along the x- and y-axis than the ones applied on the GLG4sim coefficients by the HAND model. The parametrization with both models is compatible, proving that the border effects are not caused by the γ-cascade implementation. An independent c_{Gd} for each cell has been computed taken into account the constructed BAND function, and the information from a neutrino MC simulation. The obtained results lie between 0.965 and 0.985 for the border cells and the center of the detector respectively, representing the directionality of the neutrino flux. The IBD cut efficiency correction coefficients c_{IBD} have also shown a significant increase of a $\sim 2\%$ in all of the positions due to the cascade implementation. Different cells and positions show general agreement with this model, being considered the mean value 0.9985 as the global coefficient for the entire detector. With the combination of these two terms c_{Gd} and c_{IBD}, a total correction coefficient c_{ε} has been computed for each cell and the results are summarized in Table 6.4.1.

The systematic uncertainties studied cover the time stability, a source position bias, and the spatial inhomogeneities. They can be summarized in two cell-to-cell terms, an uncorrelated one of 0.84% covering the entire volume, and a cell dependent correlatated term up to 0.42%. Both uncertainties present a significant reduction with respect to the computed values for GLG4sim, mostly caused by the upgrade of the energy reconstruction in the current analysis.

The correction coefficients used in the absolute normalization of the detected neutrino flux have been updated with the new gamma cascade. These values are computed from the oscillation analysis correction coefficients, yielding a global value of $\langle c_{\varepsilon} \rangle = 0.9774 \pm 0.0084$. The corrected coefficient has improved with respect to the summarized results in the previous chapter.

Summarizing, the GLG4sim gamma cascade has been creating a tension between MC and DATA in the energy spectra of the neutron capture, causing a bias in the ratio of neutron efficiencies. The implementation of the FIFRELIN model has yielded a notable improvement in this area, consequently reducing the correction coefficients applied to the MC during the STEREO analysis. Despite this upgrade, some border effects are still present in the MC simulation, most likely caused by an inaccurate implementation of the neutron diffusion and/or the capture cross section. This incomplete understanding of the neutron physics has been compensated by applying the BAND model during the computation of the correction coefficients, reaching the desired agreement between DATA and MC while granting a low contribution of systematic uncertainties.

Summary

The relevance of STEREO as one of the very short baseline reactor experiments studying the hypothesis of a sterile neutrino oscillation has been described in this thesis. This experiment, also evaluating the absolute neutrino flux from a highly enriched uranium reactor, observes neutrinos via inverse beta decay (IBD, $\overline{\nu}_e + p \rightarrow e^+ + n$) in its segmented target, filled with liquid scintillator (LS). A good energy containment in the STEREO detector is necessary to properly reconstruct IBD events. Since a data-to-simulation comparison is performed in both STEREO analyses, a set of correction coefficients have been introduced to account for possible disagreements between the selected events in data and simulation samples. More concretely, to consider inaccuracies of the neutron interaction in the detector. This thesis has focused on the study of this neutron interactions, and their impact in the neutrino selection efficiency.

Neutrons created in the IBD process are observed few µs later than the positron annihilation, via radiative emissions from the neutron capture on nuclei present in the LS. Most of the neutron captures occur on the gadolinium isotopes loaded in the LS, followed by a gamma cascade from the excited ^{155}Gd and ^{157}Gd nuclei. This thesis has defined the correction coefficient c_ε, a parameter that studies two different effects: the amount of neutron captures on Gd with respect to the other nuclei, and the impact of the IBD energy and time selection cuts on the neutron events.

The c_ε correction coefficient has been monitored with the calibration data from an AmBe source. This source is characterized by a n emission, that is accompanied by a γ in $\sim 60\%$ of the occasions. It is deployed through the internal calibration tubes of the STEREO detector on a monthly basis, allowing to study the neutron production at different positions. A coincidence selection of the $\gamma + n$ emission has been performed in this thesis, which allows to study the properties of these particles in the detector, such as the reconstructed energy spectra after a neutron capture or the neutron capture time.

During the evaluation of the c_ε, it has been observed that this term is sensitive to inaccuracies in the simulation description of the neutron interactions. Some of them, as the thermal neutron scattering, have been improved to reach a good agreement with data, but some others are still creating a tension in the correction coefficients. More concretely, the amount of neutron captures on Gd nuclei have been studied when the AmBe source was getting closer to the edges of the target volume. Since the center of the detector was consistent between data and simulations, imprecisions in the description of the neutron physics might be the source of this disagreement in the vicinity of the target limit.

A three-dimensional function of the correction coefficient has been developed in this thesis to account for these border effects. This original function uses the information from the source deployment, to contemplate the neutron creation position in the computation. Considering the position of the STEREO detector with respect to the reactor core and the isotropically neutrino emission, an independent correction coefficient c_ε for each detector cell has been computed with this function. This treatment of the correction coefficient is crucial for the STEREO analysis, due to the segmented neutrino target volume.

One of the major improvements in the STEREO simulation has been the implementation of an updated gamma cascade in the de-excitation of a gadolinium isotope. In the first analysis of the STEREO data, the `GLG4sim` package libraries were used to describe it. This package provided an incomplete description of the final states of the gamma cascade, presenting some tension in the simulated energy spectrum describing the released gammas after a neutron capture. These inacuraciones have created a $\sim 6.9\%$ discrepancy with the data samples in the center of the detector, leading to correction coefficients

$$
\begin{aligned}
\text{for central cells} \quad & c_\varepsilon^{\texttt{GLG4sim}} = 0.931 \pm 0.009 \ (\text{stat+syst}) \ , \\
\text{and for border cells} \quad & c_\varepsilon^{\texttt{GLG4sim}} = 0.908 \pm 0.009 \ (\text{stat+syst}) \ .
\end{aligned}
\tag{6.16}
$$

Uncertainties were considered cell-to-cell uncorrelated, and have been evaluated taking into account several factors as the time stability of the different calibration dates, possible source position bias between data and simulations, innacuracies on the energy reconstruction, and the use of a spatial model to describe the border effects of the coefficients. These c_ε values have been used in the oscillation analysis presented in [3], and for the evaluation of the absolute neutrino flux a merged value for the entire detector volume has been obtained:

$$
\langle c_\varepsilon^{\texttt{GLG4sim}} \rangle = 0.923 \pm 0.009 \ (\text{stat+syst}) \ .
\tag{6.17}
$$

This value covers both the disagreement caused by the gamma cascade implementation, and the border effects observed along the detector volume. All of these data to simulation discrepancies triggered the investigation of a better implementation for the gamma cascade. The FIFRELIN model has been tested in the STEREO simulation by replacing the gamma cascade implementation of the `GLG4sim` package. FIFRELIN contains information about the transition levels between the excited state of the ^{155}Gd and ^{157}Gd isotopes and the ground states, using the experimental knowledge from fission data and theoretical models to describe the amount of emitted gammas and their energy. This update caused an exceptional improvement in the energy spectra after a neutron capture, being the disagreement present with the `GLG4sim` packaged no longer observed. A new set of correction coefficients have been computed for the FIFRELIN-based simulations, where an agreement of $\sim 1.7\%$ has been reached between data and simulations. A c_ε for each detector volume has been obtained,

$$
\begin{aligned}
\text{for central cells} \quad & c_\varepsilon^{\text{FIFRELIN}} = 0.983 \pm 0.008 \ (\text{stat+syst}) \ , \\
\text{and for border cells} \quad & c_\varepsilon^{\text{FIFRELIN}} = 0.964 \pm 0.008 \ (\text{stat+syst}) \ .
\end{aligned}
\tag{6.18}
$$

The observed border effects have the same 2% relative impact, for both models, with respect to the center of the detector, being therefore independent to the gamma cascade implementation. The correspondent systematic uncertainties have also been computed in this thesis in the same way as with `GLG4sim`, accounted as cell-to-cell uncorrelated for the oscillation analysis. In

general, these correction coefficients have presented a notable improvement, and have been used for the neutrino oscillation analysis in the lastest publication from STEREO [4]. The averaged correction coefficient for the entire detector volume, used for the calculation of the absolute normalization of the neutrino flux has been increased by $\sim 5\%$ with respect to the one obtained with `GLG4sim` as,

$$\left\langle c_\varepsilon^{\text{FIFRELIN}} \right\rangle = 0.977 \pm 0.008 \ (\text{stat+syst}) \ . \tag{6.19}$$

Summarizing, a set of correction coefficients for the neutron efficiency have been computed in this thesis to perform a proper data-to-simulation comparison. The spatial dependence of the correction coefficients have been modeled to minimize the detection uncertainties. The presented values along this manuscript have been used for the study of the light sterile neutrinos hypothesis, with the best-fit point of the RAA being rejected by the STEREO experiment with 99% C.L. The STEREO study of the absolute neutrino flux from a highly enriched uranium reactor will also benefit from the aforementioned correction coefficients, providing a relevant piece to the reactor neutrinos puzzle with an unprecedented precision.

Calibration dates and MC simulations
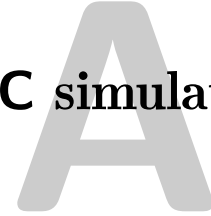
All the information concerning the DATA and the MC files used for the AmBe studies are summarized in this appendix.

A.1 DATA

The calibration DATA samples used for the study of AmBe events are saved in the preprocessing folder `/stereo/ILL_DATA/preprocessed/`. DATA runs are ordered by year and reactor cycle, providing a well-defined path for each calibration date. Runs are separated in different `.root` files, depending on the data taking date and time. The calibration dates are represented in Table A.1.1 for the AmBe deployment. The standard run-time for each calibration run with AmBe is 5 min.

A.2 MC simulations

The MC simulations used for the study of the AmBe events are taken from the official simulation space in `/stereo/MC_reservoir/`. Each phase, calibration system, and MC version are saved different paths `/phaseX/calibsystem/version/AmBe_celli_position.root`. In addition, a specific MC is created for each calibration cell and position, as the calibration DATA. Two different MC versions are used along this thesis, `v2r2` with the `GLG4sim` gamma cascade, and the `v2r4` with the Fifrelin. The MC simulations are created with 2M of AmBe events.

Table A.1.1: Calibration dates with the AmBe source. Different colors represent differen deployment configurations for the source, namely **only deployed at 10/45/80 cm**, in **all the positions (10/30/45/60/80 cm)**, only at the center (45 cm).

	date [YYYYMMDD]	Cell1	Cell2	Cell4	Cell5	Cell6
PHASE I	20161216	X		X		X
	20170106	X		X		X
	20170127	X		X		X
	20170222	X		X		X
PHASE I	20171024	X		X		
	20171027		X		X	
	20171205					X
	20171206	X	X	X	X	
	20180105	X	X	X		X
	20180206	X	X	X	X	X
	20180228	X	X	X	X	X
	20180327	X		X		
	20180418	X	X	X	X	X
	20180426	X	X	X	X	X
	20180619	X	X	X	X	X
	20180712	X	X	X	X	X
	20180813	X	X	X	X	X
	20180919	X	X	X	X	X
	20181031	X	X	X	X	X
	20190109	X	X	X	X	X
	20190212	X	X	X	X	X

B Uncertainties Estimation

B.1 Mean and standard deviation

If $x_1, ..., x_N$ are the results of N measurements of the same magnitude x, then the best estimate for the set is their *mean*

$$\bar{x} = \frac{\sum\limits_{i=1}^{N} x_i}{N} \; .$$ (B.1)

The *standard deviation* of these measurements is computed as follows [76]

$$\sigma_x = \sqrt{\frac{1}{N-1} \sum_{i=1}^{N} (x_i - \bar{x})^2} \; .$$ (B.2)

This parameter[1] represents the average uncertainty in the individual measurements $x_1, ..., x_N$. Consequently, another quantity is defined as the *standard deviation of the mean*,

$$\delta\bar{x} = \frac{1}{\sqrt{N}} \cdot \sigma_x \; .$$ (B.3)

The fact that this parameter would slowly decrease as we increase N, points out that if we make more measurements we would naturally expect the final result more reliable. Another useful parameter is the absolute mean, computed in the same way as Eq. B.1,

$$\bar{x} = \frac{\sum\limits_{i=1}^{N} |x_i|}{N} \; .$$ (B.4)

B.2 Uncertainty in a function of serveral variables

Consider a set ot measured values $x_0, ..., x_n$ with uncertainties $\delta x_0, ..., \delta x_n$, which are used to compute the function $q(x_0, ..., x_n)$. If these uncertainties are independent and uncorrelated, then the uncertainty of q is written [76]

$$\delta q(x_0, ..., x_n) = \sqrt{\sum_{i=0}^{n} \left(\frac{\partial q}{\partial x_i} \delta x_i \right)^2} \; .$$ (B.5)

---

[1]This approximation using the coefficient $N-1$ in the denominator is more conservative that an initial definition (considering only N), and it is better for a number of measurements N small.

This formula has been used to compute some of the uncertainties for the different magnitudes presented along this thesis:

- for the product $f(a,b) = a \cdot b$, its uncertainty is

$$\delta f(a,b) = \sqrt{(b\delta a)^2 + (a\delta b)^2} \ ; \tag{B.6}$$

- for the ratio $f(a,b) = \dfrac{a}{b}$, it is derived as

$$\delta f(a,b) = f \cdot \sqrt{\left(\frac{\delta a}{a}\right)^2 + \left(\frac{\delta b}{b}\right)^2} \ ; \tag{B.7}$$

List of Symbols

HEU	Highly Enriched on Uranium
LEU	Low Enriched on Uranium
LS	Liquid Scintillator
IBD	Inverse Beta Decay
ILL	Institute Laue Langevin
SBL	Short Baseline
VSBL	Very Short Baseline
NT	Neutrino Target
GC	Gamma-Catcher
VETO	Cherenkov muon veto
LAB	Linear Alkylbenzene
PXE	Ortho-phenyl-xylyl-ethane
DIN	Di-isopropy-naphtalene
PPO	Diphenyloxazole
bis-MSB	bis-methylstyrylbenzen
FE8	Front-end electronic boards
TRB	Readout board
PE	Photo-electrons
PSD	Pulse Shape Discrimination
MC	Monte Carlo
GS	Ground State
G4NDL	Geant4 Data Libraries

List of Figures

List of Tables

Acknowledgements

"But in the end, it's only a passing thing, this shadow.
Even darkness must pass. A new day will come,
and when the sun shines it will shine out the clearer.
Those were the stories that stayed with you, that meant something.
Even if you were too small to understand why.
But I think, Mr. Frodo, I do understand. I know now.
Folk in those stories had lots of chances of turning back only they didn't.
because they were holding on to something."
— TOLKIEN, *The Two Towers.*

Many thanks go to the colleagues of the STEREO Collaboration. Working together during the last years has been an enriching experience, even in the moments of full pressure. I would like to particularly thank our spokesperson, Dr. David Lhullier for his helpful suggestions and discussions. Many thanks to Dr. Serge Kox, for his patience filling the ELOG and his greats advices about french restaurants in Grenoble. Special mention goes to Dr. Viktoriya Sergeyeva, Dr Alessandro Minotti, and Dr. Laura Bernard, I have enjoyed working with them these years.

My sincere thanks also goes to the people in the Lindner division. I would like to start with Dr. Teresa Marrodán Undagoitia, because her conversations and advices brought me to the institute. Many thanks to Dr. Guillaume Eurin, for being always there to remove the scientific stress with a cold beer. I would like to thank also my office mates during these years (all of them, considering I have moved 3 times in the last 3 years). Specially to Dr. Alexander Helmboldt, for his tips about writing a thesis, but particularly for our pool-project. Many thanks to Pablo Herrero, for being part of the spanish-lunch team, and for his random conversations about the Simpsons.

This thesis also would not have been possible without the IMPRS-HD, that allowed me to do my doctoral studies here. Specially I would like to mention Dr. Werner Rodejohann, for his help and patience during this time. An honorable mention goes to Anja and Britta, the true heroes of all the PhD theses in our division, for their willingness, enthusiasm, and constant smiling (and obviously, the full supply of cookies!).

I would like to thank my friends I have made during these years, starting with Diana, for our years of friendship in Heidelberg, Tokyo and Madrid, quoting *Lord of the Rings* and adopting Pokemons. Thanks to you I have tried the best ramen of my life! I would also like to thank my panecillo, Marta, for our endless coffees, pizza-wine nights and philosophical bed-time conversations. Even if sometimes I want to kill her so bad, she is definitely one of my best friends. Many thanks also go to the other side of the *sandwich*, Christian, for being my friend during all my years as a physicist, in-side and out-side work. For all the *cervesetes* at the right moment, and the long gossiping conversations.

Por último, quiero agradecer a mi familia, por que esta tesis va por ellos. A a mi hermano Adrián le quiero dar las gracias por ser como es, por compartir mi pasión por Disney y los videojuegos y por ser mi *partner in crime* desde pequeños hasta ahora. A Papá y a Mamá le quiero dar gracias por todo. Por que gracias a ellos soy la persona que soy ahora mismo, por haberse sacrificado toda la vida por nosotros, y por estar ahí siempre. Desde que les dije que me quería ir a estudiar fuera, hasta cuando me he roto la rodilla (por enésima vez). Sé que con ellos tres voy a poder contar siempre, *hasta el infinito, y mas allá.*

Last but definitely not least, I would like to thank my favorite person (in all the worlds), my little *lala-patuki.* From the warmest Helos, to the shiniest Olympus Coliseum, passing through Main Street, you have been always by my side – *aw phooey,* even in the moments I'm just goofing around! Thanks to that, I am not lost anymore, because you are my hikari, you are home. So don't ever forget, no matter where we are, even if you find your socks or not, our hearts will bring us together again – *"This is my family. I found it on my own. It's little and broken, but still good. Yay! Still good."*

Helena Almazán, November 2019.

130

Bibliography

[1] H. Almazan et al, *Sterile Neutrino Constraints from the STEREO Experiment with 66 Days of Reactor-On Data*, Phys. Rev. Lett. 121, 161801 (2018).

[2] J. Lamblin, *Latest Results of the STEREO Experiment*, Talk at XXVIII International Conference on Neutrino Physics and Astrophysics, 4-9 June (2018), Heidelberg, Germany, DOI: 10.5281/zenodo.1286997, https://doi.org/10.5281/zenodo.1286997

[3] L. Bernard, *Reactors anti-neutrino anomaly: search for a sterile neutrino with STEREO experiment* , Talk at Reencontres du Moriond, Electroweak Interactions and Unified Theories, 16-23 March (2019), La Thuile, Italy, https://moriond.in2p3.fr/2019/EW

[4] STEREO Collaboration, *Improved Sterile Neutrino Constraints from the Stereo Experiment with 179 Days of Reactor-On Data*, TBP (2019).

[5] W. Pauli, Reprint of the letter in *The idea of the neutrino*, Physics Today. 31(9): 23–28, (1978).

[6] F. Reines and C.L. Cowan, *Detection of a free neutrino*, Phys. Rev. 92, 830, (1953).

[7] F. Reines and C.L. Cowan, *Detection of a free neutrino: a confirmation*, Science. 124, 3212, 103–104 (1956).

[8] J. N. Bahcall et al, *Solar Neutrinos. I. Theoretical*, Phys. Rev. Lett. 12, 300, (1964).

[9] D. Raymond et al, *Search for Neutrinos from the Sun*, Phys. Rev. Lett. 20, 1205 (1968).

[10] Press release. NobelPrize.org. Nobel Media (2015).

[11] C. Giunti et al, *Fundamentals of neutrino physics and astrophysics*, Oxford University Press (2007).

[12] C. Patrignani et al, *Review of Particle Physics*, Chin. Phys. C40(10):100001 (2019).

[13] V. Antonelli et al, *Solar Neutrinos*, arXiv:1208.1356 (2012).

[14] T. Kajita, *Atmospheric neutrinos and discovery of neutrino oscillations*, Proc Jpn Acad Ser B Phys Biol Sci. 86(4): 303-321 (2010).

[15] P. Vogel et al, *Neutrino Oscillation Studies with Reactors*, Nature Communications 6, 6935 (2015).

[16] S. E Kopp , *Accelerator Neutrino Beams*, Phys.Rept.439:101-159 (2007).

[17] P. Vogel et al, *Reactor antineutrino spectra and their application to antineutrino induced reactions* , Phys. Rev. C 24, 1543 (1981).

[18] K. Schreckenbach et al, *Determination of the antineutrino spectrum from ^{235}U thermal nuetron fission products up to* $9.5\,\mathrm{MeV}$, Phys. Lett. B 160, 325-328, (1985).

[19] A. Hahn et al, *Antineutrino spectra from ^{241}Pu and ^{239}Pu thermal neutron fission products*, Phys. Lett. B 218, 365-368, (1989).

[20] N. Haag et al, *Experimental determination of the antineutrino spectrum of the fission products of ^{238}U*, Phys. Lett. 112, 122501(2014).

[21] T. A. Muller et al, *Improved Predictions of Reactor Antineutrino spectra*, Phys. Rev., vol C83, p. 054615, (2011).

[22] P. Huber et al, *On the determination of anti-neutrino spectra from nuclear reactors*, Phys. Rev., vol C84, p. 024617, (2011).

[23] Double Chooz Collaboration, *Indication for the disappearance of the reactor $\overline{\nu}_e$ in the Double Chooz experiment*, Phys. Rev. Lett. 108, 131901, (2012).

[24] G. Boireau et al, *Online Monitoring of the Osiris Reactor with the Nucifer Neutrino Detector*, Phys. Rev. D 93, 112006 (2016).

[25] G. Mention et al, *The Reactor Antineutrino Anomaly*, Phys. Rev. D83:073006 (2011).

[26] S. Gariazzo et al, *Updated Global 3+1 Analysis of Short-BaseLine Neutrino Oscillations*, 10.1007/JHEP06 135 (2017).

[27] F. P. An et al, *Evolution of the Reactor Antineutrino Flux and Spectrum at Daya Bay*, Phys. Rev. Lett. , vol 118, p. 251801 (2017).

[28] C. Giunti et al, *Reactor Fuel Fraction Information on the Antineutrino Anomaly*, JHEP, vol 1710, p. 143, (2017).

[29] C. Giunti et al, *Diagnosing the Reactor Antineutrino Anomaly with Global Antineutrino Flux Data*, Phys. Rev. vol D99, no. 7, p 073005 (2019).

[30] Y, Abe et al, *Improved measurements of the neutrino mixing angle θ_{13} with the Double Chooz detector*, JHEP, vol. 10, p.086 (2014).

[31] F. P. An et al, *Measurement of the Reactor Antineutrino Flux and Spectrum at Daya Bay*, Phys. Rev. Lett. vol 116, p 061801 (2016).

[32] J. Choi et al, *Observation of Energy and Baseline Dependent reactor Antineutrino disappearance in the RENO Experiment*, Phys. Rev. vol 116, p 211801 (2016).

[33] G. Mention et al, *Reactor antineutrino shoulder explained by energy scale nonlinearities*, Phys. Rev. vol B773, pp. 307-312, (2017).

[34] C. Buck et al, *Investigate the Spectral Anomaly with Different Reactor Antineutrino Experiments*, Phys. Rev. vol B765, pp. 159-162, (2017).

[35] F. Kaether et al, *Reanalysis of the GALLEX solar neutrino flux and source experiments*, Phys. Lett., vol. B685, pp. 47–54, (2010).

[36] A. Aguilar-Arevalo et al, *Evidence for neutrino oscillations from the observation of anti-neutrino (electron) appearance in a anti-neutrino (muon) beam*, Phys. Rev., vol D64, p. 112007 (2001)

[37] A. Aguilar-Arevalo et al, *Improved search for $\overline{\nu}_\mu \to \overline{\nu}_e$ oscillations in the MiniBooNE experiment*, Phys. Rev. Lett., vol 110, p. 161801, (2013).

[38] S. Boeser et al, *Status of Light Sterile Neutrino Searches*, Prog. in Part. and Nucl. Phys 103736 https://doi.org/10.1016/j.ppnp.2019.103736 (2019).

[39] J. Ashenfelter et al, *The PROSPECT Reactor Antineutrino Experiment*, Nucle. Instrum. Meth., vol A922, pp. 287–309 (2019)

[40] Y. Ko et al, *A sterile neutrino search at NEOS Experiment*, Phys. Rev. Lett., vol 118, p. 121802 (2017).

[41] I. Alekseev et al, *Search for sterile neutrinos at the DANSS experiment*, Phys. Lett., vol B787, pp. 56–63 (2018).

[42] Y. Abreu et al, *A novel segmented-scintillator antineutrino detector*, JINST, vol. 12, no 04, p. P04024 (2017).

[43] A. Serebrov et al, *The first observation of effect of oscillation in Neutrino-4 experiment on search for sterile neutrino*, JETP Letters, (2019).

[44] D. Lhuillier et al, *Proposal of a search for sterile neutrinos at ILL: the STEREO experiment.* Proposal STEREO experiment (2012).

[45] N. Allemandou et al, *The STEREO experiment.* Journal of Instrumentation. 13 (7): P07009. arXiv:1804.09052 (2018).

[46] C. Aberle et al, *Large scale Gd-beta-diketonate based organic liquid scintillator production for antineutrino detection*, JINST 7 P06008 (2012).

[47] P. Mutti et al, *Nomad more than a simple sequencer*, Proc. ICALEPCS (2011)

[48] A. Bonhomme, *Anomalie des antineutrinos de réacteurs: recherche d'un état stérile avec l'expérience STEREO*, Physique des Hautes Energies - Expérience [hep-ex]. Université Paris-Saclay (2018). Franąis. NNT : 2018SACLS319 . tel-01931309.

[49] N. Voudoukis, *Inverse square law for light and radiation: A unifying educational approach*, European Journal of Engineering Research and Science, 10.24018/ejers.2017.2.11.517, (2017)

[50] I. El Atmani, *Update Absolute Normalization Emitted Neutrino Flux*, STEREO Internal Document, stereo-doc-1048-v1 (2019).

[51] H. Almazan et al, *Improved STEREO simulation with a new gamma ray spectrum of excited gadolinium isotopes using FIFRELIN*, Eur. Phys. J. A (2019) 55: 183. https://doi.org/10.1140/epja/i2019-12886-y.

[52] G. Knoll, *Radiation Detection and Measurement.* 3rd ed. John Wiley and Sons, New York (2000).

[53] National Nuclear Data Center, *EDDF/B-VIII.0 Nuclear Data for Science and Technology: Cross Sections, Covariances, Fission Product Yields and Decay Data.* Nuclear Data Sheets **148**, 1040 (2018).

[54] International Atomic Energy Agency, *Thermal neutron capture γs information*, `https://www-nds.iaea.org/capgam/indexbyn.htmlx`

[55] K. Hagiwara et al, *Gamma-ray Spectrum from Thermal Neutron Capture on Gadolinium-157.* PTEP, Volumen 2019, Issue 2, February 2019, 023D01, `https://doi.org/10.1093/ptep/ptz002`

[56] Hamamatsu Company, *Photomultiplier Tube R5912*, `https://www.hamamatsu.com/eu/en/product/type/R5912/index.html`

[57] P. Huber, *On the determination of anti-neutrino spectra from nuclear reactors*, Phys. Rev. C 84, 024617 (2011), `https://arxiv.org/abs/1106.0687`.

[58] J.-Ch. Sublet et al, *FISPACT-II: An Advanced Simulation System for Activation, Transmutation and Material Modelling*, Nuclear Data Sheets 139, 77 (2017).

[59] J. B. Birks, *Scintillations from Organic Crystals: Specific Fluorescence and Relative Response to Different Radiations*, Proc. Phys. Soc. A64 (10): 874-877 (1951).

[60] J. Allison et al, *Recent developments in Geant4*, Nucl. Instrum. Meth. A 835, 186 (2016).

[61] C. Buck et al, *Production and Properties of the Liquid Scintillators used in the Stereo Reactor Neutrino Experiment*, Journal of Instrumentation 14, P01027 (2019) `https://arxiv.org/abs/1812.02998`.

[62] S.Y.F. Chu et al, *The Lund/LBNL Nuclear Data Search*, `nucleardata.nuclear.lu.se/toi/`

[63] A. A. Mowlavi et al, *Determination of 4.438 MeV γ-ray to neutron emission ratio from a AmBe neutron source*, Applied Radiation and Isotopes Volume 60, Issue 6, June 2004, Pages 959-962.

[64] J. Scherzinger et al, *Tagging fast neutrons from an $^{241}Am^9Be$ source*, Applied Radiation and Isotopes Volume 98, January 2015, Pages 74-79.

[65] C. Roca, *Optimization of the simulation framework in the STEREO Experiment to characterize the detector response and optical properties of the liquid scintillators*, Dissertation Heidelberg University, `https://doi.org/10.11588/heidok.00026500` ,(2019).

[66] H. Almazan, *Update on the status of the neutron MC simulations and its effects on the neutron efficiency*, STEREO Internal Document, stereo-doc-786-v1 (2018).

[67] H. Almazan, *Test of a MC with a reduced Gd concentration*, STEREO Internal Document, stereo-doc-486-v1 (2018)

[68] J. Haser, *Neutrino detection uncertainties in the θ_{13} analysis of the Double Chooz experiment*, Dissertation University of Heidelberg, `https://doi.org/10.11588/heidok.00018432`, (2015).

[69] H. Almazan, *Consistencies of the neutron detection effciency in the Double Chooz reactor neutrino detectors*, Master Thesis, Ruprecht-Karls-Universitãđt, Heidelberg, `http://hdl.handle.net/11858/00-001M-0000-002B-A0F7-D`, (2016)

[70] H. Almazan, *Neutron efficiency studies: cell center*, Stereo Internal Document, stereo-doc-371-v1 (2017).

[71] M. T. Subbotin, *On the Law of Frequency of Error*, Mat. Sb., Volume 31, Number 2, Pages 296-301 (1923).

[72] A. Blanchet, *Recherche du neutrino stérile auprés du réacteur de l'ILL: expérience Stereo.*, `https://www.theses.fr/s163080`, (2019).

[73] L. Bernard, *Recherche d'un neutrino stérile avec l'expérience STEREO : Détermination des spectres neutrinos et caractérisation du bruit de fond*, `https://www.theses.fr/s164415`, (2019).

[74] L. Bernard, *Neutrino simulation: acceptance of selection cuts*, Stereo Internal Document, stereo-doc-706-v6 (2019).

[75] *Additional gadolinium support for GLG4sim*, `http://neutrino.phys.ksu.edu/~GLG4sim/Gd.html.`

[76] J.R. Taylor, *Introduction to error analysis*, University Science Books Sausalito, California (1997).

[77] M. Paterno, *Calculating Efficiencies and Their Uncertainties*, `https://home.fnal.gov/~paterno/images/effic.pdf` (2003).

[78] T. Salagnac, *Absolute normalization of the neutrino flux*, Stereo Internal Document, stereo-doc-711-v1 (2018).

[79] O. Litaize et al, *Fission modelling with FIFRELIN*, Eur. Phys. Ja. A, vol 51, no. 177, pp 1–14 (2015).

[80] E. Porter and C. R. G. Thomas, *Fluctuations of nuclear reaction widths*, Phys. Rev., vol 104, p. 483 (1956).

[81] T.Kibedi et al, *Evaluation of theoretical conversion coefficients using bricc*, Nucl. Instr. Meth. Phys. Res. A, vol. 589, pp. 202–228 (2008).